Towards an understanding of the upconversion efficiencies of Pr^{3+} involving the $4f^1 5d^1$ configuration

Author
FLORIS KOOIJ

Supervisors
Dr. MARKUS SUTA
Prof. Dr. ANDRIES MEIJERINK
Dr. SANLI FAEZ

July 21, 2019

CONDENSED MATTER AND INTERFACES
DEBYE INSITUTE FOR NANOMATERIALS SCIENCE

Utrecht University

Abstract

The energy level structure of Pr^{3+} theoretically allows for an efficient blue-to-UV single-ion upconversion process by means of sequential ground state absorption (GSA) and excited state absorption (ESA), finding possible applications in the development of high-power UV lasers. However, studies on the single-ion upconversion of Pr^{3+} involving the excited $4f^1 5d^1$ configuration are only scarce, with so far limited applications. A recent breakthrough was achieved with β-$Y_2 Si_2 O_7$:Pr^{3+} that showed a promising upconversion efficiency of around $0.75 \cdot 10^{-2}\%$ given the fact that bioorganisms are very sensitive to UVC radiation. In this thesis, the main goal is a fundamental understanding of the impacts of the involved electronic levels on the upconversion efficiency of Pr^{3+}. For that purpose, Pr^{3+}-activated $LaBO_3$, YPO_4 and $Lu_3 Al_5 O_{12}$ (LuAG) were chosen as phosphors. Measurements on the intraconfigurational $4f^2 \leftrightarrow 4f^{2'}$ luminescence in the Pr^{3+}-activated compounds revealed an efficient $^3H_4 \rightarrow ^3P_2$ GSA in agreement with predictions based on a Judd-Ofelt analysis. Moreover, all three compounds have a sufficiently high phonon energy to favor a non-radiative relaxation to the metastable $^1D_2$ level of Pr^{3+}, which has already been shown to be of critical importance for a more efficient ESA to the $4f^1 5d^1$ configuration. Decay measurements performed for the $4f^2$-based levels relevant for upconversion also indicated a more metastable $^1D_2$ level compared to the $^3P_0$ level. Upon 451 nm excitation low-intensity $4f^1 5d^1 \rightarrow 4f^2$ upconverted emission was observed for all three Pr^{3+}-activated compounds even with a pulsed optical parametric oscillator (OPO) instead of a continuous wave laser. The dependence of the upconversion emission intensity on the relative excitation power revealed a linear dependence in the high-power regime for all three compounds indicating a saturation behavior. For LuAG:Pr^{3+}, a quadratic dependence in the lower-power regime was additionally observed in agreement with expectations based on the nature as a two-photon process. Based on our observations, we develop a better understanding of the energy of the $4f^1 5d^1$ configuration of Pr^{3+} and the maximum phonon energy of the host lattice, and are able to prescribe elements for a host lattice suitable for achieving a more efficient upconversion emission. In addition to Pr^{3+}, also Tm^{2+} was proven to be an efficient NIR-to-visible upconversion activator involving an electric dipole-allowed $4f^{13} \rightarrow 4f^{12} 5d^1$ ESA. In order to investigate this alternative, it was attempted to investigate $SrB_4 O_7$:Tm^{2+}, which was reported to readily incorporate Tm^{2+} even on air. This feature is far from trivial since it is otherwise chemically challenging to reduce Tm^{3+} even under inert conditions. Throughout this thesis, it was possible to successfully synthesize the $SrB_4 O_7$ host, whereas luminescence studies revealed the major presence of Tm^{3+}, however, and thus, avoided a detailed study on the upconversion efficiency in this compound. Finally, also Sm^{2+} was investigated as an academic intermediate example for a red-to-red upconversion system including a $4f^6(^7F_0) \rightarrow 4f^6(^5D_J)$ GSA and a $4f^6 \rightarrow 4f^5 5d^1$ ESA. For that purpose, a low-energy phonon host such as SrFCl would be useful. While the synthesis of the host did work, it was not possible to reduce initially incorporated Sm^{3+} in there. In contrast, $SrB_4 O_7$:Sm^{2+} could be synthesized and exhibited intense deep red $4f^6(^5D_0) \rightarrow 4f^6(^7F_J)$ luminescence. In agreement to expectations according to the much higher phonon energy of this host material, no upconversion could be observed in this compound even at 4.2 K. In summary, this thesis may provide some general insights in the boundary conditions for efficient upconversion processes involving the less investigated $4f^{n-1} 5d^1$ configuration of lanthanide ions.

Contents

1 Introduction

Upconversion (UC) is a special multi-phonon process within the field of luminescence, in which the absorption of multiple low-energy photons results in the emission of a single high-energy photon. Given their rich $4f^n$ energy level landscape, lanthanide ions have long been subject to extensive research regarding upconversion luminescence. Most studies regarding upconversion within lanthanide ions utilize an energy transfer between the $4f^n$-based energy levels in different lanthanide ions. An illustrative example of this is the Yb^{3+}/Er^{3+} couple, capable of achieving efficient near-infrared (NIR) to visible upconversion when doped in β-$NaYF_4$.[1,2] In addition to this energy transfer upconversion (ETU), there is the possibility of single-ion upconversion within lanthandide ions, in which the UC takes place by consecutive excitations of the same ion.

One lanthanide ion in particular, Pr^{3+} ($n = 2$), displays enormous potential as a $4f^2 \leftrightarrow 4f^1 5d^1$ single-ion upconverting agent, as its energy levels theoretically allow for a blue-to-UV upconversion process, finding possible applications in the development of high-power UV lasers. However, the few studies that have been published on the $4f^1 5d^1 \to 4f^2$ UC emission report a similarly low quantum yield for this process, a phenomenon for which no conclusive origin is hitherto known.[3–5] A recent breakthrough in this area was achieved by Cates *et al.*, who reported the most efficient $4f^1 5d^1$-related UV upconverted emission in Pr^{3+}-activated β-Y_2SiO_5 (YSO)[6–8] and $Y_2Si_2O_7$ (YPS)[9] observed so far. They also proposed that the unusual UC efficiency must be related to an efficient non-radiative relaxation pathway to the metastable $^1D_2$ $4f^2$-based level of Pr^{3+} from which excited state absorption (ESA) to the $4f^1 5d^1$ configuration can occur. Interestingly, in contrast to the generally poorly efficient upconversion, Pr^{3+} has been shown to be an excellent downconverting, or quantum cutting, agent, both by itself[10,11] and coupled with Yb^{3+}.[12,13]

Contrary to Pr^{3+}, the involvement of the corresponding $4f^n \leftrightarrow 4f^{n-1} 5d^1$ of Tm^{2+} ($n = 13$) in a potential UC process has been studied to a somewhat higher degree, and is generally better understood. The first case of conventional $4f^{12} 5d^1 \to 4f^{12}$ luminescence in Tm^{2+} was reported back in 1994,[14] with appreciably efficient upconversion performances in Tm^{2+}-doped materials being reported more recently.[15–18] In addition to Tm^{2+}, Sm^{2+} ($n = 6$) may also serve as an upconverting agent from a fundamental point of view. Most typically, the very similar energy of the $4f^5 5d^1$ configuration compared to the excited $4f^6(^5D_J)$ levels of Sm^{2+} make this ion an ideal candidate for temperature and pressure sensing.[19–24] Due to this unique electronic situation, Sm^{2+} may be suited as a test example for a red-to-red upconversion involving the excited $4f^5 5d^1$ configuration in the ESA. As such it represents an intermediate case between the NIR-to-visible UC of Tm^{2+} and blue-to-UV UC of Pr^{3+}.

The goal of this thesis is a deeper insight into the conditions for an efficient upconversion of Pr^{3+} involving the $4f^1 5d^1$ configuration. To that avail, three host lattices for Pr^{3+} were selected: $LaBO_3$, YPO_4 and LuAG ($LuAl_5O_{12}$). The upconversion mechanism as well as the impact of the host material on the upconversion efficiency were carefully investigated in order to allow for predictive guidelines. Additionally, decay kinetics of the relevant electronic energy levels were investigated related to the underlying mechanism.

In addition to the selected Pr^{3+}-activated compounds, the upconversion emission in Tm^{2+} and Sm^{2+} was attempted to be investigated. For Tm^{2+}, the SrB_4O_7 lattice was selected as a host, as it is one of the only compounds known to stabilize Tm^{2+} on air. Sm^{2+} was also chosen to be incorporated into the SrB_4O_7 host, in addition to the SrFCl host. The latter was selected based on the correspondingly higher energy of the $4f^5 5d^1$ configuration in Sm^{2+} and the lower phonon energy compared to the SrB_4O_7 host. Based on the results presented within this thesis, it is sought for a deeper understanding of the mechanism of interconfigurational upconversion processes within lanthanide ions in general.

2 Theoretical background

In this section, the theoretical backgrounds required for a better understanding of the results as well as their interpretation are presented. It deals with a short, basic review of the terms lanthanides, photon upconversion and term symbols, as well as several possible types of energy transfer. It will then proceed with an overview of upconversion mechanisms, the characteristics of the transitions involved and the relevant energy level diagrams.

2.1 Lanthanides, photon upconversion and term symbols

Lanthanides (meaning 'like Lanthanum') is a collective term for the elements with atomic numbers ranging from 57 (Lanthanum) to 71 (Cerium). Occupying the first row of the f-block in the periodic table, they possess the electron configuration $[Xe]6s^2 4f^n$. In addition, La, Ce, Gd an Lu each have 1 electron occupying a 5d-orbital. It is this partially filled 4f shell that is the basis of the characteristic optical properties most lanthanide ions display.

Photon upconversion (UC) is, in the broadest of senses, a photophysical phenomenon where a single high-energy photon is emitted after the sequential absorption of multiple lower energetic photons. In most UC processes, two photons are converted into a higher energetic photon, but UC processes with a conversion of more than two photons do exist. They become, however, less probable. Since the energy of emitted photons is higher than that of absorbed photons, upconversion processes are also denoted as anti-Stokes processes. UC was first proven experimentally by Auzel et al.[17] in 1966, and has developed enormously since then.

Term symbols are abbreviated quantum mechanical descriptions for the angular momentum quantum numbers labelling a many-electron wave function of an atom or ion. Term symbols assume Russel-Saunders coupling (which is also referred to LS coupling), which, in short, entails that spin-orbit coupling is weak enough that the total orbital angular momentum $L = \sum_i l_i$ and total spin angular momentum $S = \sum_i s_i$ can still be considered good quantum numbers, but already couple to to form a total angular momentum $J = L + S$.[25] Since L and S are well-defined quantum numbers, the atomic states are readily described by term symbols, which are denoted as $^{2S+1}L_J$, where $2S + 1$ denotes the spin multiplicity. Within these term symbols, L is denoted in the spectroscopic notation: L-values of 0, 1, 2, 3, 4. . . are indicated as S, P, D, F, G. . . . From F onward, the symbols proceed alphabetically, with the exception of J, which is reserved to represent the total angular momentum of a quantum state. Hence, for example, a state with $L = 6$, $J = 8$ and $S = 2$ would be denoted as $^5I_8$.

2.2 Energy transfer

Energy transfer is a process in which the excitation energy is transferred from one entity to another either radiatively or non-radiatively and thus, allows for an indirect excitation. In energy transfer, the ion that is directly being excited by the light source and that transfers the energy, is known as the sensitizer or donor. The ion that receives the energy is known as the activator. The sensitizer and the activator may be either identical or different ions.[17] One type of energy transfer is resonant radiative transfer: here, the sensitizer emits a real photon upon relaxation from its excited state to the ground state, which is then absorbed by a distant activator ion within the photon travel distance. A schematic representation of this transfer process may be found in Figure 1a. The probability of such a transfer between two ions with inter-ionic distance R is found to be[17, 26]

$$p_{SA}(R) = \frac{\sigma_A}{4\pi R^2 \tau_s} \int g_s(\nu) g_a(\nu) d\nu \tag{1}$$

where σ_A is the absorption cross-section, τ_s is the average sensitizer decay time in absence of an acceptor, since the photon will be emitted regardless of the presence of an activator ion within the photon travel length, the integral represents the spectral overlap between the emission spectrum of the sensitizer and excitation spectrum of the activator, both denoted by a line function $g(\nu)$. As can be directly concluded from equation 1, energy transfer is more effective at lower inter-ionic distances, resulting in a more efficient process for higher doping concentrations of both sensitizer and activator.

In analogy to resonant radiative transfer, resonant non-radiative decay requires the sensitizer and activator to have a nearly equal energy separation between their electronic ground state and respective excited state. Unlike the case of radiative however, the excitation 'jumps' from sensitizer to activator directly via the Coulomb interaction in the case of non-radiative transfer, a schematic representation thereof is given in Figure 1b. In the case of a Coulomb interaction, the transfer probability follows the simple formula[17, 27]

$$p_{SA}(R) = \frac{(R_0/R)^n}{\tau_s} \tag{2}$$

where n is a number dependent upon the type of interaction: it equals 6 for dipole-dipole interactions, 8 for dipole-quadrupole interactions and 10 for quadrupole-quadrupole interactions, and R_0 the critical transfer distance at
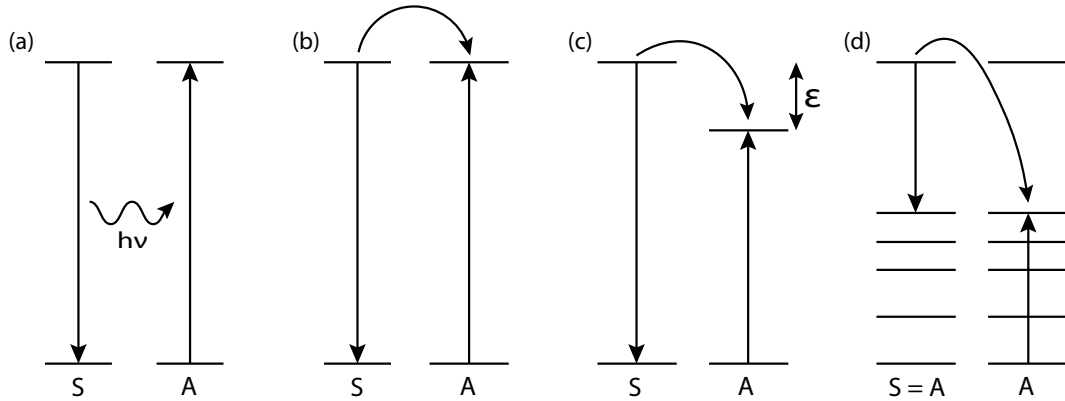
Figure 1: Types of energy transfer between sensitizer (S) and activator (A) ions: (a) resonant radiative transfer, (b) resonant non-radiative transfer, (c) phonon-assisted non-radiative transfer, where ε denotes the energy gap between the two excited states, and (d) cross-relaxation, where sensitizer and activator are identical ions

which excitation transfer and spontaneous sensitizer emission have equal probabilities.[17] Theoretically accurate predictions of R_0 are generally difficult, but became possible by the approaches of Kushida[28] or Pouradier and Auzel[29] in terms of Racah tensor algebra in analogy to Judd-Ofelt theory. From equation 2, it may be easily concluded that resonant non-radiative energy transfer becomes dominant at small inter-ionic distances, and, as such, high doping concentrations.

One requirement for both radiative and non-radiative resonant energy transfer is a match in the energy gap between the ground state and excited state of both the sensitizer and the activator ion. If an energy mismatch is present however, non-radiative transfer may still occur by a phonon-assisted process, due to a phonon-broadened overlap. Grossly oversimplified, a phonon is a collective excitation of host lattice electrons to higher vibrational modes. These phonons, or lattice vibrations, play a major role in many physical properties in condensed matter, and hence, are among the most paramount of subjects regarding condensed matter studies. Thus, energy transfer can still occur by incorporation of phonons into the mechanism, as depicted in Figure 1c.

A special case of non-radiative transfer is cross relaxation: it refers to all types of partial energy transfer cases were sensitizer and activator are identical ions. A schematic representation of this process is displayed in Figure 1d. If the energy of the involved levels is identical, diffusion might take place, where the energy of the photon ultimately emitted is unchanged with respect to the situation in which no cross-relaxation occurs. More relevant, however, is the case were these energies are different: in that case, self-quenching may take place, which is naturally detrimental to all other types of luminescence.

2.2.1 Multi-phonon relaxation

In addition to radiative decay from an excited state, where the loss of energy by the electron upon relaxating from a higher- energy state to a lower-energy state is manifested as the emission of a photon, there is also the possibility of non-radiative multi-phonon relaxation. In this process, the energy loss by the electron is not transferred to a photon, but is instead transferred to the host lattice to excite electrons in phonons. The more phonons the energy difference between two states corresponds to, the smaller the probability of the non-radiative transfer process from the higher to the lower of the two states. As a rule of thumb, if the energy difference between two states corresponds to ~5 times the phonon energy or more, the probability of the multi-phonon relaxation from the higher to the lower state can be considered negligible in comparison with the probability of radiative transfer. In return, if the energy difference between two states corresponds to a much lower number of phonons, the probability of radiative decay will be negligible when compared to the probability of multi-phonon relaxation.

2.3 Electronic transitions in lanthanide ions

2.3.1 Parity selection rule and Judd-Ofelt theory

Whether the wave function describing an electron in a free atom/ion has an odd or an even parity, is dictated by its azimuthal quantum number l: if l is even (as is the case for s and d orbitals), the electron will possess an even parity, whereas an odd l (as is the case for p and f orbitals) dictates odd parity. According to Fermi's golden rule, the intensity of an electric dipole (ED) transition between an initial state ψ_i and final state ψ_f is proportional to the absolute square of its matrix element[18, 30]

$$I_{abs/em} \propto |\langle \psi_i | \vec{\mu}_{ED} | \psi_f \rangle |^2 \tag{3}$$

where $\vec{\mu}_{ED}$ is the ED operator, which can be expressed as[30]

$$\vec{\mu}_{ED} = -e \sum_i \vec{r}_i \tag{4}$$

As the ED operator possesses odd parity, this matrix element is equal to zero if the initial state and the final state posses the same parity, as is the case for the intraconfigurational $4f^n \leftrightarrow 4f^{n'}$ transitions within lanthanide ions. These transitions however, are both magnetic dipole (MD) and electric quadruple (EQ) allowed, since both of the operators associated with them posses even parity.[30] Consequently, MD and EQ transitions can be shown to be a factor $\sim (2\alpha)^{-2} \sim 10^{-5}$ lower than the ED allowed transitions, where α denotes the electromagnetic fine structure constant.[30, 31]

Experimentally however, $4f^n \leftrightarrow 4f^{n'}$ transitions are well known occur within lanthanide ions with an intensity far greater than can be explained by merely viewing them as MD or EQ transitions, which thus contradicts the predictions made by conventional quantum mechanics.[32, 33] This contradiction resulted in the development of a theory on forced electric dipole $4f^n \leftrightarrow 4f^{n'}$ transitions that was published independently by Brian R. Judd[34] and George S. Ofelt.[31] The detailed mathematical derivation of Judd-Ofelt theory is far beyond the scope of this section, so only a concise overview of the most important aspects of it's derivation, assumptions and results will be discussed.

The essence of Judd-Ofelt theory is that it considers admixtures of even parity orbitals (d or g orbitals) to the otherwise purely odd parity $4f^n$ levels by odd contributions of a crystal field in a non-centrosymmetric environment. Since this contribution differs between different $4f^n$-based electronic levels, this allows for a partially ED allowed character of the $4f^n \leftrightarrow 4f^{n'}$ transitions. Mathematically, the odd components of the crystal field is viewed as a first order perturbation of the all-even parity 4f states, which is a good approximation since the crystal field only acts weakly on the well-shielded 4f orbitals. These mixed parity states are thus formulated as follows:[18, 31, 34]

$$|\psi'\rangle = |\psi\rangle + \sum_{nl} \frac{\langle \psi | \mathcal{V}_{odd} | \psi \rangle}{E(\psi) - E(nl)} |nl\rangle \tag{5}$$

where, $|nl\rangle$ denotes the even parity states, ψ the odd-parity unperturbed $4f^n$ states, and $\mathcal{V}_{odd}$ the odd-parity crystal field. For the same reasons regarding the odd parity of the operator and both unperturbed wave functions ψ_i and ψ_f possessing the same parity for an intraconfigurational transition, the matrix elements $\langle \psi_i | \mathcal{V}_{odd} | \psi_f \rangle$ and $\langle nl | \mathcal{V}_{odd} | nl \rangle$ must be equal to zero. Hence, the expression for the electric dipole matrix elements becomes[18, 31, 34]

$$\langle \psi_i | \vec{\mu}_{ED} | \psi_f \rangle = \sum_{nl} \left(\frac{\langle \psi_i | \mu_{ED} | nl \rangle \langle nl | \mathcal{V}_{odd} | \psi_f \rangle}{E(\psi_f) - E(nl)} + \frac{\langle \psi_f | \mu_{ED} | nl \rangle \langle nl | \mathcal{V}_{odd} | \psi_i \rangle}{E(\psi_i) - E(nl)} \right) \tag{6}$$

Next, Judd-Ofelt theory makes two assumptions in order to simplify this equation. The first one is that the even parity states $|nl\rangle$ are assumed to be degenerate in J, and that they can be characterized by a barycenter energy $E(nl)$. The second assumption is that the energy differences between the $4f^n$ states are much smaller than the energy difference between any of the $4f^n$ and the $4f^{n-1}5d^1$ states, so that $E(\psi_f) - E(nl)$ and $E(\psi_i) - E(nl)$ can be considered equal. After employment of symmetry principles and tensor algebra involving the Wigner-Eickart theorem, an expression for the line strength of the intraconfigurational transitions, denoted by S_{ED}, is found:[18, 30, 31, 34]

$$S_{ED} = e^2 \sum_{\lambda=2,4,6} \Omega_\lambda \left| \left\langle l^N SLJ\gamma \left\| U^{(\lambda)} \right\| l^{N'} S'L'J'\gamma' \right\rangle \right|^2 \tag{7}$$

Here, $U^{(\lambda)}$ represent the irreducible unit tensor forms of rank λ of the ED operator, with the whole term between brackets denoting the reduced matrix element with the intermediate coupling scheme.[18] These reduced matrix elements (or, more precisely, their absolute squares) are characteristic for a specific $4f^n \leftrightarrow 4f^{n'}$ transition of the

free ion and only negligibly affected by the surrounding host. Values for these reduced matrix elements have been tabulated extensively for a wide variety of transitions within different lanthanide ions. More recently, software such as RELIC automatically implemented these matrix elements for additional processing.[35] The Judd-Ofelt parameters Ω_λ in the order of 10^{-20} cm^2 on the other hand, are dependent on the host material a considered lanthanide ion is incorporated in and typically considered as phenomenological parameters that are determined by least-squares fits on the intensities of the experimental absorption spectra,[35] and have been extensively tabulated for a wide variety of host lattices.

The term intermediate coupling assumed in the calculation of the reduced matrix elements refers to the fact that lanthanide ions are an intermediate case between Russell-Saunders coupling on one hand, and jj coupling, where the spin-orbit coupling is so strong that each individual orbital angular momentum l_i and corresponding spin s_i couple to the total angular momentum of that electron j_i, which in turn couple to the total angular momentum $J = \sum_i j_i = \sum_i (l_i + s_i)$.[36,37] In the case of jj coupling, L and S as separate quantum numbers do not appropriately describe eigenstates of the Hamiltonian anymore and thus lose their meaning in the extreme case of strong spin-orbit coupling. In the end, Judd-Ofelt theory provides both a powerful tool to predict the line strengths of intraconfigurational $4f^n \leftrightarrow 4f^{n'}$ transitions, and also a reasonable explanation for the observed higher intensities than for MD or EQ transitions as would be predicted by conventional quantum mechanics.

2.3.2 $4f^n \leftrightarrow 4f^{n'}$ transitions in lanthanide ions

As laid down in detail within the previous sub-section, the intraconfigurational $4f^n \leftrightarrow 4f^{n'}$ in lanthanide ions are parity-forbidden, yielding low line-strengths of this kind of transitions. Due to the relatively large energy separation of the discrete $4f^n$-based electronic energy levels, intraconfigurational $4f^n \leftrightarrow 4f^{n'}$ transitions within lanthanide ions are characterized by narrow absorption and emission lines. Another characteristic of this type of transition is that its energies are are relatively insensitive to the host lattices in which the lanthanide ion is incorporated. This feature is easily explained by the fact that the 4f orbitals within the lanthanide ions are well-shielded by electron in the 5s and 5p orbitals, which have a larger radial extent than the 4f orbitals.[38] Finally, this shielding of the 4f orbitals results in the equilibrium bond lengths for the $4f^n$ ground state and $4f^{n'}$ excited states to be virtually unchanged in turn yields narrow absorption and emission lines for this type of transition, as depicted in Figure 2.

2.3.3 $4f^n \leftrightarrow 4f^{n-1}5d^1$ transitions in lanthanide ions

In contrast to the well-defined energy levels of $4f^n$-based electron configurations, the $4f^{n-1}5d^1$ configuration in lanthanide ions consists of many closely lying energy levels, such that they may be represented as a quasi-continuous energy band, resulting in characteristic broad emission and absorption bands for transitions involving the $4f^{n-1}5d^1$ configuration. Due to the larger radial extent of the 5d wavefunctions, the $4f^{n-1}5d^1$ configuration is poorly shielded, making the electrons occupying it susceptible to host lattices influences. Consequently, influence of the host lattice via nephelauxetic effect (covalence of the lanthanide-ligand bond) or the stronger crystal field splitting (lifting of the degeneracy of certain energy levels imposed by the lower symmetry of the lattice site compared to the spherically symmetric free ion) of the 5d orbitals compared to that of the 4f orbitals plays a crucial role in determining the energies at which this $4f^{n-1}5d^1$ band is located.

The poor shielding of the 5d orbitals also results in the $4f^{n-1}5d^1$ possessing shorter equilibrium bond lengths,[18] resulting in a larger Stokes shift compared to the $4f^n \leftrightarrow 4f^{n'}$ transitions, as depicted in Figure 3. Considering the even azimuthal quantum number of the d orbitals ($l = 2$) and uneven azimuthal quantum number of f orbitals ($l = 3$) and consequently even and odd parity of these orbitals respectively, the interconfigurational transitions between $4f^n$-based and $4f^{n-1}5d^1$-based electronic levels are ED allowed, resulting in higher line strengths for this type of transitions compared to the intraconfigurational $4f^n \leftrightarrow 4f^{n'}$ transitions.
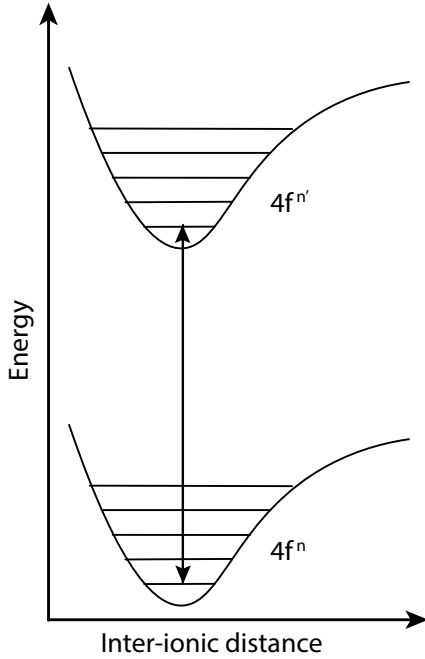

Figure 2: Configuration coordination diagram for $4f^n \leftrightarrow 4f^{n'}$ transitions within lanthanide ions.
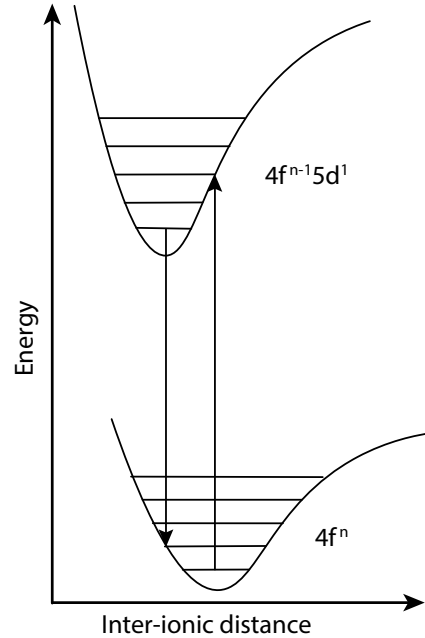
Figure 3: Configuration coordination diagram for $4f^n \leftrightarrow 4f^{n-1}5d^1$ transitions within lanthanide ions.

2.3.4 Upconversion mechanisms

The conventional UC process this thesis evolves around involves an electronic transition from a $4f^n$-based ground level to an excited $4f^{n'}$-based state, known as ground state absorption (GSA). Following the $4f^n \leftrightarrow 4f^{n'}$ GSA, absorption of a second photon can excite electrons from this intermediate $4f^{n'}$ state to the $4f^{n-1}5d^1$-configuration or a $4f^{n''}$-based level, a process known as excited state absorption (ESA). A schematic representation of this UC process is depicted in Figure 4a. Within the context of this thesis, the potential of the $4f^{n'} \leftrightarrow 4f^{n-1}5d^1$ ESA will be emphasized. Due to the requirement of two subsequent absorption processes, UC is a nonlinear absorption effect and as such less probable than GSA itself. Therefore, observation of UC typically requires high-intensity excitation sources such as lasers and sufficiently slowly decaying intermediate electronic states to enhance the ESA process. Considering the aforementioned influence of the host lattices on intensities of the $4f^n$ to $4f^{n'}$ transitions by virtue of its Judd-Ofelt parameters, selecting the right host lattice is paramount for a successful upconversion process.

Since the $4f^{n'} \leftrightarrow 4f^{n-1}5d^1$ transitions are ED allowed by virtue of the azimuthal quantum numbers of the orbitals involved, the rate for the ESA is expected to be orders of magnitude higher than that for the GSA. This minimizes the occupancy of the $4f^{n'}$ state, and as such, the changes of competitive relaxation from this $4f^{n'}$ state to lower lying energy levels, or, in the worst case, the ground state. If the orders of magnitude of the rates for the GSA and ESA are very different, the UC process may be regarded as two separate one-photon processes instead of a two-photon process. In particular, a two-photon process obeys different selection rules by means of angular momentum conservation and would thus require the orbital angular momentum quantum number ℓ to change by ± 2 for allowed interconfigurational transitions. Thus, $4f^n \leftrightarrow 4f^{n-1}5d^1$ transitions would be ED forbidden in a strict two-photon process.

Besides the previously presented example of sequential GSA and ESA, there are several other possible mechanisms for upconversion. The most efficient of these is the so-called energy transfer upconversion (ETU), in which absorption of a photon yields excitation of an electron from the ground state to an excited state within a sensitizer ion. Absorption of a second photon then results in the excitation of an electron from the ground state to an excited state in an acceptor ion, either by direct excitation or via a transfer of energy from a second excited sensitize ion. This activator ion may also be the same type of ion as the sensitizer, or a different type. The excited sensitizer ion then then non-radiatively decays back to a lower excited state or ground state and transfers the energy to the activator that is then excited to a yet higher excited state and can finally show UC from this state back to the ground state, as depicted in Figure 4b. This type of process is experimentally known to be more efficient than ESA by a factor of around 10^2.[17] As already laid down in section 1.2, the energy transfer probability rapidly decreases if the distance between the sensitizer and acceptor, which makes this mechanism only effective if the doping concentration of the acceptors is sufficiently high. In addition, other cooperative types of UC are known, and the interested reader is referred to literature for additional information.[17]
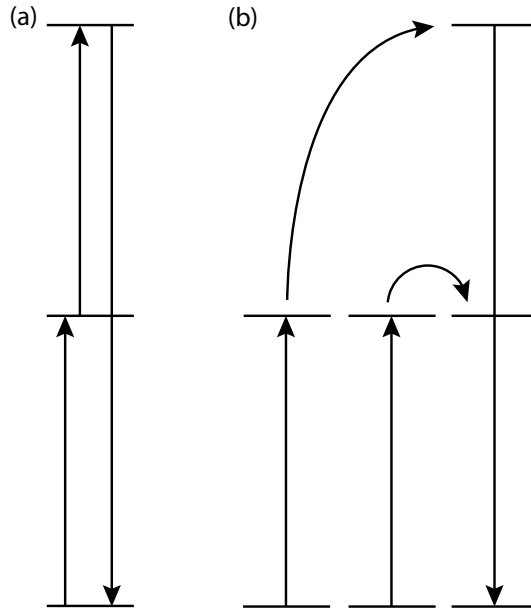

Figure 4: Schematic representation of upconversion mechanisms: (a) single-ion ground state and excited state absorption and (b) energy transfer upconversion between multiple ions.

2.4 Energy level structure of lanthanide ions

2.4.1 Energy level structure of Tm^{2+}

Tm^{2+} possesses the $[Xe]6s^24f^{13}$ electron configuration. The consequential single vacancy in the 4f orbitals within Tm^{2+} gives rise to a remarkably uncomplicated $4f^{13}$ electronic energy level scheme, as depicted in Figure 5. Since the stabilization of Tm^{2+} on air imposes specific requirements on the host lattice to be used, the differences in the position of the $4f^{12}5d^1$ electronic configuration in different host lattices known to stabilize Tm^{2+} is less pronounced than for the other lanthanide ions, but present nonetheless. The lower edge of the $4f^{12}5d^1$ absorption band for Tm^{2+} is located at an energy of approximately 17,000 cm^{-1} in the SrB_4O_7 host,[14,39] at approximately 19,000 cm^{-1} in the $SrCl_2$ host[15,40] and at approximately 13,000 cm^{-1} in both the $CsCaBr_3$ and $CsCaCl_3$ hosts.[41,42] For the purpose of upconversion, the transition between the two $4f^{13}$-based energy levels depicted in Figure 5 is to be employed as the ground state absorption, with the $4f^{13}(^2F_{\frac{5}{2}}) \rightarrow 4f^{12}5d^1$ serving as the ESA process to achieve the $4f^{12}5d^1 \rightarrow 4f^{13}(^2F_{\frac{7}{2}})$ UC emission.[15]

2.4.2 Energy level structure of Sm^{2+}

Sm^{2+} possesses the $[Xe]4f^66s^2$ electron configuration, giving rise to a more complicated $4f^6$-based energy level diagram compared to the $4f^{13}$-based energy level diagram for Tm^{2+}. This energy level diagram for the $4f^6$-based electronic levels is depicted in Figure 6. To achieve the desired $4f^55d^1 \rightarrow 4f^6(^7F_0)$ UC emission, a $^7F_0 \rightarrow ^5D_0$ GSA and $4f^6(^5D_0) \rightarrow 4f^55d^1$ ESA are to be employed. As for Tm^{2+}, the energy of the $4f^55d^1$ configuration depends on the selected host lattice, with a wider variety of host lattices available for Sm^{2+} due it being less prone to oxidation than Tm^{2+}. In the selected SrB_4O_7 host, the lower edge of the $4f^55d^1$ is located at an energy of approximately 17,000 cm^{-1}, consequently overlapping with the $4f^6$-based $^5D_2$ level.[21,24] As will be discussed in more detail in a section devoted to luminescent properties of Sm^{2+}, this may lead to a hampering in the UC process in combination with multi-phonon relaxation. The other host lattice investigated within the context of this thesis, the SrFCl host, induces a higher-energy $4f^55d^1$ configuration with a lower edge around 20,000 cm^{-1}, allowing for a more significant gain in photon energy compared to the SrB_4O_7 host.[22,23] In both hosts, however, the gain through the UC process in Sm^{2+} is low enough to make is obsolete in the light of potential applications. It would, however, make for a compelling proof of principle and allow for meaningful comparison with UC processes in other lanthanide ions.

2.4.3 Energy level structure of Pr^{3+}

Pr^{3+} possesses the $[Xe]6s^24f^2$ electron configuration. This affords a total of 91 configurations for these two electrons within the 7 4f orbitals since each orbital may be occupied by two electrons of opposite spin according to Pauli's exclusion principle. The $4f^2$-based energy levels in the range from 0 to 24,000 cm^{-1} are represented in Figure 7. In addition to the $4f^2$ electronic levels shown in this figure, Pr^{3+} also features a $^1S_0$ level with an approximate energy of 47,000 cm^{-1}, whose energy is high enough that it can be safely disregarded in the context of UC involving the $4f^15d^1$ configuration within the context of this thesis. The energy of the $4f^15d^1$ configuration depends on the host compound Pr^{3+} is incorporated into, but typically also lies in the UV energy range of the $4f^2$-based $^1S_0$ level. For a free ion, the bottom of this configuration lies at an energy of approximately 11,000 cm^{-1} above the $^1S_0$ level.[43] For Pr^{3+} ions incorporated into a host lattice, this energy is significantly lowered due to the nephelauxetic effect and crystal field splitting of the substituted site occupied by Pr^{3+}. The exact position of the lower edge of the $4f^15d^1$ band depends strongly on the nature of the host lattice, but may, for example, be as low as approximately 36,000 cm^{-1} in the case of the frequently used aluminum garnets host lattices.[44]

For the purposes of visible to ultraviolet (UV) photon upconversion, the energy levels mainly of interest are the $^1D_2$ level and the ^3P_J levels. According the reduced matrix elements for forced electric dipole transitions (see equation 7), only the absorption from the $^3H_4$ ground level to the $^3P_2$ excited level should have appreciable absorption intensity for a host compound with a large Ω_6 parameter ($|U(2)|^2 \approx 0$; $|U(4)|^2 = 0.036$; $|U(6)|)^2 = 0.1367$), given that Judd-Ofelt theory is still regarded as valid in the case of Pr^{3+}. Upon excitation into this state, rapid non-radiative relaxation to the $^3P_0$ state will occur due to the low energy separation. From here, non-radiative decay to the $^1D_0$ level is possible in hosts with high phonon energies (>1000 cm^{-1}). Depending on this phonon energy and the energy at which the lowest level in the 5d band is located is located, blue-to-UV upconverted $4f^15d^1 \rightarrow 4f^2(^3H_J)$ emission may be excited from the $^3P_0$ and/or $^1D_2$ level, respectively.[8,45] A correct energy match between the 4f and 5d levels for both types of upconversion additionally circumvents another possible problem: if the lowest excited $4f^15d^1$-based level is at slightly higher energy than the $4f^n$-based $^1S_0$ level, multi-phonon relaxation from the 5d band to the $^1S_0$ reduces the upconversion efficiency significantly by loss of the advantage of a strong ED allowed UV $4f^15d^1$ emission.
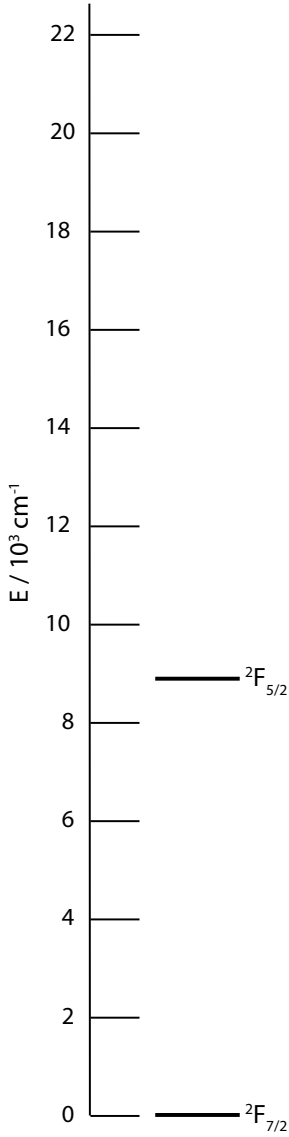
Figure 5: Energy level diagram for the $4f^{13}$-based levels of Tm^{2+}.
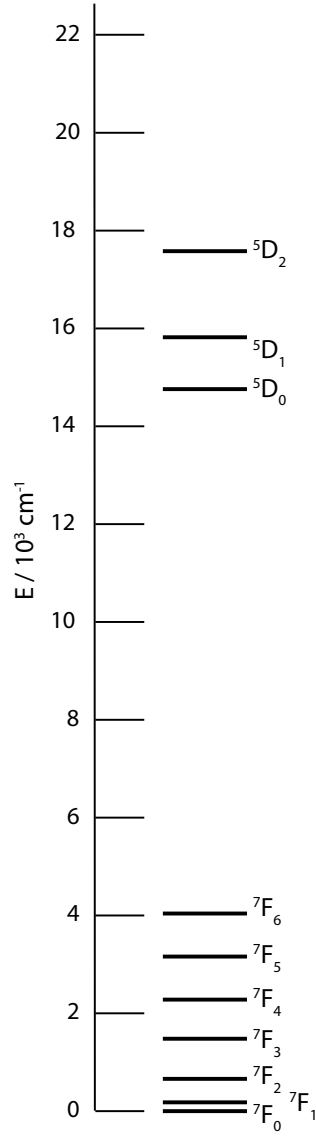

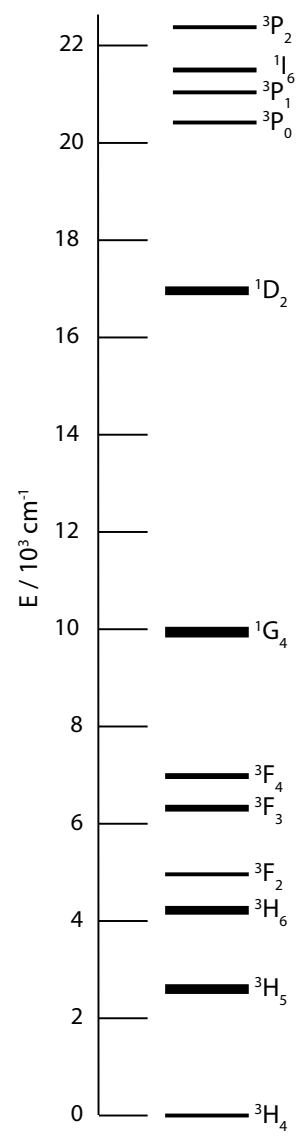Figure 6: Energy level diagram for the $4f^6$-based levels of Sm^{2+}.

Figure 7: Energy level diagram for the $4f^2$-based levels of Pr^{3+}.

3 Experimental techniques

This section covers the experimental techniques deployed within the context of this thesis. It will commence with a concise overview of the general synthesis strategy. A more precise description of the methods employed for the synthesis of the individual compounds in addition to a discussion on the viability of these methods and the quality of the synthesized compounds is given in section 4.1. A general overview of the working of a spectrometer and its vital components will be presented, as will the specifications of used equipment.

3.1 Synthetic procedures

Within the context of this thesis, all compounds investigated were prepared via a high-temperature solid-state synthesis, with the exception of $YPO_4:Pr^{3+}$, which was prepared via a co-precipitation from solution, and $LuAG:Pr^{3+}$, which was present at the research group from prior experiments. A doping concentration of 0.5 mol% was employed for the lanthanide ions relative to the ion to be substituted due to this doping concentration being considered high enough for appreciable luminescence intensities, both low enough to minimize the effects of cross-relaxation. The only exception was the already present $LuAG:Pr^{3+}$, which possessed a Pr^{3+} doping concentration of approximately 1 mol%. For all solid state synthesis performed within the context of this thesis, stoichiometric amounts of the respective starting compounds were weighed on an analytical balance, and intimately grinded with a pestle and mortar for approximately 10 minutes. Approximately 0.5 mol% of the dopant relative to the ion to be substituted was added. All used chemicals had at least reagent grade quality. During grinding, a small amount of acetone was added to allow a homogeneous mixing of the different compounds and avoid sample losses. Unless stated otherwise, samples were then transferred to alumina boats or crucibles and heated using Carbolite tube furnaces with the possibility of performing the reactions under either air, constant N_2 gas flow or constant flow of a $\sim$ 4:1 mixture of N_2 and H_2 gas. Temperature ramp and dwell time are explicitly given in each respective section. The phase purity of all synthesized samples was verified on a Philips PW1729 X-ray powder diffractometer employing Cu K$\alpha_{1,2}$ radiation. If not stated otherwise, the powder diffraction patterns were compared to simulated patterns from the Inorganic Crystal Structure Database (ICSD) of the Fachinformationszentrum (FIZ) Karlsruhe, Germany.

3.2 Spectroscopic measurements

Spectroscopic measurements were performed on an Edinburgh Instruments F900 fluorospectrometer equipped with a 450 W Xe lamp and double monochromator gratings blazed at 300 nm or 500 nm, respectively, in both the excitation and emission compartments, allowing for optimal resolution in both compartments. Luminescence was detected in a 90 °angle relative to the excitation light with a Hamamatsu R928 photomultiplier tube (PMT). Upconversion spectra and luminescence decay curves were acquired upon excitation with an Opolette 355 optical parametric oscillator (OPO) with a frequency-multiplied pump wavelength of 355 nm and tunable visible signal and infrared idler wavelengths, allowing for tuned-wavelength, high intensity pulsed excitation. The pulse frequency was 20 Hz and the maximum pulse energy at 410 nm was 9.14 mJ with a beam diameter of around 3 - 4 mm.

To acquire emission spectra, the excitation wavelength on either the Xenon lamp or the OPO was fixed, and the emission intensity was recorded over a range of wavelengths. To eliminate the excitation wavelength or its higher harmonics, originating from higher-order reflections within the monochromator compartment, a series of filters was used, with the precise filter depending on the specific requirements of the desired spectrum to be measured. Excitation spectra were acquired by varying the excitation wavelength by tuning the excitation monochromator between Xenon lamp and sample, while detecting the emission intensity at a fixed wavelength as a function of this excitation wavelength. Acquired emission spectra were corrected for the varying sensitivity of the PMT detector at different detection wavelengths using a pre-existing calibration file. Acquired emission spectra obtained through excitation through the Xenon lamp were corrected for the emission spectrum of the lamp by recording reference data. Obtained data was processed and analyzed in Python.

4 Results and discussion

In this section, the results acquired within the context of this thesis will be presented and discussed. It will start with a detailed description of the various synthetic methods and a discussion on the quality of the synthesized compounds. It will then proceed with the presentation and discussion of luminescent properties of the successfully synthesized lanthanide-doped compounds. Of these luminescent properties, intraconfigurational $4f^n \leftrightarrow 4f^{n'}$ luminescence and the $4f^n \leftrightarrow 4f^{n-1}5d^1$ (UC) luminescence will be covered. Additionally, the decay kinetics of the relevant $4f^2$-based levels in Pr^{3+} in selected host compounds will be presented and discussed.

4.1 Synthetic methods

4.1.1 Synthesis of SrB_4O_7:Tm^{2+} and SrB_4O_7:Sm^{2+}

As mentioned previously, the SrB_4O_7 host lattice is experimentally found to be very reductive in nature. In particular, it is one of the small-numbered host lattices that is reported to stabilize Tm in its divalent form on air.[39, 46] To synthesize this compound, two distinct procedures were employed.

Procedure 1

SrB_4O_7 was prepared upon mixing stoichiometric amounts of $SrCO_3$ (Aldrich, 99.9%) and H_3BO_3 (Merck, 99.8%) as starting compounds with Tm_2O_3 (Heraeus, 99.999%) and Sm_2O_3 (Schuchardt, 99.9%) as doping agents. In the first procedure,[21] a preheating step from room temperature to 300 °C with a ramp of 5 °C/min under N_2/H_2 atmosphere was employed since it was suggested that this step prevents an uncontrolled glass formation of B_2O_3. The sample mixture was kept at that temperature for 7.5 h and naturally cooled to room temperature for additional grinding. The mixture was then heated to 850 °C with 5 °C/min under N_2/H_2 atmosphere, kept at the final temperature for 8.5 h and naturally cooled down to room temperature again. Detection of a crude emission spectrum for both samples indicated successful reduction of Sm^{3+} to Sm^{2+}, but an unsuccessful reduction of Tm^{3+} to Tm^{2+}. Based on those findings, the previously described treatment at 850 °C was repeated for another time. A luminescent check-up, however, indicated a yet unsuccessful reduction of Tm^{3+} to Tm^{2+}.

Upon heating the starting compounds $SrCO_3$ and H_3BO_3 separately from room temperature to 350 °C with a ramp of 5 °C/min and a 1.5 hour dwell time, it was found that the H_3BO_3 had formed into a glassy melt, rather than the microcrystalline B_2O_3 powder. It was reported that this was a consequence the used ramp of 5 °C/min, and an alternative procedure with a lower heating rate was proposed. In this procedure, the starting compounds were again thoroughly mixed by grinding, and heated from room temperature to 350 °C for 7.5 h after a 1.5 °C/min ramp N_2/H_2 atmosphere. After intermediate grinding, the samples were heated to 850 °C for 8.5 h with a ramp of 1.5 °C/min and naturally cooled down under N_2/H_2 atmosphere. This procedure was repeated three times with intermediate grinding steps. The X-ray diffraction patterns of the resulting compounds are displayed together with respective simulated ICSD patterns for both SrB_4O_7 and the alumina sample holder in Figure 8. Since all reflections in the experimentally acquired spectra are attributable to either the SrB_4O_7 host or the Al sample holder, it may be concluded that the pure compound had formed. It should be noted that the doping concentrations of only 0.5 mol% are below the detection limit of X-ray diffraction. However, spectroscopic measurements did indicate that the reduction of Sm^{3+} to Sm^{2+} was only partially successful, whereas only minor indications of a reduction of Tm^{3+} to Tm^{2+} were observed.

Procedure 2

The second program, based on work by De Jong and Meijerink,[47] involved a prefiring step in which the grinded starting compounds were heated to 500 °C for 2 h with a ramp of 1.5 °C/min under N_2/H_2 atmosphere. After intermediate grinding, the compounds were heated to 850 °for 8 h with a ramp of 1.5 °C/min and naturally cooled down under N_2/H_2 atmosphere. The XRD patterns of the resulting compounds, along with corresponding ICSD reference patterns, are depicted in Figure 9 and indicated formation of the mostly pure SrB_4O_7 phase, although the XRD pattern of SrB_4O_7:Tm^{2+} in Figure 9b displays some low-intensity peaks for 2θ values from 25 to 30 not attributable to either the SrB_4O_7 host or the Al sample holder, hence indicating a small, yet unknown impurity.

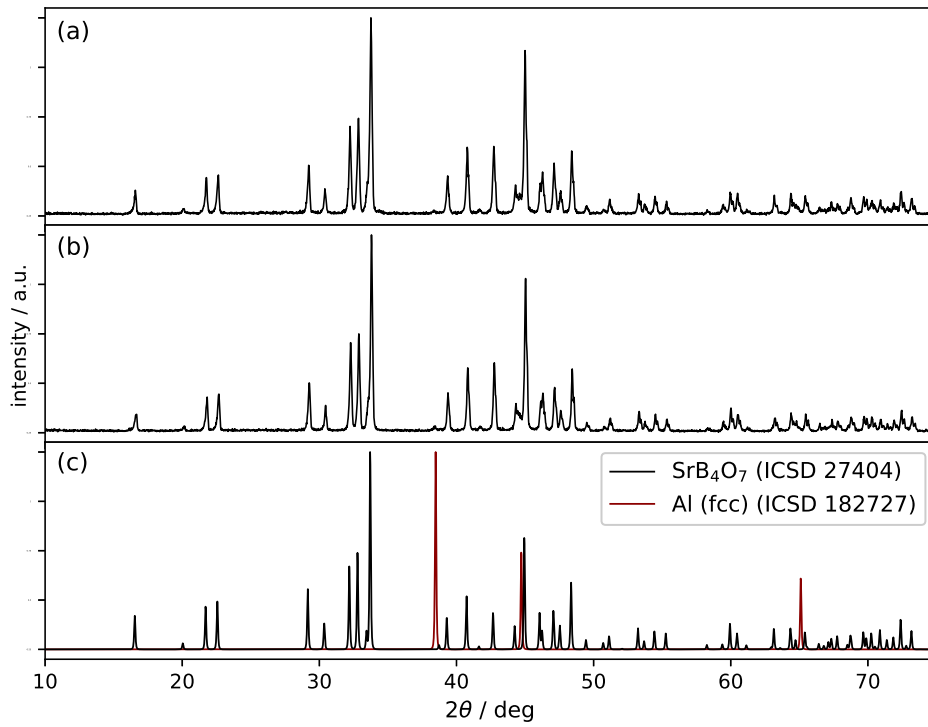Figure 8: XRD patterns for (a) synthesized SrB_4O_7:Tm^{2+}, (b) SrB_4O_7:Sm^{2+} using procedure 1, and (c) calculated ICSD patterns for SrB_4O_7 (ICSD 27404)[48] and fcc Al (ICSD 182727).[49]
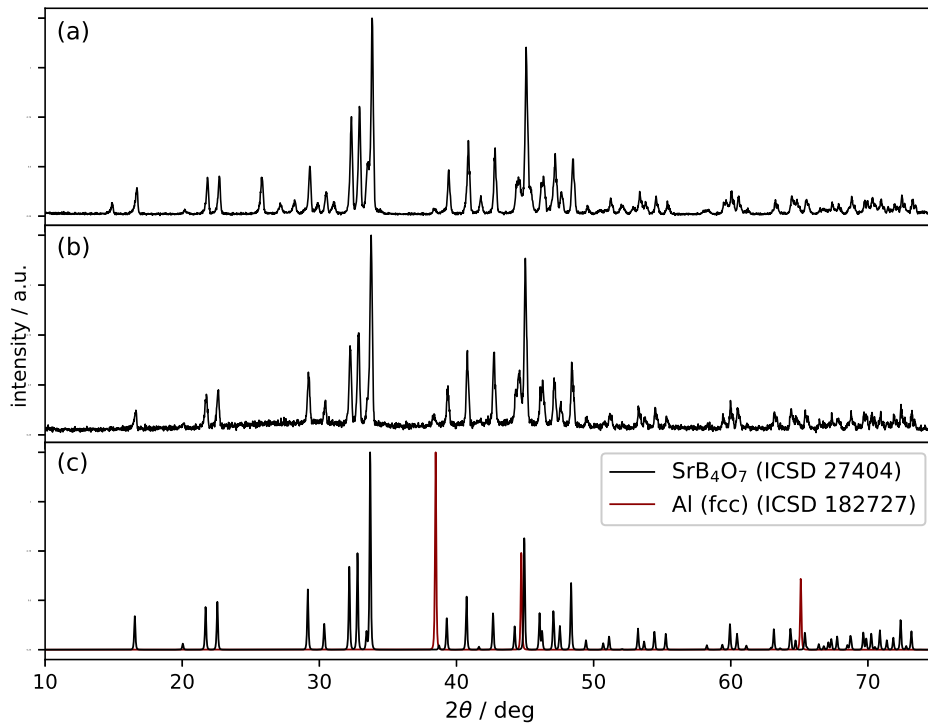
Figure 9: XRD patterns for (a) synthesized SrB_4O_7:Tm^{2+}, (b) SrB_4O_7:Sm^{2+} using procedure 2, and (c) calculated ICSD patterns for SrB_4O_7 (ICSD 27404)[48] and fcc Al (ICSD 182727).[49]

After the purity of the formed tetraborate phases was confirmed, both samples were subjected to luminescence measurements to indicate whether the reduction of Tm^{3+} and Sm^{3+} to Tm^{2+} and Sm^{2+} had been successful. Emission spectra were acquired upon direct excitation into the $4f^{n-1}5d^1$ configuration, reported to be located at 480 nm for Tm^{2+}-doped compound and at 500 nm for the Sm^{2+}-doped compound at room temperature. For Tm^{2+}, the emission spectrum is expected to display a broad emission band centered around 600 nm, attributed to the $4f^{12}5d^1 \rightarrow 4f^{13}$ ($^7F_0$) emission.[14] For Sm^{2+}, the emission spectrum is expected to display narrow emission lines, which correspond to emissions from the $^5D_0$ level to the ^7F_J (J = 0 - 6) arising from the $4f^6$ configuration. This expectation is based on the energy of the lowest state of the $4f^5 5d^1$ configuration at around 18000 cm^{-1}, overlapping with the energy of the $^5D_2$ electronic level.[50] The phonon energy in SrB_4O_7 of 1200 cm^{-1} is high enough for multi-phonon relaxation to bridge the energy gap between this $4f^5 5d^1$ configuration and the $^5D_1$ level effectively.[51] Therefore, the emission is assumed to have a maximum energy of approximately 18,000 cm^{-1}.[24]

For the allegedly synthesized SrB_4O_7:Tm^{2+}, the experimentally observed emission spectrum is displayed in Figure 10. In this spectrum, only a low intensity characteristic broad emission band around 600 nm is visible that could be attributed to the $4f^{12}5d^1 \rightarrow 4f^{13}$ emission in Tm^{2+}. Additionally, the multiple narrow emission lines observed between 550 nm and 750 nm cannot possibly be attributed to $4f^n \leftrightarrow 4f^{n'}$ transitions in Tm^{2+},[14] but can be attributed to the ^3F_J (J = 2, 3) $\rightarrow$ $^3H_{J'}$ (J' = 5, 6) transitions in Tm^{3+}.[39,52] Hence, the reduction of Tm^{3+} was unsuccessful even under reductive atmosphere, in contradiction of the reported triviality of the reduction both on air[39,46] and under reductive atmosphere.[14] A possible explanation could be an insufficient temperature insulation in the used furnace tube, resulting in an inhomogeneous temperature distribution along the center of the tube in the furnace, which may thus cause a difference between set and actual temperature. In a final attempt to achieve the desired reduction from Tm^{3+} to Tm^{2+}, the previously established program was altered such that the final step involved heating to 1100 °C with a ramp of 1.5 °C/min, both under the N_2/H_2 atmosphere and on air. These attempts, however, resulted in glassy melts unsuitable for both X-ray diffraction and luminescence measurements.

The experimentally observed emission spectrum for the allegedly synthesized SrB_4O_7:Sm^{2+} is displayed in Figure 11. The expected narrow line $4f^6(^5D_0) \rightarrow 4f^6(^7F_J)$ emissions characteristic for Sm^{2+} are observed, which indicates a successful reduction of Sm^{3+} to Sm^{2+}. The intraconfigurational $4f^6 \leftrightarrow 4f^{6'}$ transitions in Sm^{2+} will be discussed in more detail in section 4.2.1.
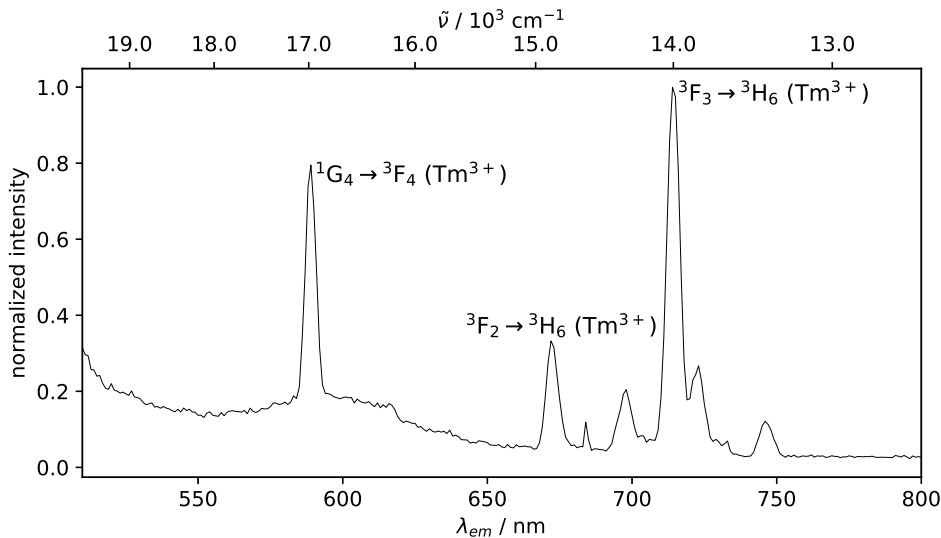

Figure 10: Emission spectrum (λ_{ex} = 480 nm) for the allegedly synthesized SrB_4O_7:Tm^{2+}
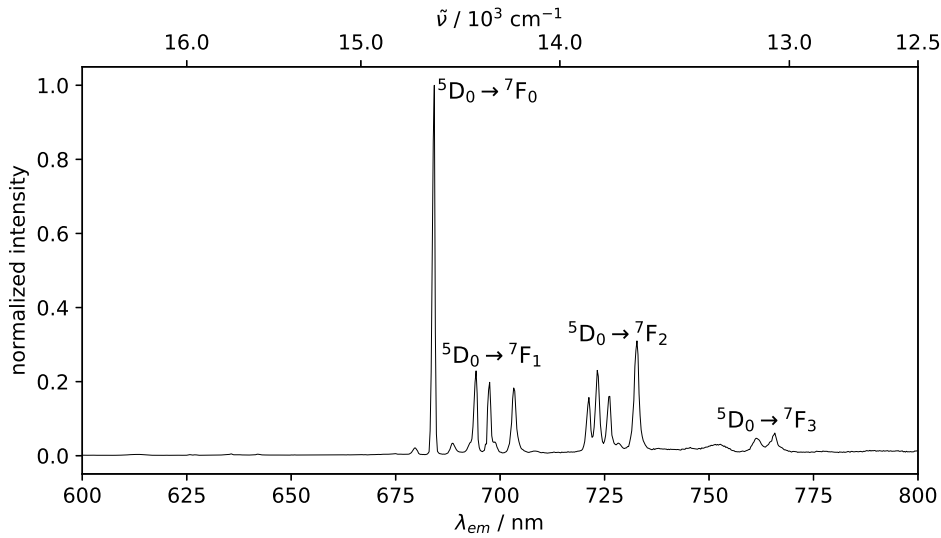
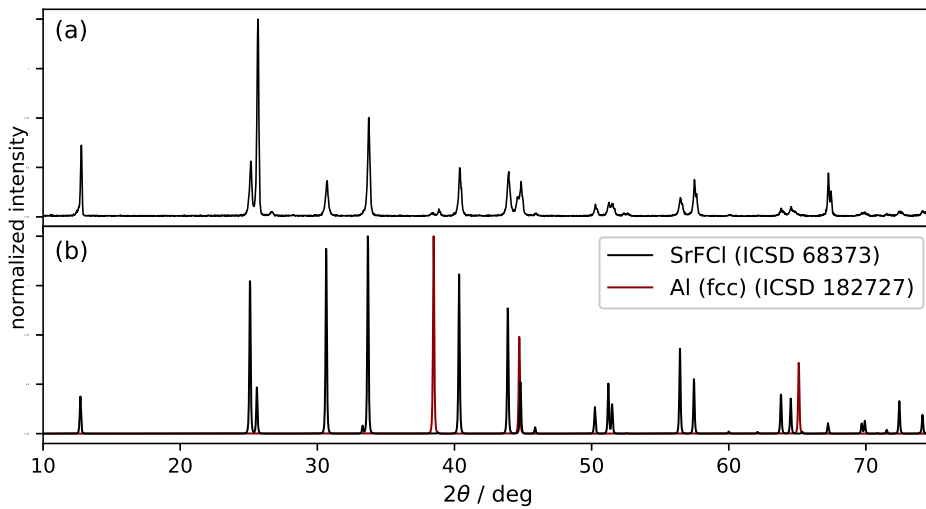Figure 11: Emission spectrum ($\lambda_{ex} = 500$ nm) for the allegedly synthesized SrB_4O_7:Sm^{2+}

Figure 12: XRD patterns for (a) the synthesized SrFCl:Sm^{2+}[53] and (b) calculated ICSD patterns for SrFCl (ICSD 68373) and fcc Al (ICSD 182727).[49]

4.1.2 Synthesis of SrFCl:Sm^{2+}

SrFCl:Sm^{2+} was synthesized from SrF_2 (Merck, P.A.) and $SrCl_2 \cdot 6H_2O$ (Merck, > 99%), with SmF_3 (Chempur, > 99.9%) being used as the Sm-dopant. After weighing and grinding, the mixture was heated to 300 °C for 5 h with a 1 °C/min heating ramp. Subsequently, the mixture was heated to 1050 °C for 20 h with a ramp of 1 °C/min without intermediate grinding step since the final temperature deployed is well above the required melting temperature of the congruently melting mixture.[54] To ensure optimal crystallinity of the final product, the cooling rate was set to 0.25 °C/min down to a temperature 850 °C, and 1 °C/min afterwards. Heating was performed in a carbon crucible under N_2/H_2 atmosphere. The desired SrFCl host lattice was formed and is phase pure, as judged by comparison between the experimentally acquired X-ray diffraction pattern and the ICSD patterns for both SrFCl and the alumina sample holder, as depicted in Figure 12.
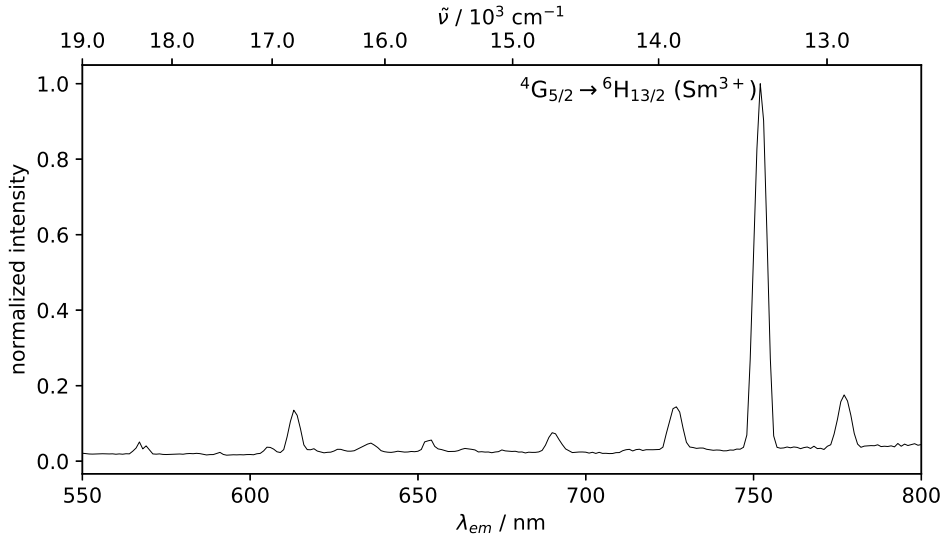
Figure 13: Emission spectrum ($\lambda_{ex} = 500$ nm) for the allegedly synthesized SrFCl:Sm^{2+}

To verify the success of the reduction of Sm^{3+} in the SrFCl host, an emission spectrum upon excitation at 500 nm was measured in analogy to the SrB$_4$O$_7$ sample. The resulting spectrum is displayed in Figure 13. Especially, the strong $4f^6(^5D_0) \rightarrow 4f^6(^7F_0)$ narrow line emission at around 684 nm characteristic for Sm^{2+} is not observed. In contrast, the slightly broadened emission peaks can be attributed to emission from various energy levels in Sm^{3+}.[55] Accordingly, the highest-intensity peak at 752 nm is attributed to the $^4G_{\frac{5}{2}} \rightarrow {}^6H_{\frac{13}{2}}$ emission.[52] Hence, the reduction of Sm^{3+} to Sm^{2+} was unsuccessful in the SrFCl host. This reduction is both theoretically expected and experimentally observed to be more challenging than the same reduction in the SrB$_4$O$_7$ host, but is reported to be possible on certain reductive conditions.[22,23] Since the synthesis of the host lattice itself was successful, the lacking reduction was also attributed to temperature inhomogenieties along the center of the tube as previously described for the attempted reduction of Tm^{3+} in the SrB$_4$O$_7$ host. Future studies will be necessary, however, to verify this hypothesis.

4.1.3 Synthesis of LaBO$_3$:Pr^{3+}

LaBO$_3$:Pr^{3+} was synthesized from La$_2$O$_3$ (Merck, P.A.) and H$_3$BO$_3$ (Merck, 99.8%), with Pr(CH$_3$COO)$_3 \cdot x$H$_2$O (Alfa Aesar, > 99%) being used as Pr^{3+} dopant source, in a manner similar to the SrB$_4$O$_7$ host lattice. Stoichiometric amounts of the starting materials together with 0.5 mol% of the Pr-dopant were thoroughly grinded and then thermally treated. They were first heated to 300 °C for 2 h with a heating rate of 1.5 °C/min under N$_2$ atmosphere. After intermediate grinding back at room temperature, the mixture was fired at 850 °C for 8 h with a heating rate of 1.5 °C/min. Finally, the sample was naturally cooled down and regrinded. The X-ray diffraction analysis (see Figure 14) indicates the formation of phase pure microcrystalline LaBO$_3$:Pr^{3+}.
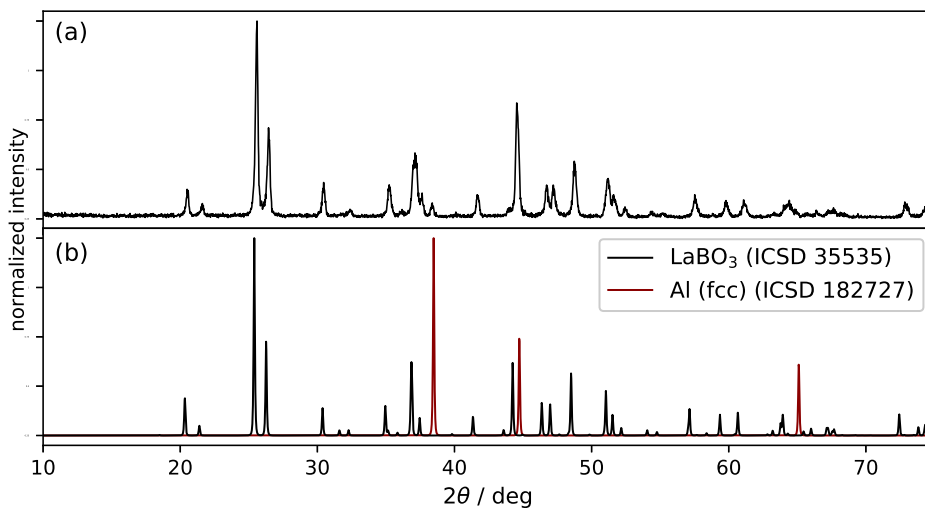
Figure 14: XRD patterns for (a) the synthesized LaBO$_3$:Pr^{3+} and (b) calculated ICSD patterns for LaBO$_3$ (ICSD 35535)[56] and fcc Al (ICSD 182727).[49]

4.1.4   Synthesis of YPO$_4$:Pr^{3+}

YPO$_4$:Pr^{3+} was synthesized by a co-precipitation from Y(NO$_3$)$_3$·6H$_2$O (Aldrich, 99.8%) and Pr(NO$_3$)$_3$·6H$_2$O (Stem Chemicals, 99.9%) as the Pr^{3+} dopant and (NH$_4$)$_2$HPO$_4$ (Fluka, >90%) as a precipitating agent. For synthesis, stoichiometric amounts of Y(NO$_3$)$_3$ and Pr(NO$_3$)$_3$ to achieve the desired 0.5 mol% Pr^{3+} doping concentration were weighted and dissolved in deionized water. A stoichiometric excess of (NH$_4$)$_2$HPO$_4$ was dissolved in deionized water separately. The pH of the phosphate solution was set to ∼ 8.0 by addition of a few μl of 2M aqueous NaOH solution. The phosphate solution was then added to the nitrate solution in 0.5 mL steps with 2 min. intervals under magnetic stirring, upon which colourless precipitate formed. Afterwards, the precipitated phosphate was allowed to sediment at the bottom and the solution carefully diluted with deionized water. After 2 hours the upper layer of solution was decanted, after which the precipitate was washed with water three more times and the remaining water was evaporated in a 150 °C oven on air. The X-ray diffraction pattern, in comparison to the simulated ICSD pattern, is displayed in Figure 15 and indicates the formation of pure microcrystalline YPO$_4$:Pr^{3+}.

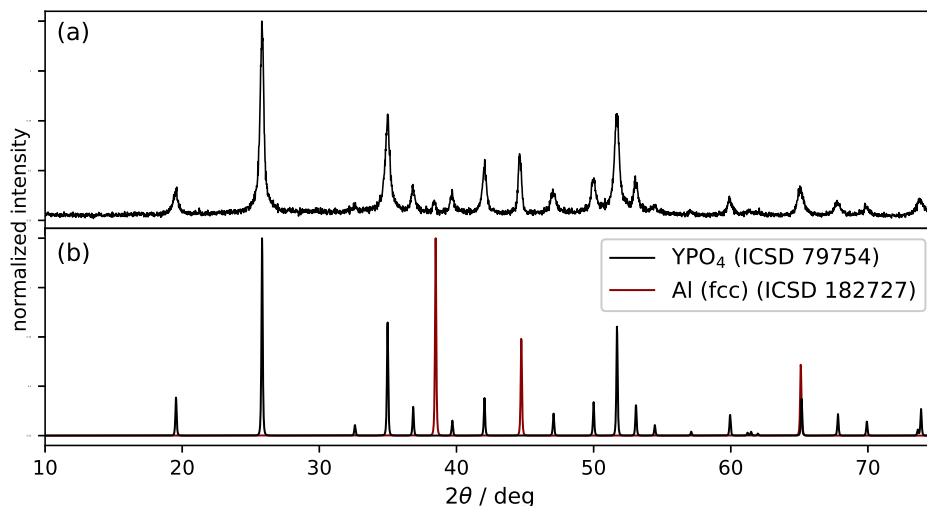Figure 15: XRD patterns for (a) the synthesized YPO$_4$:Pr^{3+} and (b) calculated ICSD patterns for YPO$_4$ (ICSD 79754)[57] and fcc Al (ICSD 182727).[49]

4.2 Luminescent features of SrB_4O_7:Sm^{2+}

In the SrB_4O_7 host, the lowest edge of the $4f^5 5d^1$ configuration in Sm^{2+} is located at an energy of approximately 18,000 cm^{-1}, overlapping with the $4f^6(^5D_2)$ level.[24,50] This feature, combined with the SrB_4O_7 host having a high phonon energy of $\sim$ 1200 cm^{-1},[51] readily leads to multi-phonon relaxation into the ^5D_J states upon excitation into the $4f^5 5d^1$ configuration from the $4f^2$-based $^7F_0$ ground level or the $^5D_0$ excited level. This poses a significant challenge to any attempted observation of upconversion of Sm^{2+} in this host compound, as multi-phonon relaxation back to the $^5D_0$ level would quench the upconversion. Therefore, it was first investigated whether emission from the $^5D_0$ or the $^5D_1$ levels in the Sm^{2+} ions could be detected upon direct excitation into the $4f^5 5d^1$ configuration. Absence pf these emissions would indicate the quenching any potential UC luminescence by this multi-phonon relaxation.

Additionally, the proximity of the ^5D_J levels to the bottom of the $4f^5 5d^1$ band would lead to a very small anti-Stokes shift of the upconversion emission, as the emission from the $^5D_1$ would only be around 1500 cm^{-1} higher in energy than the excitation energy upon excitation into the 1500 cm^{-1} lower lying $^1D_0$ level.[23,24] Although this would not provide any gain in a successful upconversion process, it may be an insightful example for the usage of $4f^{n-1}5d^1$ configurations in upconversion processes within lanthanide ions. Moreover, it allows for direct comparisons to the mainly investigated Pr^{3+} ion in the context of upconversion. Finally, it is also an excellent example of the competitive energy transfer processes and its effect on the upconversion process.

4.2.1 $4f^6 \leftrightarrow 4f^{6'}$ luminescence

To characterize the intraconfigurational $4f^6 \leftrightarrow 4f^{6'}$ luminescence in SrB_4O_7:Sm^{2+}, an emission spectrum upon 500 nm $4f^6(^7F_0) \rightarrow 4f^5 5d^1$ excitation, which is depicted in Figure 16. All observed peaks are attributed to emission originating from the $^5D_0$, with the highest-intensity emission peak attributed to the $^5D_0 \rightarrow {}^7F_0$ emission. The absence of emission from the $^5D_2$ level is also expected, as this level overlaps with that of the $4f^5 5d^1$ configuration. Additionally, the absence of luminescent decay from the $^5D_1$ indicates the prevalence of the multi-phonon relaxation from this level to the $^5D_0$ state. This transition is highly forbidden to an extent to which emission originating from the $^5D_1$ level is typically observed in the iso-electric Eu^{3+}.[23,52] However, the energy gap between $^5D_0$ and $^5D_1$ levels is somewhat lower for Sm^{2+}, probably causing the yet efficient multi-phonon relaxation. Thus, the multi-phonon relaxation in this host is already efficient enough to hamper upconversion processes at room temperature.

In addition to the previously presented narrow line emission spectrum upon $4f^6(^7F_0) \rightarrow 4f^5 5d^1$ excitation, an excitation spectrum upon detection of the $4f^6(^5D_0) \rightarrow 4f^6(^7F_0)$ emission at 684 nm was measured, which is depicted in Figure 17. In contrast to the previously presented emission spectrum, the spectrum consists of three broad bands, which can be attributed to excitations from the $4f^6$ levels into the $4f^5 5d^1$ configuration. Since the $4f^5 5d^1$ band covers a large energy range, assigning the bands to excitation from single states is only crudely possible, but allows the conclusion that the absorption offset lowest excited $4f^5 5d^1$ states are in fact positioned at around 18,000 cm^{-1} above the $^7F_0$ ground level.
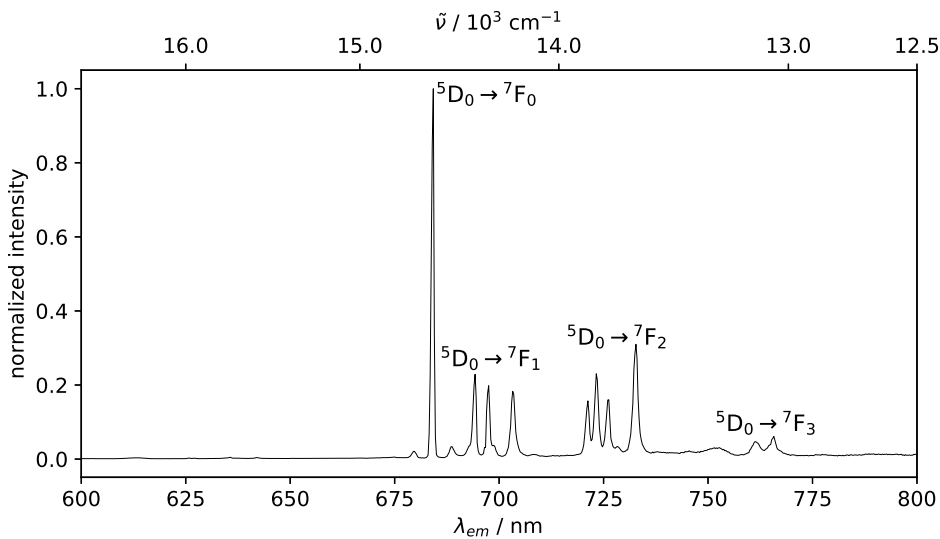

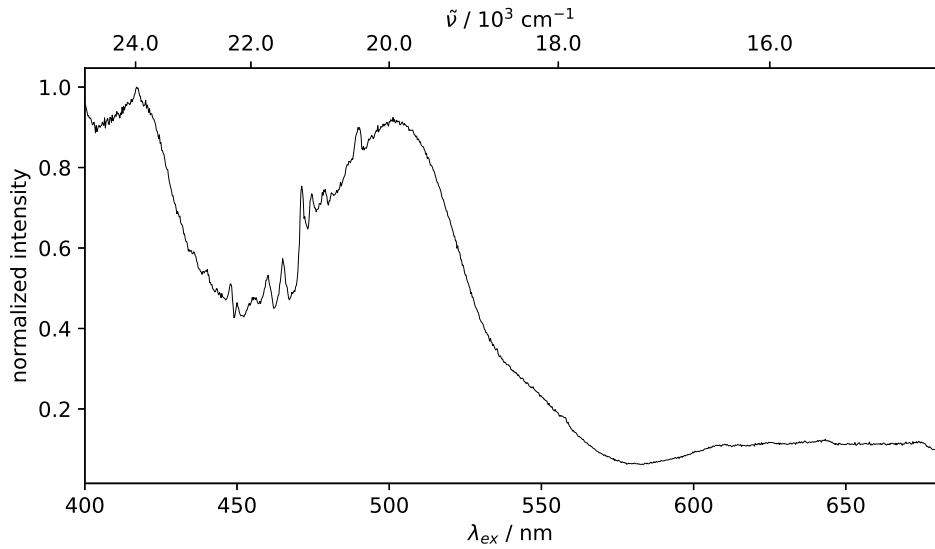Figure 16: Emission spectrum ($\lambda_{ex} = 500$ nm) of SrB_4O_7:Sm^{2+}

Figure 17: Excitation spectrum (λ_{em} = 684 nm) of SrB$_4$O$_7$:Sm^{2+}
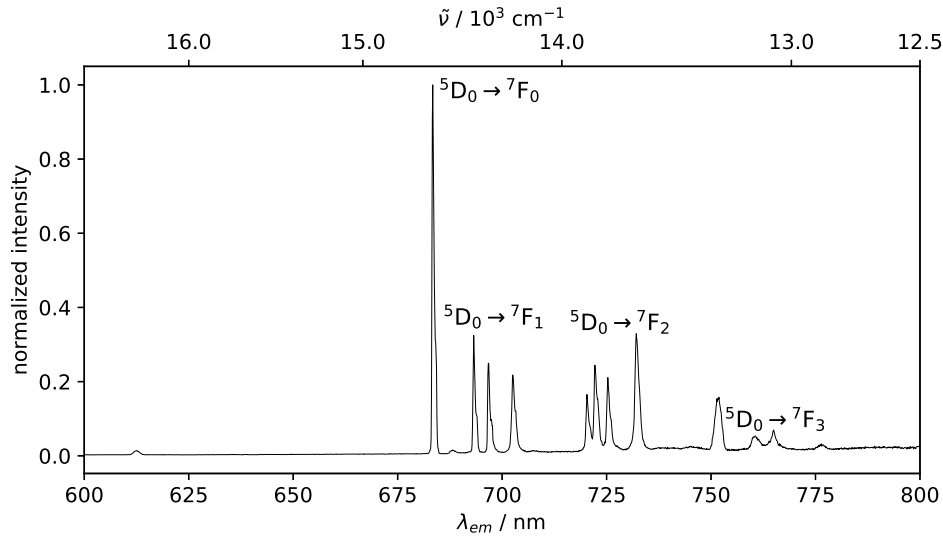

Figure 18: Emission spectrum (λ_{ex} = 500 nm) of SrB$_4$O$_7$:Sm^{2+}, measured at 4K

Since emission from neither the 4f^{5}5d^1 configuration or the ^{5}D$_2$ and ^{5}P$_1$ 4f^6-based levels upon direct 4f^6(^{7}F$_0$) $\rightarrow$ 4f^{5}5d^1 excitation was observed due to multi-phonon relaxation at room temperature, luminescence measurements on SrB$_4$O$_7$:Sm^{2+} were repeated at 4K, since the relaxation rate of the forbidden ^{5}D$_1$ $\rightarrow$ ^{5}D$_0$ transition through multi-phonon relaxation diminishes with lower temperature. Therefore, the required emission from the ^{5}D$_1$ level might be observable at these cryogenic temperatures. An emission spectrum upon 500 nm excitation of Sm^{2+} ions is depicted in Figure 18. No emission from the electronic levels above the ^{5}D$_0$ level is observed, indicating that multi-phonon relaxation between the ^{5}D$_1$ and ^{5}D$_0$ levels is even sufficiently efficient at these low temperatures. This clearly illustrates that SrB$_4$O$_7$ is not a suitable host for efficient red-to-red upconversion including an ESA to the excited 4f^{5}5d^1 configuration.

For the sake of completeness, an excitation spectrum of Sm^{2+} in SrB$_4$O$_7$ monitoring the ^{5}D$_0$ $\rightarrow$ ^{7}F$_0$ emission at 684 nm was also measured at 4K. This spectrum is displayed in Figure 19, and shows great resemblance to the same excitation spectrum measured at room temperature. The 4K excitation spectrum does also displays two broad 4f^6(^{5}F$_J$) $\rightarrow$ 4f^{5}5d^1 absorption bands at the same positions as the excitation bands in the spectrum measured at room temperature. In addition, some low-intensity excitation lines are observed around λ_{ex} = 550 nm. These transitions could possibly be related to the vibronic fine structure, which has frequently been observed in the SrB$_4$O$_7$ host doped with divalent lanthanide ions.[14,58,59] Several excitation lines are also observed between 420 and 425 nm. As the energy associated with these wavelengths exceeds the energy of the highest-energy intraconfigurational 4f^6 $\leftrightarrow$ 4f$^{6'}$ transition and the 4f^6 $\rightarrow$ 4f^{5}5d^1 transitions not displaying such narrow line transitions, these peaks may be dismissed as artifacts arising from residual signals of the employed Xe lamp and an interpretation will be disregarded here.
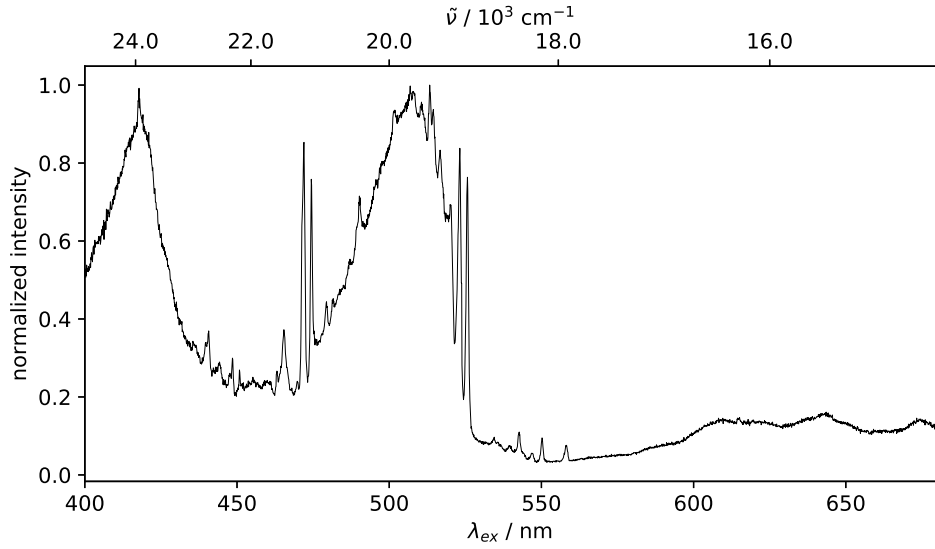
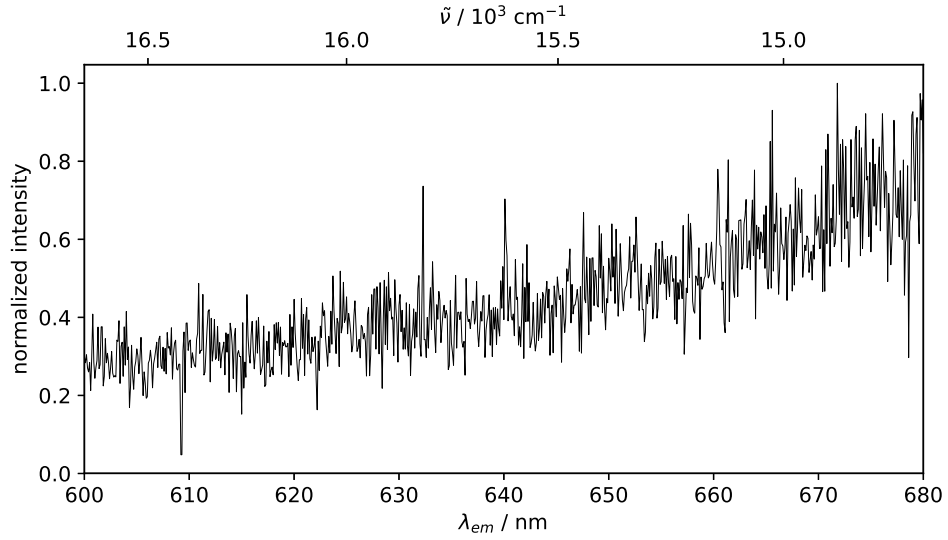Figure 19: Excitation spectrum ($\lambda_{\text{em}} = 684$ nm) of SrB_4O_7:Sm^{2+}, measured at 4K

Figure 20: Anti-Stokes emission spectrum of SrB_4O_7:Sm^{2+} ($\lambda_{\text{ex}} = 684$ nm, OPO) measured at 4K.

4.2.2 Attempts at upconversion luminescence

Besides the previous discussion on an absence of $4f^6(^5D_1) \rightarrow 4f^6(^7F_J)$ emission upon $4f^6(^7F_0) \rightarrow 4f^55d^1$ excitation at 4 K being an indication for efficient multi-phonon relaxation between the $^5D_1$ and $^5D_0$ levels of Sm^{2+} in SrB_4O_7, a definite proof on a consequently lacking upconversion signal was attempted. A corresponding anti-Stokes emission spectrum upon $4f^6(^7F_0) \rightarrow 4f^6(^5D_0)$ ($\lambda_{\text{ex}} = 684$ nm) excitation with an OPO, is depicted in Figure 20. As evident from this Figure, no upconversion signal was detected, again illustrating that SrB_4O_7 is no suitable choice as a host material for the upconversion with Sm^{2+}.

4.3 Luminescent features of LaBO$_3$:Pr^{3+}

In LaBO$_3$:Pr^{3+}, the bottom of the 4f^{1}5d^1 configuration is located approximately 42,500 cm^{-1} above the ^{3}H$_4$ ground level,[60] which would require the upconversion emission to be achieved via 4f^6(^{3}H$_4$) $\rightarrow$ 4f^6(^{3}P$_2$) GSA and a subsequent 4f^6(^{3}P$_0$) $\rightarrow$ 4f^{1}5d^1 ESA upon $\sim$ 450 nm excitation. As the intraconfigurational 4f^2 $\leftrightarrow$ 4f$^{2'}$ luminescence is similar in all Pr^{3+}-activated compounds, a discussion on the respective photoluminescence spectra in this section will also serve as a foundation for the discussion on the other Pr^{3+}-compounds in the context of this thesis. Following the characterization of this 4f^2 $\leftrightarrow$ 4f$^{2'}$ luminescence, the results on the upconversion luminescence will then be presented and discussed. Finally, decay kinetics of the relevant 4f^2-based levels will be presented discussed, which will also serve as a foundation for the discussion of decay kinetics of the other two Pr^{3+}-doped host lattices.

4.3.1 4f^2 $\leftrightarrow$ 4f$^{2'}$ luminescence

As stated previously, the 4f^2-based electronic levels of particular interest for 4f^{1}5d^1 $\rightarrow$ 4f^2(^{3}HJ) UC emission are the ^{1}D$_2$ and ^{3}P$_J$ levels. Comparing the reduced electric dipole matrix elements for the transition between these states and the ^{3}H$_4$ ground state, the reduced matrix element for $\lambda = 6$ is found the be especially large for the transition between the ^{3}H$_4$ and ^{3}P$_2$ levels. Combined with Ω_6 being the largest of the Judd-Ofelt parameters of Pr^{3+} in the LaBO$_3$ host, the ^{3}H$_4$ $\leftrightarrow$ ^{3}P$_2$ transition is expected to have a high absorption cross section. To characterize the 4f^2 $\leftrightarrow$ 4f$^{2'}$ luminescence experimentally, several emission and excitation spectra were taken in the energy range of these transitions. An emission spectrum upon excitation at $\lambda_{ex} = 446$ nm, corresponding to the ^{3}H$_4$ $\rightarrow$ ^{3}P$_2$ transition,[52] is depicted in Figure 21. Two distinct groups of emission peaks are observed, one at approximately $\lambda_{em} = 480$ nm and one at approximately $\lambda_{em} = 600$ nm, respectively. The former is attributed to the ^{3}P$_0$ $\rightarrow$ ^{3}H$_4$ emission, considering the efficient ^{3}P$_2$ $\rightarrow$ ^{3}P$_0$ multi-phonon relaxation due to their low energy separation, whereas the latter is attributed to the ^{1}D$_2$ $\rightarrow$ ^{3}H$_4$ emission. The relatively high intensity of the emission originating from the ^{1}D$_2$ level indicates an efficient population of this level through multi-phonon from the ^{3}P$_0$ level, readily explained by the high maximum phonon energy ($\hbar\omega = 1300$ cm^{-1})[61] of the LaBO$_3$ host.

An emission spectrum upon ^{3}H$_4$ $\rightarrow$ ^{1}D$_2$ excitation of LaBO$_3$:Pr^{3+} ($\lambda_{ex} = 580$ nm) is depicted in Figure 22. Three emission peaks, attributed to transitions originating from the ^{1}D$_2$ level, are observed. Compared to the emission spectrum upon ^{3}H$_4$ $\rightarrow$ ^{3}P$_2$ excitation (see Figure 21), the intensity of the emissions upon ^{3}H$_4$ $\rightarrow$ ^{1}D$_2$ excitation is significantly lower, as indicated by the lower signal-to-noise ratio. It is proposed that this is a consequence of the ^{3}H$_4$ $\rightarrow$ ^{1}D$_2$ excitation being considerably less efficient than the previously presented ^{3}H$_4$ $\rightarrow$ ^{3}P$_2$ excitation, in agreement with the smaller reduced matrix elements for the former transition due to its spin-forbidden nature and higher stability of the ^{1}D$_2$ level.
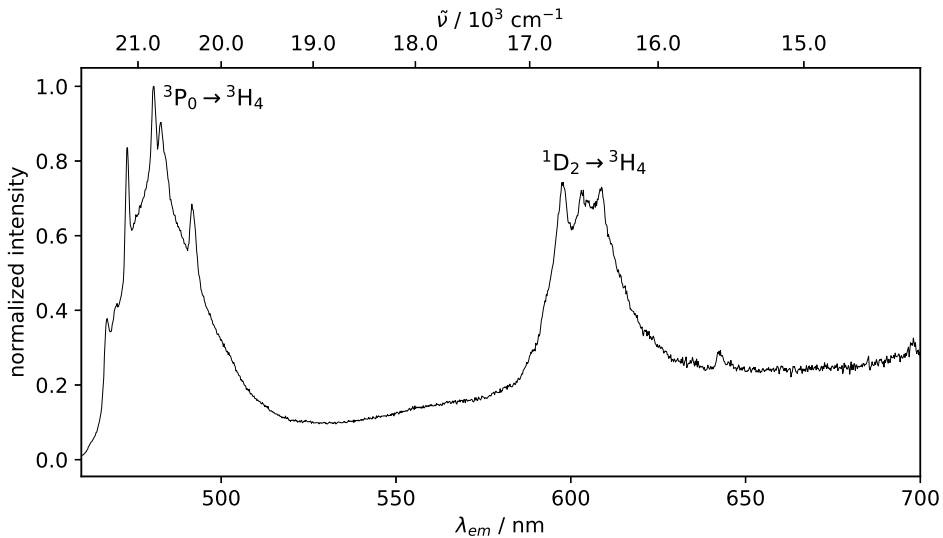

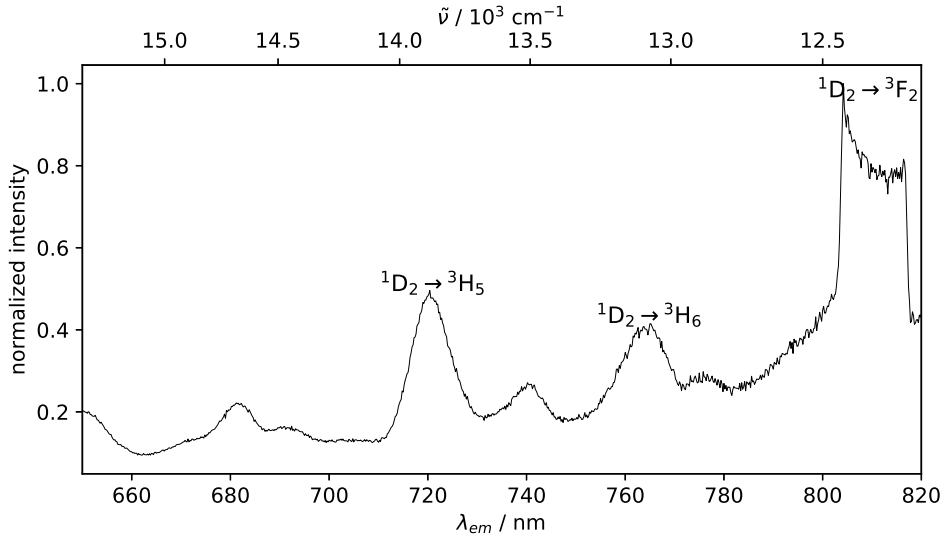
Figure 21: Emission spectrum ($\lambda_{ex} = 446$ nm) of LaBO$_3$:Pr^{3+}

Figure 22: Emission spectrum ($\lambda_\text{ex} = 580$ nm) of $LaBO_3$:Pr^{3+}
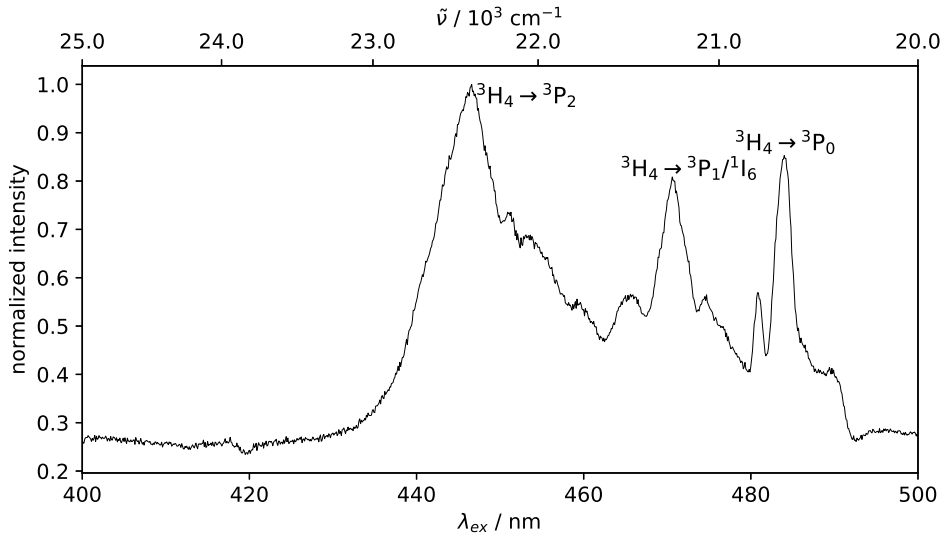

Figure 23: Excitation spectrum ($\lambda_\text{em} = 609$ nm) of $LaBO_3$:Pr^{3+}

In addition to the previously presented emission spectra, an excitation spectrum upon monitoring the emission at $\lambda_\text{em} = 609$ nm, corresponding to the $^1D_2 \rightarrow {}^3H_4$ emission,[52] is depicted in Figure 23. As mentioned in section 2.4.3, a Judd-Ofelt analysis on $LaBO_3$:Pr^{3+} predicts a particularly high line strength for the $^3H_4 \rightarrow {}^3P_2$ absorption. The excitation spectrum seems to strengthen this prediction since the $^3H_4 \rightarrow {}^3P_2$ excitation transition most efficiently induces luminescence from the $^1D_2$ level. For an experimental appreciation, however, absorption spectra would be necessary to justify the predictions from Judd-Ofelt theory more quantitatively. Two lower-intensity excitation peaks attributed to excitation into the $^1I_6/{}^3P_1$ and $^3P_0$ levels are also observed at excitation wavelengths of 473 nm and 485 nm, respectively. Since the measurements were performed at room temperature, $^3P_1$ and $^1I_6$ levels overlap significantly due to additional Stark splitting in the crystalline environment together with vibronic broadening and thus, hamper a high resolution at room temperature. Predictions on highest absorption intensities of the $4f^2 \leftrightarrow 4f^2$ transitions of Pr^{3+} in the $LaBO_3$ host together with the matching energy of the lowest edge of the $4f^1 5d^1$ configuration, it was decided to investigate upconversion primarily through 451 nm excitation.

4.3.2 Upconversion luminescence

As stated previously, both position of the energy of the $4f^2(^3H_4) \to 4f^15d^1$ absorption transition at around 42,500 cm^{-1}[51] and favourable line strengths for the $^3H_4 \leftrightarrow {}^3P_2$ transition make $LaBO_3$:Pr^{3+} a promising sample for an efficient $4f^15d^1 \to 4f^2(^3HJ)$ UC luminescence transition via ESA from the $^3P_0$ level. The UC was excited with a (pulsed) OPO and the $4f^2(^3H_4) \to 4f^2(^3P_2)$ transition located at 451 nm was used as a GSA.

The anti-Stokes emission spectra upon 451 nm OPO excitation for excitation powers ranging from 0.45 to 1.00 relative to the maximum excitation power for emission wavelengths from 234 nm to 250 nm are depicted Figure 24a. A broad emission band centred around 240 nm is observed, corresponding to the $4f^15d^1 \to 4f^2(^3H_J)$ upconverted emission. The upconverted emission intensity as a function of the relative OPO excitation power is depicted in Figure 24b. The errors reported are estimated are based on the estimated errors in assessing the set integration boundaries of the emission band, as it was assumed the numerical error of the integration of the emission band itself. The measuring error inherent to the used equipment measuring emission with a signal-to-noise ratio as low as the signal-to-noise ratio observed for the UC emission is impossible to be quantitatively taken into account. This does, however, significantly increase the error in the observed UC emission intensities. This is especially true for the lower excitation powers, to a point where the UC emission intensity at excitation powers lower than 0.5 may not be deemed physical altogether.

As expected, an increase in intensity is observed for the higher laser powers. At relative incident laser powers larger than 0.70 of the maximum laser power, the intensities evolve into a linear behavior on a double-log scale indicating a rational power dependence of the intensity. Linear regression on the power dependent intensities for relative excitation powers from 0.75 to 1.00 resulted in a slope of 1.14 ± 0.10, suggesting a saturation regime and and to a large extent agreeing with the linear relation between power and UC intensity in the high-power limit.[62] For lower indicent laser powers, a slope of 2 could be obtained through a similar regression, but considering the gradually increasing slope for the lower laser powers, the value for this slope is greatly influenced by the selection of data points used in the regression. Hence, these results should not be interpreted quantitatively and future studies with continuous wave (CW) excitation will be necessary to address the UC performance more quantitatively. For even lower laser powers, the slope far exceeds the theoretical slope of 2.00 for a two-photon process. This observed deviation from theoretical predictions is attributed to the pulsed excitation nature of the OPO rather than a CW laser source. At lower laser power, the UC process may be additionally hampered by the 10 ns pulse width of the OPO. A second aspect to consider is the high background level. Several reasons may be related to this artifact. On the one hand, the UC signal may be too weak due to the pulsed excitation nature of the OPO. Moreover, the OPO beam was unfocused to avoid laser-induced overheating of the sample. On the other hand, the wavelength range of the Pr^{3+}-based $4f^15d^1 \to 4f^2(^3H_J)$ UC emission was at the sensitivity edge of the employed PMT. A vacuum UV-sensitive PMT might be more helpful in accurate detection of the corresponding UC emission intensity.
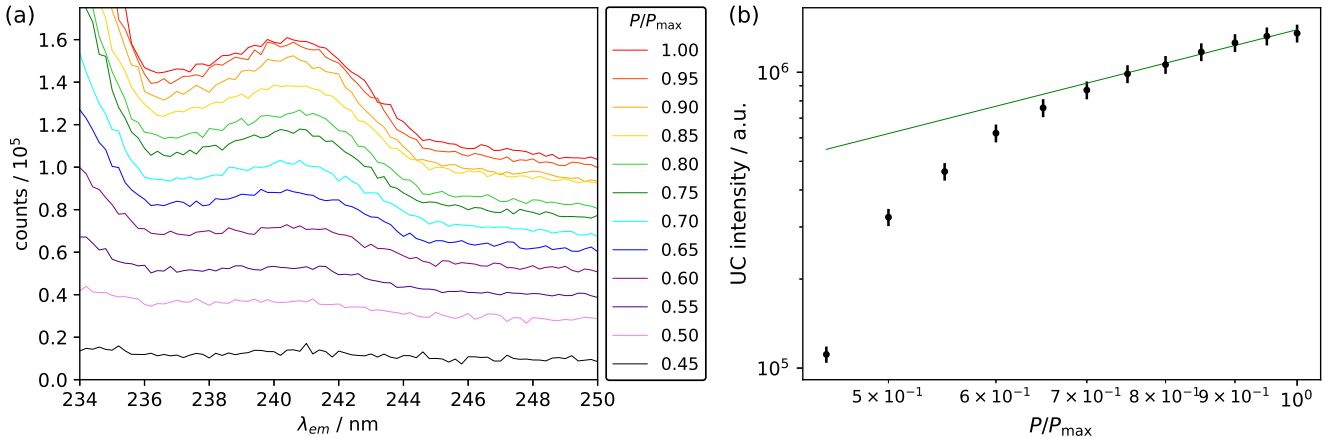

Figure 24: (a) Anti-Stokes upconversion emission spectrum of $LaBO_3$:Pr^{3+} ($\lambda_{ex} = 451$ nm, OPO) between 234 nm and 250 nm at various relative excitation powers and (b) UC emission intensity, obtained by numerical integration of the spectra between $\lambda_{em} = 235.25$ nm and $\lambda_{em} = 244.25$ nm, as a function of relative OPO power, with the linear regression over relative excitation powers from 0.75 to 1.00 ($\chi^2_{red} = 2.8 \cdot 10^{-4}$).

In addition to the previous results, the anti-Stokes emission spectra in the range between 215 nm and 236 nm acquired upon 451 nm OPO excitation for excitation powers ranging from 0.45 to 1.00 relative to the maximum excitation power are depicted in Figure 25a. A broad emission band centered around $\lambda_{em} = 224$ nm is observed, whose position does not match with the reported energy of the $4f^5 1d^1 \rightarrow 4f^2(^3H_J)$ emission in Pr^{3+}-activated LaBO$_3$.[60,63] It is assumed that this band is an artifact of the spectrometer that may be removed upon usage of a bandpass filter. This was not attempted for this sample, as its energy is too high to interline with any potential UC emission. It will be, however, considered for the YPO$_4$:Pr^{3+} sample, for which a similar feature was observed. The intensity of this signal as a function of the relative OPO excitation power is displayed in Figure 25b. For the higher laser powers, the increase of the UC intensity with laser power incident laser power appears to show a linear correlation on a double logarithmic scale. Linear regression over the logarithm of the UC intensity as a function of the logarithm of the relative laser power for laser powers from 0.75 to 1.00 results in a slope of 1.41 $\pm$ 0.28, which is statistically significantly different from a slope of one within the given error margin. For lower relative laser powers, a gradually decreasing slope for decreasing laser power in observed. The difference in power dependency compared to the results depicted in Figure 24 may possibly be interpreted as indicative for an artifact rather than a real emission originating from the LaBO$_3$:Pr^{3+} sample. However, this should be done with care, as the low signal-to-noise ratio and correspondingly high unquantifiable error in the UC emission intensities result in the values for the slopes being unreliable.
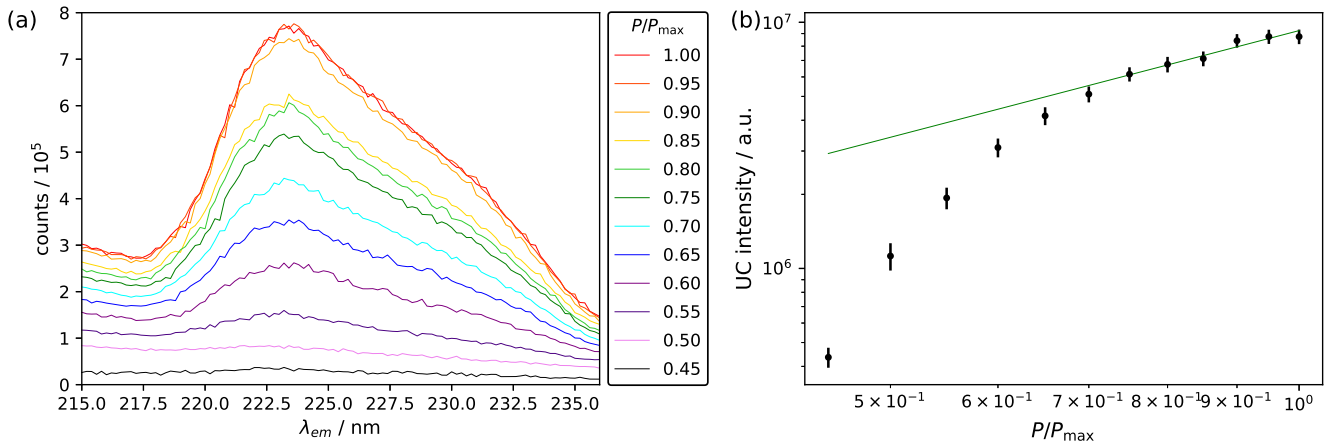

Figure 25: (a) Anti-Stokes upconversion emission spectrum of LaBO$_3$:Pr^{3+} ($\lambda_{ex} = 451$ nm, OPO) between 234 nm and 250 nm at various relative laser powers and (b) anti-Stokes emission intensity, obtained by numerical integration of the spectra between $\lambda_{em} = 218.50$ nm and $\lambda_{em} = 236.00$ nm, as a function of relative OPO power, with the linear regression over relative excitation powers from 0.75 to 1.00 ($\chi^2_{red} = 8.1 \cdot 10^{-4}$).

4.3.3 Decay analysis

To further elucidate on the UC mechanism, decay curves for the relevant 4f²-based levels in Pr³⁺ were measured. Decay curves for the $^3P_0 \rightarrow \,^3H_4$ (λ_{em} = 485 nm) emission were measured upon $^3H_4 \rightarrow \,^3P_2$ (λ_{ex} = 451 nm) and $^3H_4 \rightarrow \,^3P_0$ (λ_{ex} = 480 nm) excitation. For the $^1D_2 \rightarrow \,^3H_4$ emission (λ_{em} = 615 nm) decay curves were measured using the two aforementioned excitation transitions into the $^3P_2$ and $^3P_0$ 4f²-based levels, in addition to direct $^3H_4 \rightarrow \,^1D_2$ (λ_{ex} = 580 nm) excitation.

The situation upon excitation into either the $^3P_1$ or $^3P_2$ levels, from which feeding into the $^3P_0$ level takes place, is depicted in Figure 26. Based on this scheme and the assumed feeding ratios β_i, the decay kinetics should be identical upon excitation into the $^3P_2$ and $^3P_1$ states. For the case in which the $^3P_0$ level is occupied, the population dynamics of the $^1D_2$ and $^3P_0$ levels, denoted as states $|1\rangle$ and $|2\rangle$, are given by

$$\frac{dN_1}{dt} = \beta_1 N^* - k_{r_1} - k_{nr}^{abs} g_2 N_1 + k_{nr}^{em} g_1 N_2 \tag{8}$$

$$\frac{dN_2}{dt} = \beta_2 N^* - k_{r_2} N_2 + k_{nr}^{abs} g_2 N_1 - k_{nr}^{em} g_1 N_2 \tag{9}$$

Here, N^* denoted the population of the $^3P_{1,2}$ states, k_{nr}^{em} and k_{nr}^{abs} denote the rate of non-radiative multi-phonon relaxation and absorption, respectively, between states $|1\rangle$ and $|2\rangle$, k_{r_1} and k_{r_2} denote the rate of radiative decay of states $|1\rangle$ and $|2\rangle$, respectively, and g_1 and g_2 denote the degeneracy of states $|1\rangle$ and $|2\rangle$ respectively. Normalizing equations 8 and 9 with respect to N^* and re-writing in matrix form yields

$$\begin{pmatrix} \dot{n_1} \\ \dot{n_2} \end{pmatrix} = \begin{pmatrix} -k_{r_1} - k_{nr}^{abs} g_2 & k_{nr}^{em} g_1 \\ k_{nr}^{abs} g_2 & -k_{r_2} - k_{nr}^{em} g_1 \end{pmatrix} \begin{pmatrix} n_1 \\ n_2 \end{pmatrix} + \begin{pmatrix} \beta_1 \\ \beta_2 \end{pmatrix} \tag{10}$$

Since the energy gap between states $|1\rangle$ and $|2\rangle$ is approximately 4000 cm⁻¹,[52,64] multi-phonon absorption in the LaBo₃ host lattice with a phonon energy of around 1300 cm⁻¹ becomes negligibly small, such that the assumption $k_{nr}^{abs} g_2 = 0$ is feasible. The simplification of this linear system of differential equations in equation 10 allows it to be analytically solved. Upon imposing the initial conditions $n_1(0) = 0$ and $n_2(0) = n_{02}$, the final solution becomes

Figure 26: Simplified decay kinetics diagram for Pr³⁺ upon excitation into the ^3P_J levels.

$$\begin{pmatrix} n_1(t) \\ n_2(t) \end{pmatrix} = n_{02} \begin{pmatrix} \frac{k_{nr}^{em} g_1}{k_{r_1} - k_{r_2} + k_{nr}^{em} g_1} (e^{-k_{r_1} t} - e^{-k_{r_2} + k_{nr}^{em} g_1 t}) \\ e^{-(k_{r_2} + k_{nr}^{em} g_1 t)} \end{pmatrix} + \begin{pmatrix} \frac{\beta_1}{k_{r_1}} + \frac{\beta_2 k_{nr}^{em} g_1}{k_{r_1}(k_{r_2} - k_{nr}^{em} g_1)} \\ \frac{\beta_1}{k_{r_2} - k_{nr}^{em} g_1} \end{pmatrix} \tag{11}$$

Based on this solution, the $^1D_2$ and $^3P_0$ levels are expected to respectively display bi-exponential and single-exponential decay upon excitation into the ^3P_J levels, respectively. Upon direct excitation into the $^1D_2$, a single exponential decay of the intensity of the $^1D_2 \rightarrow \,^3H_4$-based emission is expected considering the isolation of this energy level and corresponding absence of competing decay processes. The decay curves presented in both this section and the sections on decay analysis of the other Pr³⁺ activated compounds are corrected for the purposes of the decay analysis. The uncorrected decay curves may be found in appendix A.

The decay curves upon monitoring the $^3P_0 \rightarrow \,^3H_4$ emission upon excitation into the $^3P_2$ and $^3P_0$ levels are depicted in Figure 27. Both curves display a similar biexponential decay, in contradiction to the theoretical prediction of equation 11. One possible explanation is cross-relaxation.[60] However, no conclusive evidence supporting this explanation was found. Although the relatively low doping concentration of 0.5 mol% was chosen to diminish such a competitive process, Pr³⁺ is known to be extremely susceptible to cross-relaxation,[4] which may be additionally enhanced by clustering of Pr³⁺ ions.[9] Regardless of the cause, the bi-exponential decay is expected to posses a single-exponential component representing the $^3P_0 \rightarrow \,^3H_4$ emission. Hence, a bi-exponential function of the form $I = Ae^{-t/\tau_1} + Be^{-t/\tau_2} + C$ was fitted to the decay curves, represented by the red regression lines in Figure 27. The decay components were found to be (5.47 ± 0.04) µs and (36.9 ± 0.4) µs for 451 nm excitation, and (7.985 ± 0.018) µs and (35.1 ± 0.8) µs for 480 nm excitation.
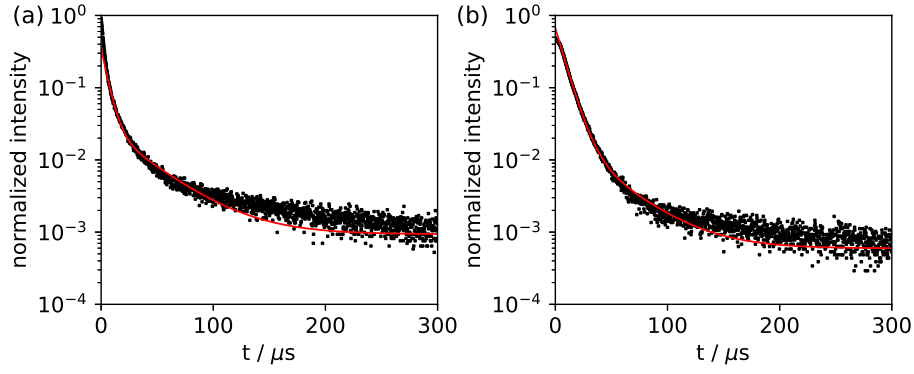
Figure 27: Luminescence decay curves of the Pr^{3+} $^3P_0 \rightarrow$ $^3H_4$ emission (λ_{em} = 485 nm) in the $LaBo_3$ host upon (a) $^3H_4 \rightarrow$ $^3P_2$ (λ_{ex} = 451 nm) and (b) $^3H_4 \rightarrow$ $^3P_0$ (λ_{ex} = 480 nm) excitation.

The decay curves upon monitoring the $^1D_2 \rightarrow$ $^3H_4$ emission upon excitation into the $^3P_2$, $^3P_0$ and $^1D_2$ levels are depicted in Figure 28. For excitation into the ^3P_J levels, bi-exponential decay is observed. However, equation 11 predicts a rise time caused by the feeding from the $^3P_0$ level, which is not observed. This is attributed to the energy of the $^1D_2 \rightarrow$ $^3H_4$ emission being very similar to that of the $^3P_0 \rightarrow$ $^3H_6$, which may be competing upon excitation into the ^3P_J levels due to the emission large slit width used. Hence, a bi-exponential function was fit to the decay curves in Figures 28a and b. The decay components were found to be (2.669 ± 0.008) μs and (36.16 ± 0.12) μs for 451 nm excitation, and (1.364 ± 0.004) μs and (33.79 ± 0.09) μs for 480 nm excitation. For excitation into the $^1D_2$ level, the expected single-exponential decay is observed. From a single exponential function fitted to the decay curve in Figure 28c, corresponding to the red regression line, a decay time of (28.32 ± 0.10) μs was found.

Lifetimes of the $^3P_0$ level have been reported for a variety of hosts, and range from ~2 μs for the Yi_2SiO_5 (YSO) host,[9] to ~ 42 μs for the ZBLAN glass[65] and 55-60 μs for the BaY_2F_8 host.[66] One trend observed in every host, however, is the shorter lifetime of the $^3P_0$ compared to the $^1D_2$,[9,65,66] caused by the spin-forbidden nature of transitions originating from the latter.[67,68] Reported lifetimes of the $^1D_2$ level are also greatly influenced by the choice of host lattice, ranging from 1.6-56 μs for the YSO host[9] to well over 500 μs for the ZBLAN glass[65] and certain occupied hosts in the $Y_4Al_2O_9$ (YAM) host.[5] Based on this observation and the decay times found upon fitting the $^1D_2$ decay curves, the shorter of the two found decay components upon monitoring the 485 nm emission is attributed to the $^3P_0$ lifetime. Hence, reported lifetimes of the $^3P_0$ level are (5.47 ± 0.04) μs and (7.985 ± 0.018) μs for 451 nm and 480 nm excitation respectively. Likewise, the longer of the two decay components upon monitoring the 615 nm emission is attributed to the $^1D_2$ lifetime. Hence, reported lifetimes of the $^1D_2$ level are (36.16 ± 0.12) μs, (33.79 ± 0.09) μs and (28.32 ± 0.10) μs for 451 nm, 480 nm and 580 nm excitation, respectively. A separation of the radiative and non-radiative contributions to the decay time (eq. 11) by means of fitting to the data is not viable due to derivation of the observed decay curves from predictions based on equation 11.
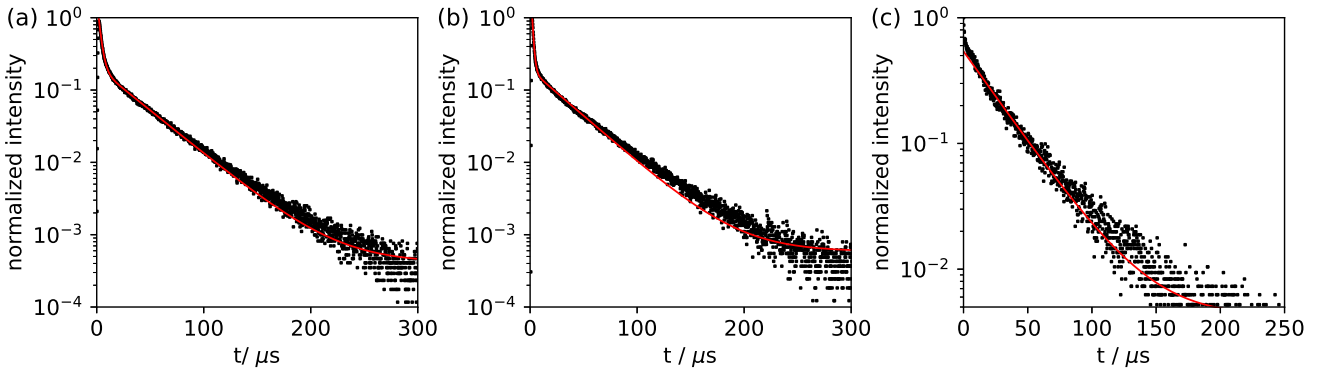

Figure 28: Luminescence decay curves of the Pr^{3+} $^1D_2 \rightarrow$ $^3H_4$ emission (λ_{em} = 615 nm) in the $LaBO_3$ host upon (a) $^3H_4 \rightarrow$ $^3P_2$ (λ_{ex} = 451 nm), (b) $^3H_4 \rightarrow$ $^3P_0$ (λ_{ex} = 480 nm) and (c) $^3H_4 \rightarrow$ $^1D_2$ (λ_{ex} = 580 nm) excitation.

While the decay times found for the two $4f^2$-based electronic levels differ significantly based on the excitation wavelengths, they are of the same order of magnitude as those reported in literature for a variety of host lattices, with the $^1D_2$ possessing a longer lifetime. Considering the 10 ns pulse width of the OPO, the lifetimes recorded for the $^3P_0$ level indicate that the two steps in the UC process, the GSA and the ESA, are required to occur within a single excitation pulse, as the $^3P_0$ level is not appreciably populated 50 μs after excitation. However, since the $^3H_4 \rightarrow ^3P_2$ GSA is quite inefficient, the UC process may be hampered by the pulse width. Based on this, $4f^55d^1 \rightarrow 4f^2(^3H_J)$ UC emission may be most efficiently excited through $4f^2(^3H_4) \rightarrow 4f^2(^3P_2)$ GSA, followed by a non-radiative multi-phonon relaxation to the $^1D_2$ $4f^2$-based level and finally, $4f^2(^1D_2) \rightarrow 4f^15d^1$ ESA. However, as stated previously, the energy of a 451 nm photon is insufficient to bridge the energy gap between the $^1D_2$ level and the lower edge of the $4f^55d^1$ configuration in the LaBO$_3$ host. This may explain the relatively low intensity of the UC emission observed in Figure 24. The found lifetimes of both the $4f^2$ levels are several orders of magnitude higher than the reported lifetime of 12.7 ns[60] of the $4f^15d^1$ levels of Pr^{3+} in LaBO$_3$ and similar lifetimes for other Pr^{3+} host lattices,[60,69] naturally explained by the parity-allowed nature of the $4f^15d^1 \leftrightarrow 4f^2$ transitions.

4.4 Luminescent features of YPO$_4$:Pr^{3+}

In the YPO$_4$ host, the lower edge of the 4f^{1}5d^1 absorption band in Pr^{3+} is located at a slighter higher energy compared to the position in the LaBO$_3$ host, starting at approximately 44,000 cm^{-1} above the 4f^2(^{3}H$_4$) level.[60,70] This energy is a high-energy limiting case regarding the position of the 4f^{1}5d^1 configuration for UC purposes, as it is theoretically just low enough to allow for 4f^2(^{3}H$_4$) $\rightarrow$ 4f^2(^{3}P$_2$) GSA and sequential 4f^2(^{3}P$_J$) $\rightarrow$ 4f^{1}5d^1 ESA to achieve the 4f^{1}5d^1 $\rightarrow$ 4f^2(^{3}H$_J$) UC emission. In analogy to LaBO$_3$:Pr^{3+}, the intraconfigurational 4f^2 $\leftrightarrow$ 4f$^{2'}$ luminescence will be briefly discussed, followed by a more in-depth discussion on the UC luminescence and the decay kinetics of the relevant 4f^2-based levels.

4.4.1 4f^2 $\leftrightarrow$ 4f$^{2'}$ luminescence

As previously stated, the chemical nature of the host lattice has a strong influence on the 5d wavefunctions, unlike the well-shielded 4f wavefunctions. Since the effect of the change in 5d wavefunctions on the 4f wavefunctions is negligible, the situation for Pr^{3+} is assumed to be virtually identical between the LaBO$_3$ and YPO$_4$ hosts. An emission spectrum upon ^{3}H$_4$ $\rightarrow$ ^{3}P$_2$ excitation (λ_{ex} = 446 nm) is depicted in Figure 29. This spectrum displays some resemblance to its analogy in LaBO$_3$:Pr^{3+} (see Figure 21), with groups of emission peaks attributed to both the ^{3}P$_0$ $\rightarrow$ ^{3}H$_4$ emission and ^{1}D$_2$ $\rightarrow$ ^{3}H$_4$ emission being observed with the former again possessing a higher intensity, were the ^{3}P$_0$ and ^{1}D$_2$ levels are both populated through efficient multi-phonon relaxation from the ^{3}P$_2$ level. One striking difference however, is the presence of a broad emission band centered around λ_{em} = 515 nm. The broadness of this band cannot possibly be attributed to an intraconfigurational 4f^2 $\leftrightarrow$ 4f$^{2'}$ transition, as those are characterized by narrow emission and absorption lines. It is hence discarded as an artefact present despite the heavy use of filters employed while acquiring this spectrum.

An emission spectrum upon ^{3}H$_4$ $\rightarrow$ ^{1}D$_2$ excitation (λ_{ex} = 580 nm) is depicted in Figure 30. As expected, this spectrum shows great resemblance to the analogous spectrum for LaBO$_3$:Pr^{3+} (see Figure 22), displaying a low signal-to-noise ratio spectrum with three emission peaks attributed to the low-intensity ^{1}D$_2$ $\rightarrow$ ^{3}H$_5$, ^{1}D$_2$ $\rightarrow$ ^{3}H$_6$ and ^{1}D$_2$ $\rightarrow$ ^{3}F$_2$ emissions. In analogy to the LaBO$_4$:Pr^{3+} sample, this is assumed to be a consequence of the ^{3}H$_4$ $\rightarrow$ ^{1}D$_2$ excitation being significantly more inefficient than the ^{3}H$_4$ $\rightarrow$ ^{3}P$_2$ excitation by virtue of the respective reduced matrix elements for both transitions and corresponding lower occupation of the ^{1}D$_2$ level.
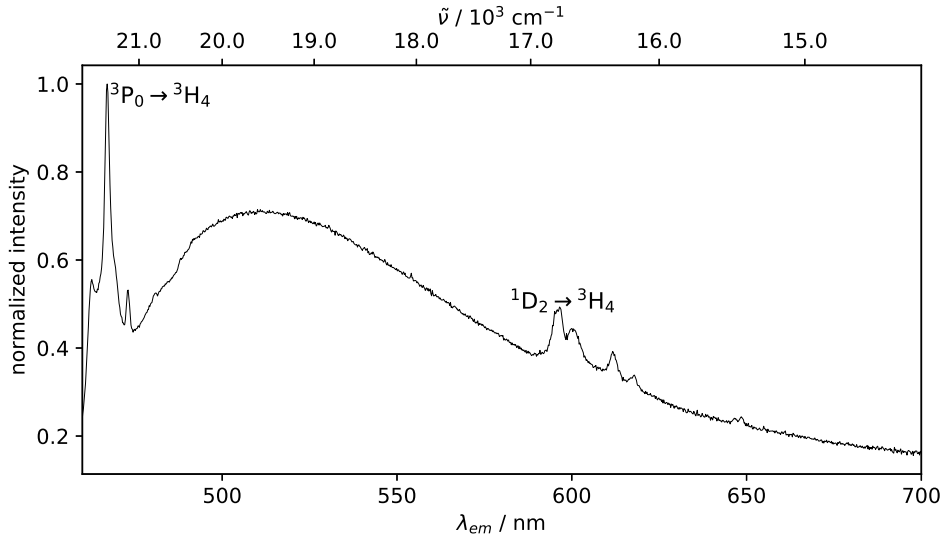

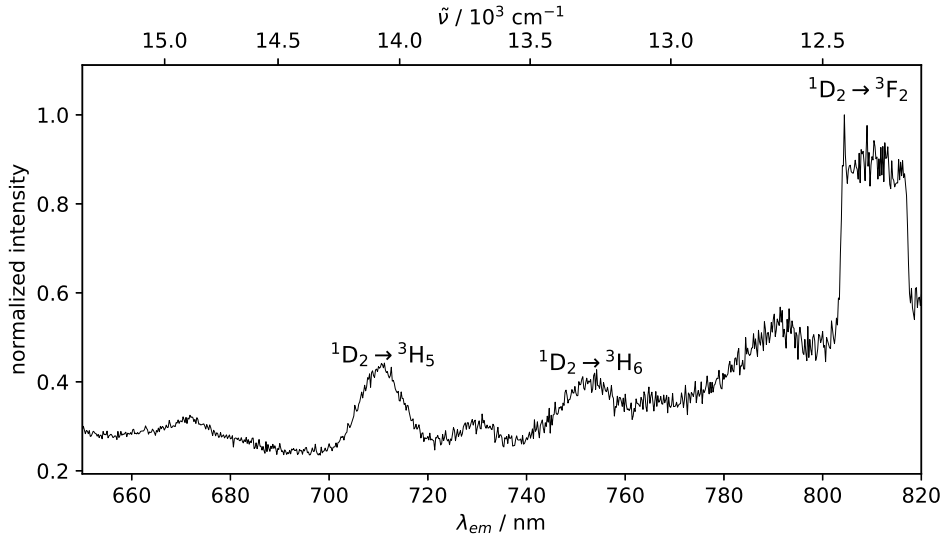Figure 29: Emission spectrum (λ_{ex} = 446 nm) of YPO$_4$:Pr^{3+}

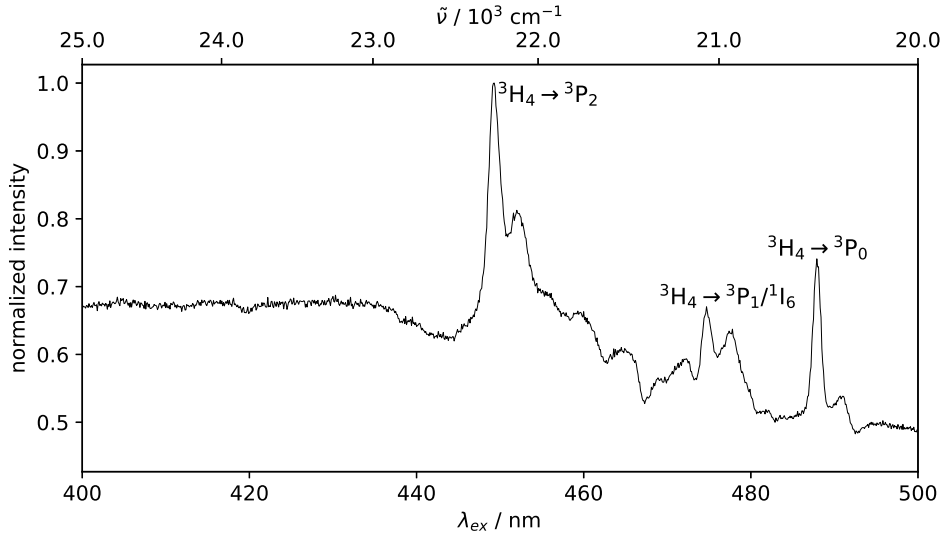Figure 30: Emission spectrum ($\lambda_{\text{ex}} = 580$ nm) of YPO$_4$:Pr^{3+}

Figure 31: Excitation spectrum ($\lambda_{\text{em}} = 609$ nm) of YPO$_4$:Pr^{3+}

An excitation spectrum upon monitoring the $^1D_2 \rightarrow {}^3H_4$ emission ($\lambda_{\text{em}} = 609$ nm) is displayed in Figure 31. Similar to the excitation spectrum for LaBO$_3$:Pr^{3+} in Figure 23, the highest-intensity excitation peak is attributed to the $^3H_4 \rightarrow {}^3P_2$ excitation, conforming with the high line strength for the $^3H_4 \rightarrow {}^3P_2$ excitation at $\lambda_{\text{ex}} = 451$ nm predicted by the Judd-Ofelt parameters of Pr^{3+}. Two additional excitation peaks are observed at excitation wavelengths of 475 nm and 488 nm, attributed to the $^3H_4 \rightarrow {}^3P_1/{}^1I_6$ and $^3 \rightarrow {}^3P_0$ transitions, respectively. Based on the intensities of these intraconfigurational $4f^2 \leftrightarrow 4f^{n'}$ transitions, the feasibility of investigating the upconversion process primarily through $4f^2(^3H_4) \rightarrow 4f^2(^3P_2)$ GSA using 451 nm excitation was confirmed.

4.4.2 Upconversion luminescence

The position of the lower edge of the $4f^15d^1$ configuration absorption band theoretically allows for a $4f^15d^1 \rightarrow 4f^2(^3H_J)$ UC emission via sequential $4f^2(^3H_4) \rightarrow 4f^2(^3P_2)$ GSA and $4f^2(^3P_0) \rightarrow 4f^15d^1$ ESA under monochromatic 451 nm excitation. The anti-Stokes emission spectra upon 451 nm OPO excitation of YPO_4:Pr^{3+} with relative excitation powers from 0.45 to 1.00 in the wavelength range between 215 and 240 nm, are depicted in Figure 32a. As was the case for $LaBO_3$:Pr^{3+}, a broad emission band centered around 224 nm is observed. Considering this wavelength is nearly equal to half the excitation wavelength, it was proposed this peak may be an artifact originating from the emission monochromator allowing the excitation radiation to pass through. In order to account for this potential artefact, a band pass filter only allowing passage of radiation with the desired emission wavelength ($\lambda_{em} \sim 210 - 250$ nm) was placed between sample and emission monochromator. The placement of this filter did not result in an appreciable drop in intensity of the emission peak. Unlike in $LaBO_3$:Pr^{3+} however, the emission band in YPO_4:Pr^{3+} displays an additional shoulder around an emission wavelength of 230 nm. Since the position of this shoulder agrees with the reported position of the $4f^15d^1 \rightarrow 4f^2(^3H_4)$ emission in YPO_4:Pr^{3+},[60,70] it was proposed that the presence of this shoulder is attributable to the aforementioned UC emission overlapping with the more intense emission band of unknown origin.

Due to the overlap of the UC emission signal with the emission peak of unknown origin, regression over the sole UC signal was not possible. Hence, the power dependence was analyzed via integration of the whole emission peak. The power dependence of this peak integral on a double logarithmic scale is depicted in Figure 32b. Like for $LaBO_3$:Pr^{3+}, the low signal-to-noise ratio makes the UC intensities for the lowest relative excitation powers more inaccurate. Similarly to $LaBO_3$:Pr^{3+}, a gradually decreasing slope for higher excitation powers is observed, eventually saturating for relative excitation powers of 0.75 and higher. Linear regression on the logarithm of the UC intensity as a function of the logarithm of the relative excitation power in the high-power limit yielded a slope of 1.10 ± 0.08. This agrees with the linear dependency predicted by the ESA process being more efficient than the GSA process. Additionally, the theoretically predicted quadratic dependence for the low-power regime is not observed, which may be attributed either to the overlap with another signal or, as proposed for $LaBO_3$:Pr^{3+}, to the OPO being a pulsed excitation source. It should however be noted, the observed power dependence behaviour is not irrevocably attributable to the upconversion emission due to the overlap with the peak of unknown origin and a similar power dependence behaviour being observed for a similar peak in the anti-Stokes emission spectra of $LaBO_3$:Pr^{3+} without the overlapping UC emission signal (see Fig. 25).
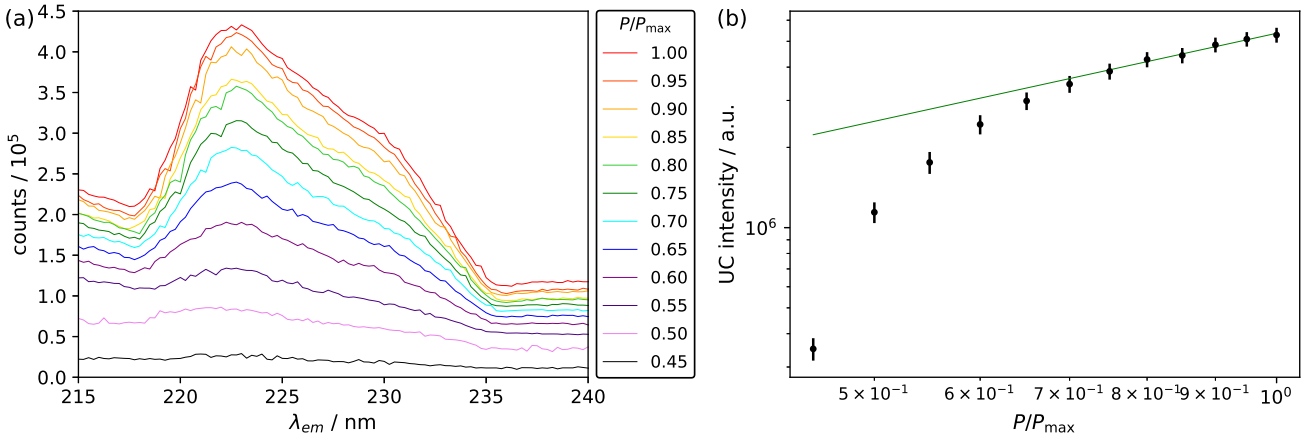

Figure 32: (a) Anti-Stokes upconversion emission spectrum of YPO_4:Pr^{3+} ($\lambda_{ex} = 451$ nm, OPO) between 215 nm and 240 n at various relative excitation powers and (b) UC emission intensity, obtained by numerical integration of the spectra between $\lambda_{em} = 217.75$ nm and $\lambda_{em} = 235.0$ nm, as a function of relative OPO power, with linear regression over relative excitation powers from 0.75 to 1.00 ($\chi_{red}^2 = 1.9 \cdot 10^{-4}$).

4.4.3 Decay analysis

Since the situation regarding the $4f^2$-based energy levels of Pr^{3+} is virtually identical between the $LaBO_3$ and YPO_4 hosts, the same mathematical description presented in equations 8 to 11 for the decay kinetics in $LaBO_3$:Pr^{3+} is valid for YPO_4:Pr^{3+}. Hence, bi-exponential and single-exponential decay behaviour are expected for the $^1D_2$ and $^3P_0$ levels respectively upon $^3H_4 \rightarrow {}^3P_J$ ($J = 0, 2$) excitation, and single exponential decay behaviour is expected for the $^1D_2$ level upon $^3H_4 \rightarrow {}^1D_2$ excitation.

The decay curves upon monitoring the $^3P_0 \rightarrow {}^3H_4$ emission upon excitation into the $^3P_2$ and $^3P_0$ levels are depicted in Figure 33. As in $LaBO_3$, both decay curves display a pronounced bi-exponential decay behaviour, in contradiction to the predicted single exponential decay according to equation 11. Since this bi-exponential behaviour is expected to posses a single component representing the $^3P_0 \rightarrow {}^3H_4$ emission, a bi-exponential function was fitted to the decay curves, represented by the red regression lines in Figure 33. The decay components were found to be (7.05 ± 0.03) μs and (30.6 ± 0.4) μs for 451 nm excitation, and (7.51 ± 0.06) μs and (23.5 ± 0.5) μs for 480 nm excitation.
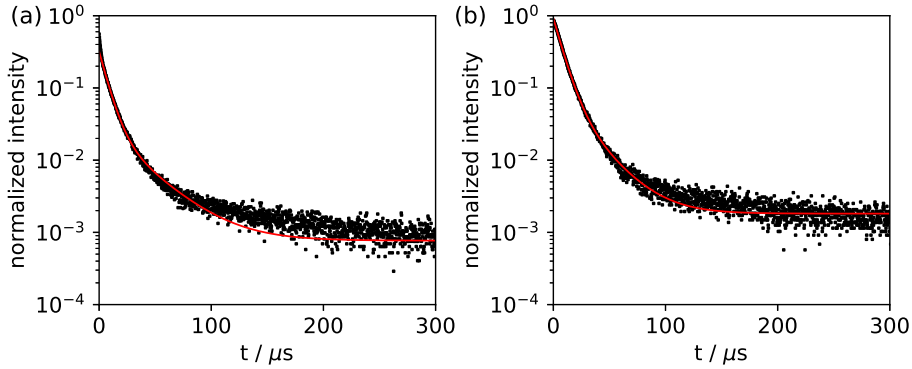

Figure 33: Luminescence decay curves of the Pr^{3+} $^3P_0 \rightarrow {}^3H_4$ emission ($\lambda_{em} = 485$ nm) in the YPO_4 host upon (a) $^3H_4 \rightarrow {}^3P_2$ ($\lambda_{ex} = 451$ nm) and (b) $^3H_4 \rightarrow {}^3P_0$ ($\lambda_{ex} = 480$ nm) excitation.

The decay curves obtained upon monitoring the $^1D_2 \rightarrow {}^3H_4$ emission upon excitation into the $^3P_2$, $^3P_0$ and $^1D_2$ levels are depicted in Figure 34, respectively. Similar to the $LaBO_3$ sample, bi-exponential decay is observed for excitation into the ^3P_J levels, but the rise time predicted by equation 11 is absent. Like $LaBO_3$:Pr^{3+}, the observed bi-exponential decay is possible attributable to the $^3P_0 \rightarrow {}^3H_6$ emission, which possesses a similar energy compared to the $^1D_2 \rightarrow {}^3H_4$ emission. Unlike the decay curves observed in $LaBO_3$:Pr^{3+} however, the decay curves for YPO_4:Pr^{3+} display a significantly longer-lived component as the component with the shortest decay time. Hence, the assumption that this decay component originates from an emission overlapping in energy with the $^1D_2 \rightarrow {}^3H_4$ emission is not reasonable. It does, however, provide an argument for attributing the longer-lived component to the $^1D_2 \rightarrow {}^3H_4$ emission, considering the expected similarity in decay times for the well-shielded $4f^2$-based levels in different hosts and the isolate nature of the $^1D_2$ level. Bi-exponential functions were fitted to the decay curves in Figures 34a and 34b, yielding decay components of (6.61 ± 0.04) μs and (25.5 ± 0.3) μs for 451 nm excitation, and (5.36 ± 0.04) μs and (17.09 ± 0.20) μs for 480 nm excitation. Single-exponential decay behaviour is observed for 580 nm excitation, in agreement with the predictions from equation 11. Fitting a single-exponential function to the decay curve in Figure 34c, a decay time of (9.53 ± 0.14) μs was found.
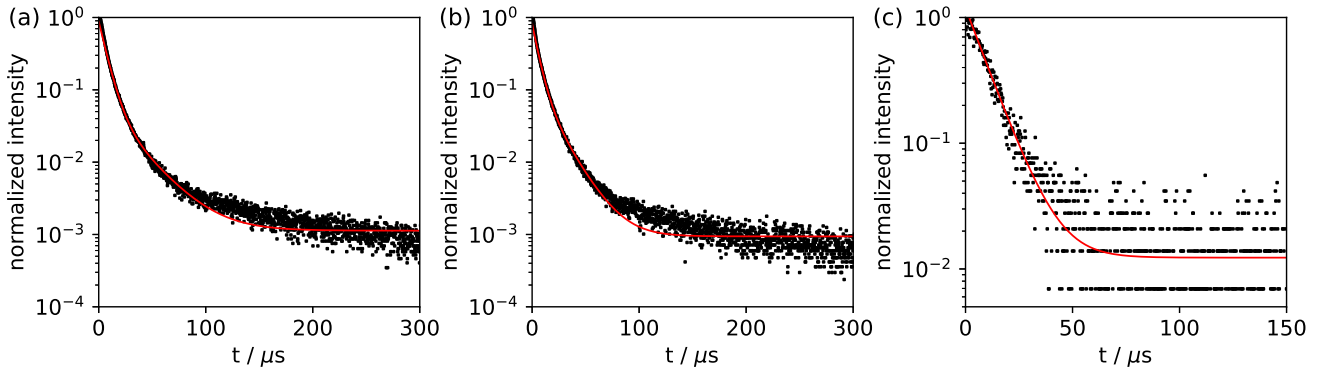
Figure 34: Luminescence decay curves of the Pr^{3+} $^1D_2 \rightarrow {}^3H_4$ emission (λ_{em} = 615 nm) in the YPO_4 host upon (a) $^3H_4 \rightarrow {}^3P_2$ (λ_{ex} = 451 nm), (b) $^3H_4 \rightarrow {}^3P_0$ (λ_{ex} = 480 nm) and (c) $^3H_4 \rightarrow {}^1D_2$ (λ_{ex} = 580 nm) excitation.

In analogy to the $LaBO_3$:Pr^{3+} sample, the shorter-lived component of the bi-exponential decay behaviour observed for the $^3P_0$ level is attributed to the $^3P_0 \rightarrow {}^3H_4$ emission. Hence, reported lifetimes of this emission are (7.05 ± 0.03) μs and (7.51 ± 0.06) μs for 451 nm and 480 nm excitation, respectively. While the difference between these reported decay times is significant, they are of the same order of magnitude as both the previously discussed decay times reported for the $^3P_0$ level in literature and the decay times found for this level in $LaBO_3$:Pr^{3+}. Likewise, the longer-lived decay component of the bi-exponential decay behaviour observed for the $^1D_2$ upon excitation into the ^3P_J levels is attributed to the $^1D_2 \rightarrow {}^3H_4$ emission. Consequently, reported lifetimes for this particular emission are (25.5 ± 0.3) μs, (17.09 ± 0.20) μs and (9.53 ± 0.14) μs for 451 nm, 480 nm and 580 nm excitation, respectively.

The differences between the observed decay times are significant, even more so than for both the decay times reported for $LaBO_3$:Pr^{3+} and the $^3P_0$ level in YPO_4:Pr^{3+}. Despite the different values, the lifetimes found for the $^1D_2 \rightarrow {}^3H_4$ emission upon excitation into the ^3P_J levels do conform with the order of magnitude of the lifetime of this emission reported in literature and in $LaBO_3$:Pr^{3+} within the context of this thesis. The much shorter decay time found upon direct excitation into the $^1D_2$ level, however, does not conform to previously established lifetimes, and also deviates significantly from the shorter-lived decay components found for the $^1D_2$ level upon excitation into the ^3P_J levels. The cause for this was not decisively established, but might be attributable to a deficit in the used equipment. Another possibility may be one related to the sample itself: the reflections in the XRD pattern of the synthesized YPO_4 (see Figure 15) displays somewhat broad reflection peaks. Combined with the drying performed at 150 °C, the possible presence of residual water on the surface and consequent quenching of luminescence is considered. Like in $LaBO_3$:Pr^{3+}, the employed pumping wavelength of 451 nm upon inclusion of a non-radiative relaxation process to the $^1D_2$ level is actually too high to support an efficient ESA to the even higher energetic $4f^15d^1$ levels in YPO_4:Pr^{3+} compared to $LaBO_3$:Pr^{3+}. Thus, it may already be concluded that YPO_4:Pr^{3+} is not a convenient choice for an efficient red-to-UV upconversion material.

4.5 Luminescent features of LuAG:Pr^{3+}

The lowest energy level of the $4f^1d^1$ configuration in LuAG:Pr^{3+} is located at approximately 36,000 cm^{-1} above the $4f^2(^3H_4)$ level, based on its UV excitation maxima reported in literature.[60, 71] This results in LuAG:Pr^{3+} being a potential candidate for a $4f^15d^1 \rightarrow 4f^2(^3H_J)$ UC emission via $4f^2(^3H_4) \rightarrow 4f^2(^3P_2)$ GSA and $4f^2(^1D_2) \rightarrow 4f^15d^1$ ESA. In addition, the highest phonon on energy of approximately 750 cm^{-1} is considerably lower than the highest phonon energy of the LaBO$_3$ and YPO$_4$ hosts.[72] For the LuAG:Pr^{3+} compound, both the intraconfigurational $4f^2 \leftrightarrow 4f^{2'}$ luminescence and the interconfigurational $4f^2 \leftrightarrow 4f^15d^1$ will be briefly characterized. UC emission will be investigated in more detail, as will the decay kinetics of the relevant $4f^2$-based levels.

4.5.1 $4f^2 \leftrightarrow 4f^{2'}$ luminescence

An emission spectrum upon the $^3H_4 \rightarrow {}^3P_2$ (λ_{ex} = 451 nm) excitation of LuAG:Pr^{3+} is depicted in Figure 35. Similar the LaBO$_3$:Pr^{3+} and YPO$_4$:Pr^{3+} samples, the highest-intensity peak is assigned the $^3P_0 \rightarrow {}^3H_4$ emission, with a slightly less intense $^1D_2 \rightarrow {}^3H_4$ emission being observed, by which the $^3P_0$ and $^1D_2$ levels are populated through multi-phonon relaxation from the $^3P_2$ levels. The high intensity of the $^1D_2 \rightarrow {}^3H_4$ is somewhat unexpected, as the maximum phonon energy in LuAG ($\hbar\omega \approx 750$ cm^{-1}) compared to the LaBO$_3$ and YPO$_4$ hosts would lead to the prediction that the $^3P_2 \rightarrow {}^1D_2$ multi-phonon relaxation is less efficient, decreasing the population of the $^1D_2$ level. While unexpected, the relatively high intensity of this emission is promising in the light of the upconversion process, as, apparently, the $^1D_2$ level is efficiently populated, leading to the possibility of performing ESA from this level. In addition to these two well-understood emission peaks, several lower-intensity peaks absent in the emission spectra for the other two Pr^{3+}-activated compounds are observed, a cause for which is not known. In addition, an emission spectrum upon the $^3H_5 \rightarrow {}^1D_2$ (λ_{ex} = 580 nm) excitation is depicted in Figure 36. In this spectrum, the same emission peaks with low signal-to-noise ratio attributed to inefficient transitions as observed and discussed for the other two Pr^{3+}-activated compounds.
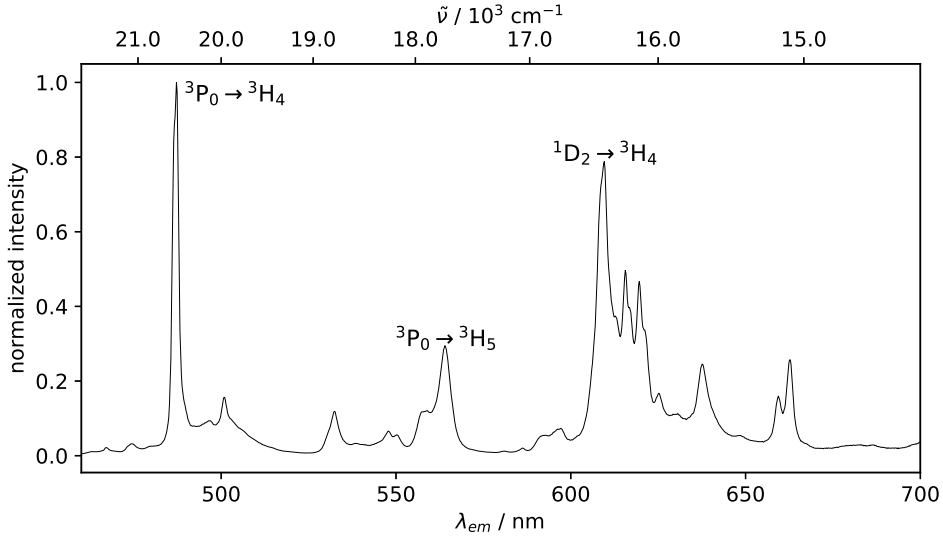

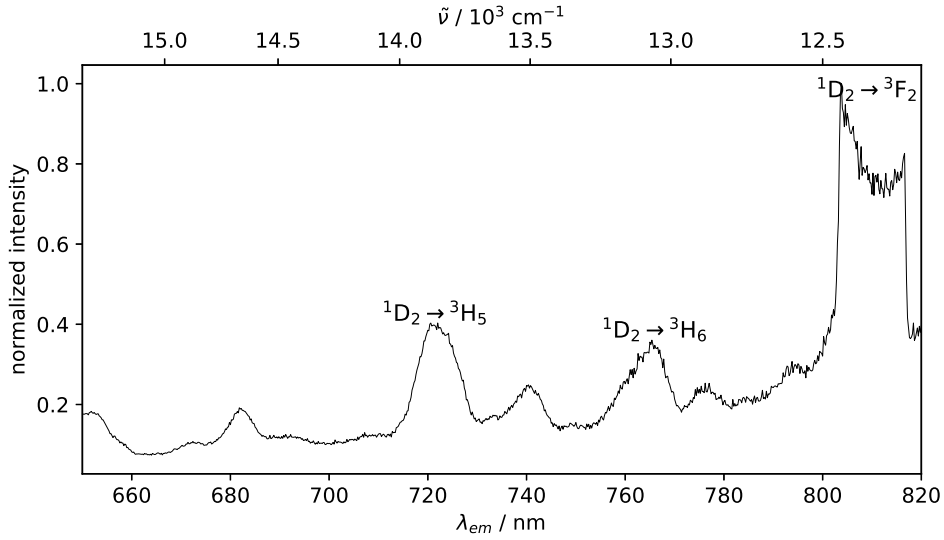Figure 35: Emission spectrum (λ_{ex} = 451 nm) for LuAG:Pr^{3+}

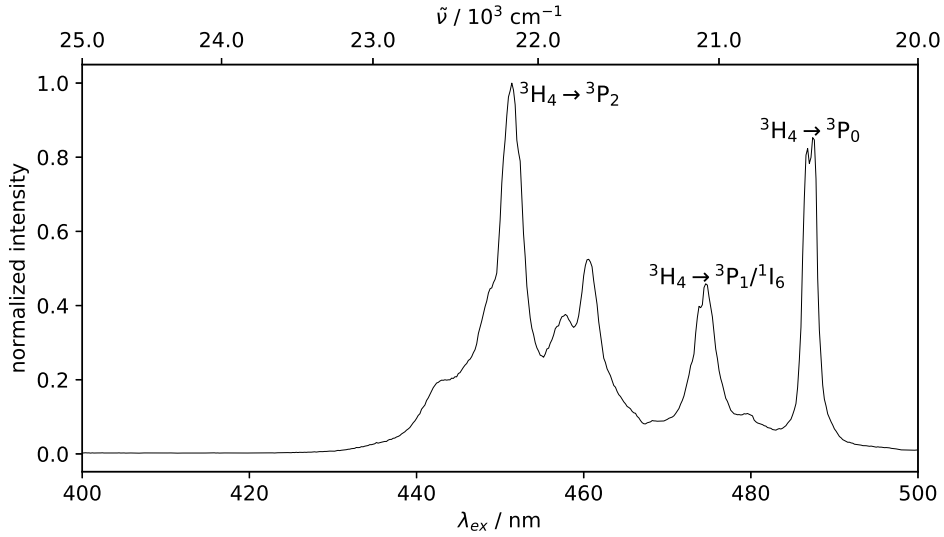Figure 36: Emission spectrum ($\lambda_{\text{ex}} = 580$ nm) for LuAG:Pr^{3+}

Figure 37: Excitation spectrum ($\lambda_{\text{em}} = 609$ nm) for LuAG:Pr^{3+}

In addition to the previously presented emission spectra, an excitation spectrum upon monitoring the $^1D_2 \rightarrow {}^3H_4$ emission ($\lambda_{\text{ex}} = 609$ nm) is depicted in Figure 37. The same three excitation peaks observed in the excitation spectra for the other two Pr^{3+}-activated compounds are present, again conforming the similarity. As for the other Pr^{3+}-activated compounds, resolving of the $^3P_1$ and $^1I_6$ levels at room temperature is impossible due to Stark splitting of these levels. A fourth excitation peak centered around $\lambda_J = 460$ nm is observed. Since its position does not fit to an excitation originating from the $4f^2(^3H_4)$ level even when considering Stark splitting, this is likely an artifact. The high intensity of the emission upon $^3H_4 \rightarrow {}^3P_2$ excitation is again in agreement with the high line strength for the $^3H_4 \rightarrow {}^3P_2$ absorption. It was therefore decided to investigate the UC process primarily upon 451 nm excitation of the LuAG:Pr^{3+} compound.

4.5.2 $4f^2 \leftrightarrow 4f^15d^1$ luminescence

Since the lowest levels of the $4f^15d^1$ configuration are considerably lower in energy in LuAG:Pr^{3+} compared to both LaBO$_3$:Pr^3 and YPO$_4$:Pr^{3+}, the spectroscopic equipment employed within this thesis was suitable for studying luminescence upon direct $4f^2(^3H_4) \to 4f^15d^1$ excitation LuAG:Pr^{3+}. That circumstance allowed for an examination of the position of the emission and excitation bands, and for a meaningful comparison with the position of this band reported in literature. An excitation spectrum in the UV range upon detection of the $4f^2(^1D_2) \to {}^3H_4$ emission ($\lambda_{em} = 615$ nm) is displayed in Figure 38. Two broad excitation bands characteristic for the $4f^2(^3H_4) \to 4f^15d^1$ transition are observed, centered at around 245 nm and 280 nm in accordance with the positions reported in literature.[60,71] The energy of the latter confirms the possibility of $^1D_2 \to 4f^15d^1$ ESA using 451 nm excitation (the wavelength used for the $4f^2(^3H_4) \to 4f^2(^3P_2)$ GSA) to achieve the desired $4f^15d^1 \to 4f^2(^3H_J)$ UC emission. In addition, an emission spectrum upon direct 245 nm excitation into the $4f^15d^1$ configuration for LuAG:Pr^{3+} is depicted in Figure 38. Two broad emission bands characteristic for $4f^15d^1 \to 4f^2$ emission centered around 311 nm and 373 nm are observed in accordance with the positions of these emission bands reported in literature.[60,71]
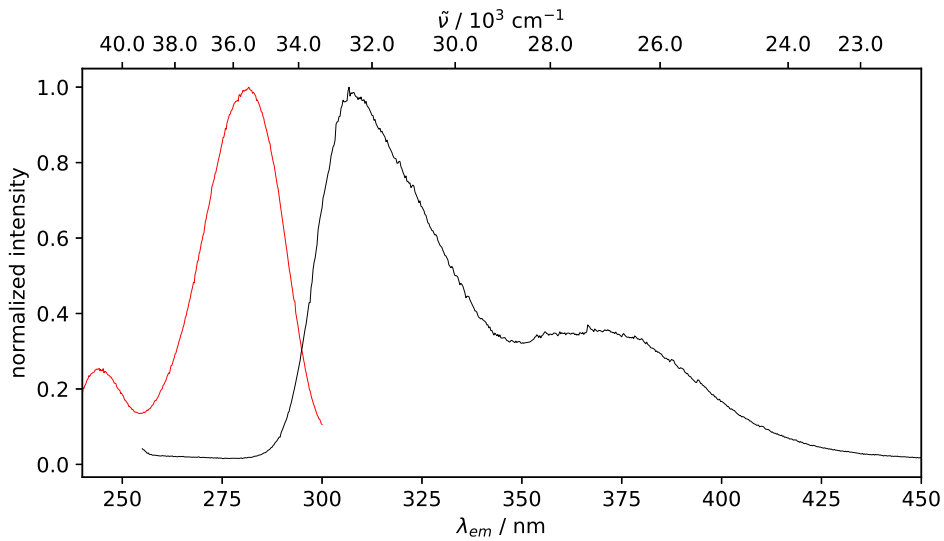

Figure 38: Excitation spectrum ($\lambda_{em} = 615$ nm, in red)and emission spectrum ($\lambda_{ex} = 245$ nm, in black) of LuAG:Pr^{3+}

4.5.3 Upconversion luminescence

The anti-Stokes emission spectra upon 451 nm excitation with the OPO for relative excitation powers from 0.60 to 1.00 are displayed in Figure 39. Two broad UC emission peaks are observed, corresponding to the $4f^15d^1 \rightarrow 4f^2(^3H_4)$ and $4f^15d^1 \rightarrow 4f^2(^3H_5)$ emissions, respectively, which are observed upon direct GSA into the $4f^15d^1$ configuration. Additionally, the signal-to-noise ratio observed for these emission peaks is very small, even more than is the case for the UC emission in the other Pr^{3+}-activated compounds investigated within this thesis. A possible explanation for this low intensity may be inherent to the proposed UC upconversion mechanism: the energy of the $4f^15d^1$-related UC emission in LuAG:Pr^{3+} necessitates a multi-phonon relaxation from the $^3P_0$ level to the $^1D_2$ level, which are separated by approximately 3500 cm^{-1}.[52] Considering the highest phonon energy in the LuAG host is approximately 750 cm^{-1},[72] more than 4 phonons are required to bridge this gap. This circumstance makes the corresponding non-radiative transition from the $^1D_2$ less probable and as such may hamper the UC process. In addition, the excitation source pulse width of 10 ns is to be considered in combination with the repetition rate. As for the two other Pr^{3+}-activated compounds investigated within this thesis, the level from which the ESA presumably takes place, does not posses appreciable population 50 ms after the excitation pulse due to the reported decay times of this level all being lower than 100 μs. Hence, GSA and ESA are to occur within a single 10 ns excitation pulse, potentially hampering the UC emission intensity. In addition, the $^3P_0 \rightarrow {}^1D_2$ multi-phonon relaxation necessary to facilitate the $4f^2(^1D_2) \rightarrow 4f^15d^1$ ESA also must occur within this narrow excitation pulse, potentially further hampering the UC emission intensity.

The relation between the UC emission intensity and the relative excitation power for both emission peaks in Figure 39 are depicted in Figure 40. Unlike the two previously presented compounds, a clear distinction between two regions with a different order dependence between them is observed for both of these peaks. Linear regression on the logarithm of the UC emission intensity of the peak centered around 310 nm, obtained by numerical integration from $\lambda_{em} = 288$ nm to $\lambda_{em} = 344$ nm as a function of the logarithm of the relative laser power (see Figure 40a), yields a slope of 2.48 ± 0.30 for relative excitation powers from 0.65 to 0.80, and a slope of 1.45 ± 0.08 for relative excitation powers from 0.80 to 1.00. The two-slope character agrees with the dependency of the UC emission intensity on the expected decrease of the UC emission intensity for higher pump powers due to the more efficient $4f^2 \rightarrow 4f^15d^1$ ESA compared to the $4f^2 \rightarrow 4f^{2'}$ GSA process. However, the slopes for this particular UC emission band found within the context of this thesis deviate significantly from the theoretical slopes of 2.00 and 1.00 for the low- and high-power limits respectively.[62] This may be readily explained by the extremely low signal-to-noise ratio observed in the UC emission spectrum, resulting in a large, yet unquantifiable error in the UC intensity.

Linear regression on the logarithm of the UC emission intensity of the peak centered around 380 nm, obtained by numerical integration from $\lambda_{em} = 344$ nm to $\lambda_{em} = 409$ nm as a function of the logarithm of the relative laser power (see Figure 40b) yields a slope of 2.29 ± 0.29 for relative excitation powers from 0.65 to 0.80, and a slope of 1.12 ± 0.09 for relative excitation powers from 0.80 to 1.00. Within the error margins, this conforms very well with the expected quadratic dependence of the UC emission intensity as a function of excitation power based on the fact that the GSA/ESA process is a two-photon process. At higher excitation powers, the dependency becomes linear due to the greater efficiency of the ESA compared to the GSA.[9,62] This aspect additionally confirms the influence of the non-systematic error resulting from the low signal-to-noise ratio, as the two UC emission bands are expected to display the same power dependence behaviour.
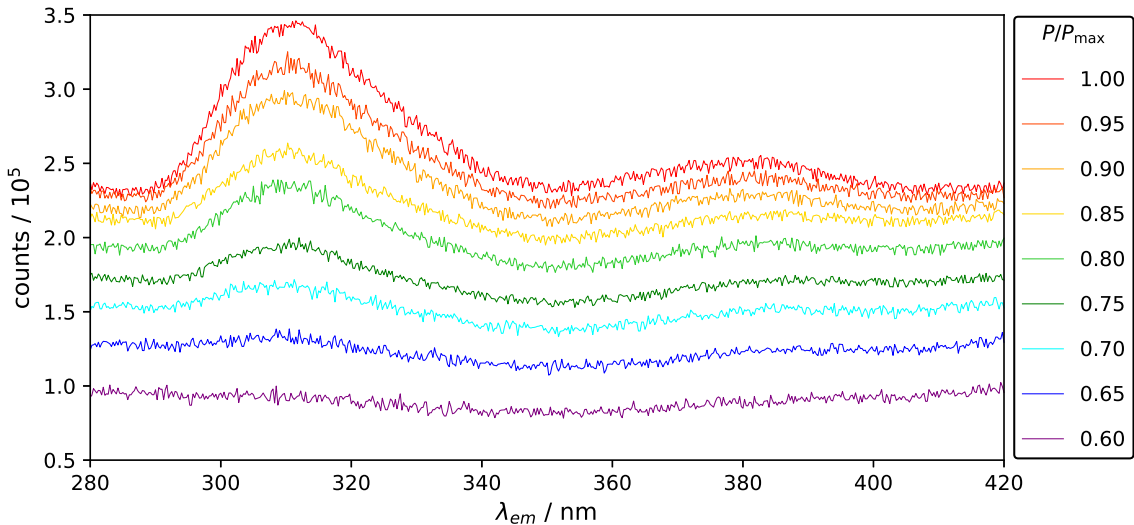

Figure 39: Anti-Stokes upconversion emission of LuAG:Pr^{3+} ($\lambda_{ex} = 451$ nm, OPO) from 280 nm to 430 nm at various relative excitation powers
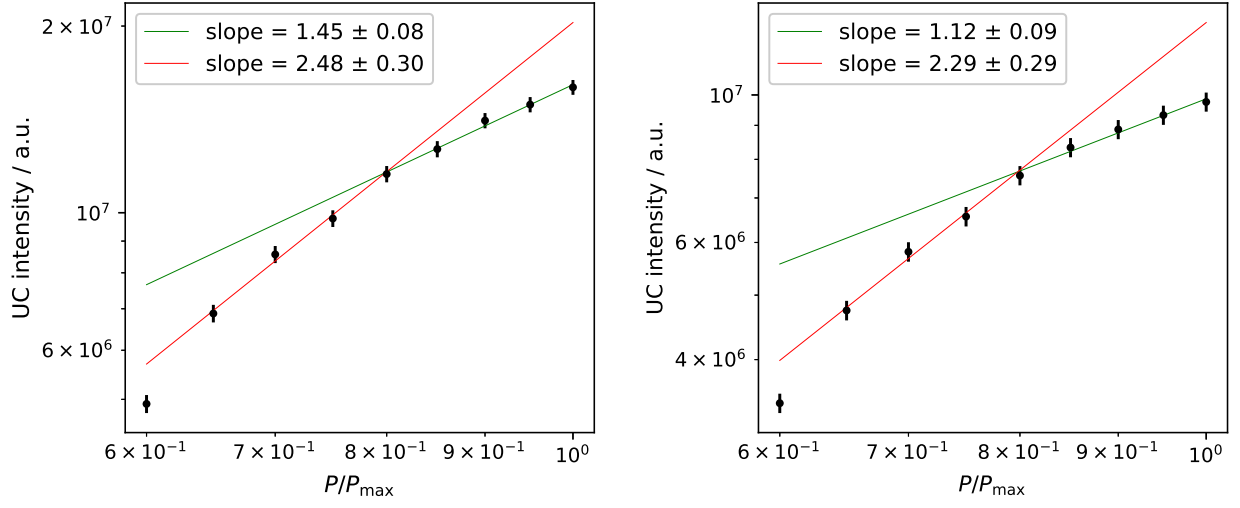
Figure 40: UC emission intensity in LuAG:Pr^{3+} upon 451 nm OPO excitation for (a) the emission band centered around 310 nm, obtained by numerical integration of the emission spectra from $\lambda_{em} = 288$ nm and $\lambda_{em} = 344$ nm with regression lines for excitation powers from 0.65 to 0.80 (in red, $\chi^2_{red} = 7.3 \cdot 10^{-5}$) and 0.80 to 1.00 (in green, $\chi^2_{red} = 7.3 \cdot 10^{-5}$), and (b) the emission band centered around 380 nm, obtained by numerical integration of the emission spectra from $\lambda_{em} = 344$ nm and $\lambda_{em} = 409$ nm, as a function of relative laser power with regression lines for excitation powers from 0.65 to 0.80 (in red, $\chi^2_{red} = 1.4 \cdot 10^{-4}$) and 0.80 to 1.00 (in green, $\chi^2_{red} = 7.6 \cdot 10^{-5}$).

4.5.4 Decay analysis

Since the situation regrading the $4f^2$-based levels in LuAG:Pr^{3+} is virtually identical to that in the the $LaBO_3$:Pr^{3+} and YPO$_4$:Pr^{3+}, the same mathematical description of the decay kinetics (see equations 8 to 11) applies, which predicts bi-exponential and single-exponential decay of the $^1D_2$ and $^3P_0$ levels, respectively upon $^3H_4 \rightarrow {}^3P_J$ ($J = 0, 2$) excitation. In addition, the $^1D_2$ level is expected to display a single exponential decay upon monitoring the $^1D_2 \rightarrow {}^3H_4$ emission.

The decay curves obtained by monitoring the $^3P_0 \rightarrow {}^3H_4$ emission upon excitation into the $^3P_2$ and $^3P_0$ are depicted in Figure 41. Similar to the $^3P_0$ level in $LaBO_3$:Pr^{3+} and YPO$_4$:Pr^{3+}, bi-expontential decay is observed, again contradicting the predictions based on equation 11. Cross relaxation may be a possible reason here due to the higher Pr^{3+} doping concentration of 1% in this compound. A bi-exponential function, expected to exhibit a single-exponential component representing the $^3P_0 \rightarrow {}^3H_4$ emission timescale, was fitted to both decay curves. The decay components were found to be (10.86 ± 0.05) μs and (25.2 ± 0.8) μs for 451 nm excitation, and (8.41 ± 0.08) μs and (15.3 ± 0.03) μs for 480 nm excitation.

The decay curves upon monitoring the $^1D_2 \rightarrow {}^3G_4$ emission upon excitation into the $^3P_2$, $^3P_0$ and $^1D_2$ levels are depicted in Figure 42. For excitation into the ^3P_J levels, bi-exponential decay is observed. However, as for the other two two compounds investigated, the rise time predicted by the results in equation 11 are absent, possibly attributable to the aforementioned overlap in energy with the $^3P_0 \rightarrow {}^3H_6$ emission. However, unlike the other Pr^{3+}-doped compounds, the $^1D_2$ level in the investigated LuAG:Pr^{3+} sample also displays bi-exponential decay upon excitation into the same level. Since this decay cannot be explained by the overlapping energy of the $^3P_0 \rightarrow {}^3H_6$ emission, this behaviour is attributed to cross-relaxation related to the higher Pr^{3+} doping concentration of 1 mol%, compared to the 0.5 mol% in the other two Pr^{3+}-activated compounds. Hence, bi-exponential functions were fitted to the three $^1D_2$ decay curves, represented by the red regression lines in Figure 42. The decay components were found to be 10.005 ± 0.010 μs and 68.4 ± 0.6 μs for 451 nm excitation, 9.049 ± 0.019 μs and 56.6 ± 0.6 μs for 480 nm excitation, and 10.94 ± 0.16 μs and 71.7 ± 0.6 μs for 580 nm excitation. In addition, a single-exponential function was fitted to the $^1D_2$ decay curve upon 580 nm excitation over the data interval where the decay displayed single-exponential character, as is represented by the green regression line in Figure 42c. The decay time in this regression was found to be (64.6 ± 0.6) μs.
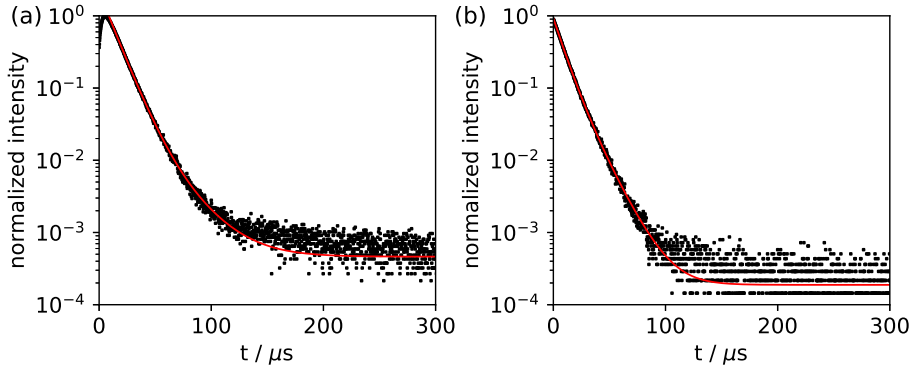

Figure 41: Luminescence decay curves of the Pr^{3+} $^3P_0 \rightarrow {}^3H_4$ emission ($\lambda_{em} = 485$ nm) in the LuAG host upon (a) $^3H_4 \rightarrow {}^3P_2$ ($\lambda_{ex} = 451$ nm) and (b) $^3H_4 \rightarrow {}^3P_0$ ($\lambda_{ex} = 480$ nm) excitation.
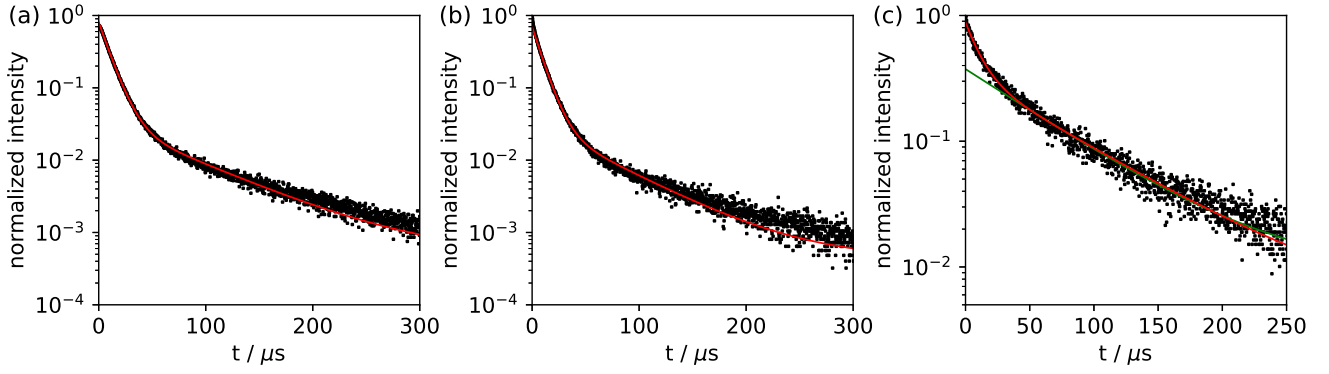
Figure 42: Luminescence decay curves of the Pr^{3+} $^1D_2 \rightarrow {}^3H_4$ emission ($\lambda_{em} = 615$ nm) in the LuAG host upon (a) $^3H_4 \rightarrow {}^3P_2$ ($\lambda_{ex} = 451$ nm), (b) $^3H_4 \rightarrow {}^3P_0$ ($\lambda_{ex} = 480$ nm) and (c) $^3H_4 \rightarrow {}^1D_2$ ($\lambda_{ex} = 580$ nm) excitation.

Considering the spin-allowed character of the $^3P_0 \rightarrow {}^3H_4$ emission for the lighter Pr^{3+} ions and the spin-forbidden character of the $^1D_2 \rightarrow {}^3H_4$ emission,[67,68] the shorter-lived component of the bi-exponential decay behaviour observed for the $^3P_0$ level is attributed to the $^3P_0 \rightarrow {}^3H_4$ emission. Hence, reported lifetimes for this particular emission the LuAG:Pr^{3+}:Pr^{3+} are (10.85 ± 0.05) μs upon 451 nm excitation and (8.41 ± 0.08) μs upon 480 nm excitation. Likewise, the longer-lived component of the bi-exponential decay behaviour observed for the $^1D_2$ level is attributed to the $^1D_2 \rightarrow {}^3H_4$ emission. Hence, the reported lifetimes of this emission are (68.4 ± 0.6) μs, (56.6 ± 0.6) μs and (71.7 ± 0.6) μs for 451 nm, 480 nm and 580 nm excitation respectively. The lifetime of (64.6 ± 0.6) μs for 580 nm excitation obtained from the single-exponential fit is similar to these decay components, and is hence also attributed to the $^1D_2 \rightarrow {}^3H_4$ emission.

As observed for the other Pr^{3+}-doped compounds, the emission lifetimes of both the $^3P_0 \rightarrow {}^3H_4$ emission and $^1D_2 \rightarrow {}^3H_4$ emission significantly differ based on the excitation wavelengths. The agreement in the orders of magnitudes confirms that the $^3H_4 \rightarrow {}^3P_2$ GSA and $^1D_2$ ESA occur within a single excitation pulse. In addition, it indicates that the UC emission may best be achieved via ESA from the $^1D_2$ due to the longer decay time of that energy level. The lifetimes of intraconfigurational emission between the $4f^2$-based levels reported both within the context of this thesis and in literature are several order of magnitude higher than the $4f^1 5d^1 \rightarrow 4f^2$ emission lifetime of 17 ns,[60,73] again explained by the parity-allowed character of this emission.

5 Conclusions and Perspectives

The SrB_4O_7 host lattice was successfully synthesized. However, the reduction of Tm^{3+} to Tm^{2+} within this host compound was unsuccessful. It was proposed that this possibly resulted from an inadequacy of the used lab equipment such as an unstable furnace temperature or insufficient insulation. Since the $4f^{13}$-based energy levels in Tm^{2+} combined with the position of the lowest level in the $4f^{12}5d^1$ configuration theoretically allow for UC emission, optimization of this synthesis may be considered for future research. A new vacuum oven within the research group, having become available at the end of this thesis, could be potentially useful in achieving a well-insulated environment with homogeneous temperature distribution, which may prove useful in achieving the desired reduction of Tm^{3+} to Tm^{2+}.

The reduction of Sm^{3+} to Sm^{2+} in the SrB_4O_7 host was successful. However, the $4f^55d^1 \rightarrow 4f^6(^7F_J)$ UC emission of Sm^{2+} within this host was hampered by a combination of a too high phonon energy and the low energy of the $4f^55d^1$ configuration. Hence, the SrB_4O_7 host was proven to be unsuitable for achieving upconversion in Sm^{2+}. To successfully achieve the desired UC emission, the SrFCl host was proposed as a promising alternative, as the strong ionicity of fluoride ions result in a higher-energetic $4f^55d^1$ configuration, and the chloride ions result in a lower maximum phonon energy due to their higher mass. This SrFCl host lattice was successfully synthesized. However, the reduction of Sm^{3+} to Sm^{2+} in this host was unsuccessful, possibly caused by an insufficient insulation of the reaction. Considering the potential of this sample, repeating the synthesis with better-insulated equipment, e.g. in the newly installed vacuum oven, should be considered for future studies. If the synthesis SrFCl and the reduction of Sm^{3+} to Sm^{2+} both prove successful, the UC process upon 684 nm excitation may be investigated, allowing for a meaningful comparison with the UC process in Pr^{3+}.

The synthesis of both $LaBO_3$:Pr^{3+} via solid-state synthesis and YPO_4:Pr^{3+} via precipitation from solution with a doping concentration of 0.5 mol% were successful. Together with the previously available LuAG:Pr^{3+} sample with a doping concentration of 1 mol%, these were studied in terms of their luminescent properties. Xe lamp excited intraconfigurational $4f^2 \leftrightarrow 4f^{2\prime}$ luminescence confirmed the high line strength for the $^3H_4 \leftrightarrow {}^3P_2$ transition as predicted by Judd-Ofelt analysis. Hence, the excitation wavelength for the GSA in the UC process was established at 451 nm, corresponding to the $^3H_4 \rightarrow {}^3P_2$ excitation. With an OPO excitation of this particular excitation wavelength, a UC emission signal was observed for all three Pr^{3+} samples. In $LaBO_3$:Pr^{3+} and YPO_4:Pr^{3+}, an additional emission band of unknown origin centered around $\lambda_{em} = 224$ nm was observed, significantly overlapping with the UC emission in YPO_4:Pr^{3+}.

The expected linear dependency of the UC emission intensity on the relative excitation pump power in the high-power limit due to saturation was observed in both $LaBO_3$:Pr^{3+} and YPO_4:Pr^{3+}, in agreement with the prediction that the ESA process involving the $4f^15d^1$ configuration is more efficient than the $4f^2 \rightarrow 4f^{2\prime}$ GSA process upon consideration of the respective parity-allowed and parity-forbidden natures of these transitions. However, the expected quadratic dependency for the lower excitation powers was not observed. Instead, the order of dependency gradually increases for lower laser powers. This phenomenon is possibly attributable to the narrow 10 ns excitation pulse width together with the repetition rate of 20 Hz, by which the UC process may be additionally hampered. $^3P_0$ decay times in the order of 1-10 μs reported in literature suggest that the $^3H_4 \rightarrow {}^3P_2$ GSA and $^3P_0 \rightarrow 4f^15d^1$ ESA must occur within a single excitation pulse, as there is no appreciable population of the $^3P_0$ level 50 ms after the excitation This was confirmed by the decay times found for the $^3P_0$ level, which were between 5 and 8 μs. Hence, the UC process may be additionally hampered by this narrow pulse width, as 10 ns may be too short to achieve an appreciable ^3P_J population for lower excitation powers.

The UC emission intensity of the two emission peaks in LuAG:Pr^{3+} as a function of relative excitation power, however, do display a distinct two-slope character on a double-logarithmic scale. The slopes of 1.45 ± 0.08 and 2.48 ± 0.30 for the higher and lower excitation powers, respectively, observed for the emission peak centered around $\lambda_{em} = 311$ nm deviate significantly from the predicted 1.00 and 2.00, explained by the large unquantifiable error introduced by the exceptionally low signal-to-noise ration. The power dependence of the UC emission peak centered around $\lambda_{em} = 380$ nm, however, agrees with the expected slopes within the error margins. Decay times for the $^1D_2$ level reported in literature are in the order of 10-100 μs for a variety of host lattices. The decay times for the $^1D_2$ level in LuAG:Pr^{3+} found within the context of this thesis vary from 56.6 to 71.7 μs and thus agree well with the reported lifetimes of this level. Based on those lifetimes, it was proposed that the $4f^2(^3H_4) \rightarrow 4f^2(^3P_2)$ GSA and $4f^2(^1D_2) \rightarrow 4f^15d^1$ ESA occur within the same excitation pulse. Hence, since multi-phonon relaxation from the $^3P_0$ to $^1D_2$ level is supposed to occur within this excitation pulse as well, the UC process may be hampered by the narrow pulse width, even more so than for Pr^{3+}-doped $LaBO_3$ and YPO_4.

The decay times reported for the $^3P_0$ and $^1D_2$ levels in all three Pr^{3+}-doped host lattices suggest achieving the UC emission though ESA from the $^1D_2$ is more efficient. Hence, the ideal material for pulsed excitation upconversion would possess a $4f^15d^1$ configuration with an absorption band maximum with an energy of 39,000 cm^{-1} ($\lambda_{ex} = 256$ nm) to facilitate an ideal $^1D_2 \rightarrow 4f^15d^1$ ESA after pumping with a wavelength of around 445 nm to efficiently excite Pr^{3+} into the $^3P^2$ level. Additionally, this ideal host should exhibit a higher maximum phonon energy than

LuAG ($\hbar\omega = 750$ cm^{-1}), such that the energy gap between the $^3P_0$ and $^1D_2$ may be more effectively bridged by the multi-phonon relaxation, and allows for a more appreciable population of the $^1D_2$ level between excitation pulses. The magnitude of this maximum phonon energy, however, does have an upper limit, as extremely high phonon energies can result in efficient multi-phonon relaxation from the $^1D_2$ to the $^1G_4$ level and hamper the UC process. Consequently, an ideal phonon energy would be approximately 1500 cm^{-1}. Additionally, this ideal host lattice would feature a high-valued Ω_6 for the intraconfigurational $^3H_4 \leftrightarrow {}^3P_2$ 4f^2 transition as to achieve the highest possible line strength for the $^3H_4 \rightarrow {}^3P_2$ GSA process.

For future research, the upconversion process in Pr^{3+} may also be investigated upon continuous wave laser excitation. At the final stage of this thesis, a 450 nm continuous wave diode laser arrived, which would be ideal to study the UC via the 4f^2($^3H_4$) $\rightarrow$ 4f^2($^3P_2$) GSA. Studying the UC efficiency for this continuous wave laser excitation should be promising, as the UC is not hampered by the excitation pulse width in that case. A second aspect that should be verified, is a comparison of the power dependence of a continuous wave excitation with the power dependence obtained for a pulsed excitation to elucidate the expected quadratic UC emission intensity dependence on the pump power in the low-power regime. The requirements for an ideal host lattice for continuous wave laser excited UC emission via the $^1D_2 \rightarrow$ 4f^{1}5d^1 ESA are identical to the ones proposed for UC emission via pulsed excitation. In addition, a host lattice optimized for achieving the UC emission via the $^3P_0 \rightarrow$ 4f^{1}5d^1 ESA may be investigated under continuous excitation, and compared to the UC emission in compounds relying on achieving UC emission via the 4f^2($^1D_2$) $\rightarrow$ 4f^{1}5d^1. Requirements for this host lattice include a 4f^{1}5d^1 excitation maximum with an energy of 42,500 cm^{-1} ($\lambda_{ex} = 236$ nm) and the lowest possible maximum phonon energy to decrease the efficiency of the $^3P_0 \rightarrow {}^1D_2$ multi-phonon relaxation.

Acknowlegdements

First and foremost, I would like to thank my daily supervisor Markus. Your explanation of theoretical concepts, discussions on the acquired results and their interpretation, and suggestions for optimizing measurements and documentation of the results were invaluable. All in all, I learned a lot from you during the past months working on this thesis, which I thoroughly enjoyed, not least thanks to you.

Secondly, I would like to express my gratitude towards Andries. Thank you for providing me with the opportunity to work on this project within the CMI group, and for the suggestions helped tremendously when I got stuck in the interpretation of the acquired results and how to proceed. In addition, I would like to thank my second corrector Sanli. While the contact was more sporadic, your supervision made this thesis possible, and suggestions and questions both from you and the audience of the BONZ symposium I was able to participate in thanks to your efforts and undoubtedly improved my understanding of my results and this thesis as a whole.

Finally, I would like to thank the CMI research group. In particular, many thanks to Naud, Annelies and Atul for helping me (and sometimes also Markus) in setting up and understanding the lab equipment necessary to bring this project to a successful conclusion, and to the other students in the bachelor room, as the interactions with you made working in on this thesis so much more enjoyable.

References

[1] B. C. Hwang, S. Jiang, T. Luo, J. Watson, G. Sorbello, and N. Peyghambarian, "Cooperative upconversion and energy transfer of new high Er^{3+}- and Yb^{3+}–Er^{3+}-doped phosphate glasses," *Journal of the Optical Society of America B*, vol. 17, p. 833, may 2000.

[2] F. Vetrone, J. C. Boyer, J. A. Capobianco, A. Speghini, and M. Bettinelli, "Significance of Yb^{3+} concentration on the upconversion mechanisms in codoped Y_2O_3:Er^{3+}, Yb^{3+} nanocrystals," *Journal of Applied Physics*, vol. 96, pp. 661–667, jul 2004.

[3] C. Hu, C. Sun, J. Li, Z. Li, H. Zhang, and Z. Jiang, "Visible-to-ultraviolet upconversion in Pr^{3+}:Y_2SiO_5 crystals," *Chemical Physics*, vol. 325, pp. 563–566, jun 2006.

[4] R. Naccache, F. Vetrone, A. Speghini, M. Bettinelli, and J. A. Capobianco, "Cross-relaxation and upconversion processes in Pr^{3+} singly doped and Pr^{3+}/Yb^{3+} codoped nanocrystalline $Gd_3Ga_5O_{12}$: The sensitizer/activator relationship," *The Journal of Physical Chemistry C*, vol. 112, pp. 7750–7756, apr 2008.

[5] M. Kaczkan, D. Pawlak, S. Turczynski, and M. Malinowski, "Site-selective energy upconversion in Pr^{3+}:$Y_4Al_2O_9$," *Journal of Alloys and Compounds*, vol. 728, pp. 1009–1015, dec 2017.

[6] E. L. Cates and J. H. Kim, "Upconversion under polychromatic excitation: Y_2SiO_5:Pr^{3+}, Li^+ converts violet, cyan, green, and yellow light into UVC," *Optical Materials*, vol. 35, pp. 2347–2351, oct 2013.

[7] S. L. Cates, E. L. Cates, M. Cho, and J. H. Kim, "Synthesis and characterization of visible-to-UVC upconversion antimicrobial ceramics," *Environmental Science & Technology*, p. 140205070115003, feb 2014.

[8] E. L. Cates, A. P. Wilkinson, and J. H. Kim, "Visible-to-UVC upconversion efficiency and mechanisms of $Lu_7O_6F_9$:Pr^{3+} and Y_2SiO_5:Pr^{3+} ceramics," *Journal of Luminescence*, vol. 160, pp. 202–209, apr 2015.

[9] E. L. Cates and F. Li, "Balancing intermediate state decay rates for efficient Pr^{3+} visible-to-UVC upconversion: the case of β-$Y_2Si_2O_7$:Pr^{3+}," *RSC Advances*, vol. 6, no. 27, pp. 22791–22796, 2016.

[10] B. Herden, A. Meijerink, F. T. Rabouw, M. Haase, and T. Jüstel, "On the efficient luminescence of β-$Na(La_{1-x}Pr_x)F_4$," *Journal of Luminescence*, vol. 146, pp. 302–306, feb 2014.

[11] B. Herden, A. García-Fuente, H. Ramanantoanina, T. Jüstel, C. Daul, and W. Urland, "Photon cascade emission in Pr^{3+} doped fluorides with CaF_2 structure: Application of a model for its prediction," *Chemical Physics Letters*, vol. 620, pp. 29–34, jan 2015.

[12] R. T. Wegh, H. Donker, K. D. Oskam, and A. Meijerink, "Visible quantum cutting in $LiGdF_4$:Eu^{3+} through downconversion," *Science*, vol. 283, pp. 663–666, jan 1999.

[13] Q. Y. Zhang, G. F. Yang, and Z. H. Jiang, "Cooperative downconversion in $GdAl_3(BO_3)_4$:RE^{3+}, Yb^{3+} (RE=Pr, Tb, and Tm)," *Applied Physics Letters*, vol. 91, p. 051903, jul 2007.

[14] W. Schipper, A. Meijerink, and G. Blasse, "The luminescence of Tm^{2+} in strontium tetraborate," *Journal of Luminescence*, vol. 62, pp. 55–59, sep 1994.

[15] O. S. Wenger, C. Wickleder, K. W. Krämer, and H. U. Güdel, "Upconversion in a divalent rare earth ion: optical absorption and luminescence spectroscopy of Tm^{2+} doped $SrCl_2$," *Journal of Luminescence*, vol. 94-95, pp. 101–105, dec 2001.

[16] J. Grimm, E. Beurer, P. Gerner, and H. Güdel, "Upconversion between 4f–5d excited states in Tm^{2+}-doped $CsCaCl_3$, $CsCaBr_3$, and $CsCaI_3$," *Chemistry - A European Journal*, vol. 13, pp. 1152–1157, jan 2007.

[17] F. Auzel, "Upconversion and anti-stokes processes with f and d ions in solids," *Chemical Reviews*, vol. 104, pp. 139–174, jan 2004.

[18] M. Suta and C. Wickleder, "Synthesis, spectroscopic properties and applications of divalent lanthanides apart from Eu^{2+}," *Journal of Luminescence*, vol. 210, pp. 210–238, jun 2019.

[19] P. Pal, T. Penhouët, V. D'Anna, and H. Hagemann, "Effect of pressure on the free ion and crystal field parameters of Sm^{2+} in BaFBr and SrFBr hosts," *Journal of Luminescence*, vol. 134, pp. 678–685, feb 2013.

[20] P. Pal, H. Hagemann, H. Bill, and J. Zhang, "Temperature and host dependence of the transition interference between f–f and f–d transitions of Sm^{2+} in matlockites," *Journal of Luminescence*, vol. 161, pp. 323–329, may 2015.

[21] S. Sakirzanovas, A. Katelnikovas, D. Dutczak, A. Kareiva, and T. Jüstel, "Concentration influence on temperature-dependent luminescence properties of samarium substituted strontium tetraborate," *Journal of Luminescence*, vol. 132, pp. 141–146, jan 2012.

[22] Y. R. Shen and W. B. Holzapfel, "Effect of pressure on energy levels of Sm^{2+} in BaFCl and SrFCl," *Physical Review B*, vol. 51, pp. 15752–15762, jun 1995.

[23] Y. Shen and K. L. Bray, "Effect of pressure and temperature on 4f-4f luminescence properties of Sm^{2+} ions in MFCl crystals (M=Ba, Sr, and Ca)," *Physical Review B*, vol. 58, pp. 11944–11958, nov 1998.

[24] Z. Cao, X. Wei, L. Zhao, Y. Chen, and M. Yin, "Investigation of SrB_4O_7:Sm^{2+} as a multimode temperature sensor with high sensitivity," *ACS Applied Materials & Interfaces*, vol. 8, pp. 34546–34551, dec 2016.

[25] H. Kurzen, L. Bovigny, C. Bulloni, and C. Daul, "Electronic structure and magnetic properties of lanthanide 3+ cations," *Chemical Physics Letters*, vol. 574, pp. 129–132, jun 2013.

[26] F. Auzel, "Multiphonon processes, cross-relaxation and up-conversion in ion-activated solids, exemplified by minilaser materials," in *Radiationless Processes*, pp. 213–286, Springer US, 1980.

[27] D. L. Dexter, "A theory of sensitized luminescence in solids," *The Journal of Chemical Physics*, vol. 21, pp. 836–850, may 1953.

[28] T. Kushida, "Energy transfer and cooperative optical transitions in rare-earth doped inorganic materials. i. transition probability calculation," *Journal of the Physical Society of Japan*, vol. 34, pp. 1318–1326, may 1973.

[29] J. Pouradier and F. Auzel, "Calcul des probabilités des transferts dénergie entre ions de terres rares. i. une méthode de calcul unifiée utilisant des méthodes tensorielles standard," *Journal de Physique*, vol. 39, no. 8, pp. 825–831, 1978.

[30] B. M. Walsh, "Judd-Ofelt theory: principles and practices," in *Advances in Spectroscopy for Lasers and Sensing*, pp. 403–433, Springer Netherlands, 2006.

[31] G. S. Ofelt, "Intensities of crystal spectra of rare-earth ions," *The Journal of Chemical Physics*, vol. 37, pp. 511–520, aug 1962.

[32] J. H. V. Vleck, "The puzzle of rare-earth spectra in solids.," *The Journal of Physical Chemistry*, vol. 41, pp. 67–80, jan 1937.

[33] L. Broer, C. Gorter, and J. Hoogschagen, "On the intensities and the multipole character in the spectra of the rare earth ions," *Physica*, vol. 11, pp. 231–250, dec 1945.

[34] B. R. Judd, "Optical absorption intensities of rare-earth ions," *Physical Review*, vol. 127, pp. 750–761, aug 1962.

[35] M. P. Hehlen, M. G. Brik, and K. W. Krämer, "50th anniversary of the Judd–Ofelt theory: An experimentalists view of the formalism and its application," *Journal of Luminescence*, vol. 136, pp. 221–239, apr 2013.

[36] B. Flowers, "Studies in jj -coupling. i. classification of nuclear and atomic states," *Proceedings of the Royal Society of London. Series A. Mathematical and Physical Sciences*, vol. 212, pp. 248–263, apr 1952.

[37] A. R. Edmonds and B. H. Flowers, "Studies in jj -coupling. III. nuclear energy levels," *Proceedings of the Royal Society of London. Series A. Mathematical and Physical Sciences*, vol. 215, pp. 120–132, nov 1952.

[38] A. J. Freeman and R. E. Watson, "Theoretical investigation of some magnetic and spectroscopic properties of rare-earth ions," *Physical Review*, vol. 127, pp. 2058–2075, sep 1962.

[39] J. R. Peterson, W. Xu, and S. Dai, "Optical properties of divalent thulium in crystalline strontium tetraborate," *Chemistry of Materials*, vol. 7, pp. 1686–1689, sep 1995.

[40] J. Grimm, O. Wenger, K. Krämer, and H. Güdel, "4f–4f and 4f–5d excited states and luminescence properties of Tm^{2+}-doped CaF_2, $CaCl_2$, $SrCl_2$ and $BaCl_2$," *Journal of Luminescence*, vol. 126, pp. 590–596, oct 2007.

[41] J. Grimm, J. F. Suyver, E. Beurer, G. Carver, and H. U. Güdel, "Light-emission and excited-state dynamics in Tm^{2+}-doped $CsCaCl_3$, $CsCaBr_3$, and $CsCaI_3$," *The Journal of Physical Chemistry B*, vol. 110, pp. 2093–2101, feb 2006.

[42] M. de Jong, A. Meijerink, L. Seijo, and Z. Barandiarán, "Energy level structure and multiple $4f^{12}5d^1$ emission bands for Tm^{2+} in halide perovskites: Theory and experiment," *The Journal of Physical Chemistry C*, vol. 121, pp. 10095–10101, may 2017.

[43] P. A. Rodnyĭ, A. N. Mishin, and A. S. Potapov, "Luminescence of trivalent praseodymium in oxides and fluorides," *Optics and Spectroscopy*, vol. 93, pp. 714–721, nov 2002.

[44] A. Srivastava, "Aspects of Pr^{3+} luminescence in solids," *Journal of Luminescence*, vol. 169, pp. 445–449, jan 2016.

[45] H. Zellmer, P. Riedel, and A. Tünnermann, "Visible upconversion lasers in praseodymium-ytterbium-doped fibers," *Applied Physics B*, vol. 69, pp. 417–421, dec 1999.

[46] P. Solarz, J. Komar, M. Głowacki, M. Berkowski, and W. Ryba-Romanowski, "Spectroscopic characterization of $SrB_4O_7:Tm^{2+}$, a potential laser material and optical temperature sensor," *RSC Advances*, vol. 7, no. 34, pp. 21085–21092, 2017.

[47] M. de Jong and A. Meijerink, "Color tuning of Bi^{2+} luminescence in barium borates," *Journal of Luminescence*, vol. 170, pp. 240–247, feb 2016.

[48] J. Krogh-Moe, A. Magnéli, R. Seip, and H. M. Seip, "The crystal structure of strontium diborate, $SrO(B_2O_3)_2$," *Acta Chemica Scandinavica*, vol. 18, pp. 2055–2060, 1964.

[49] A. Bourbia, M. Draissia, H. Bedboudi, S. Boulkhessaim, and M. Y. Debili, "X-ray and optical crystallographic parameters investigations of high frequency induction melted Al-(α-Al_2O_3)," *Journal of X-Ray Science and Technology*, vol. 18, no. 2, pp. 201–219, 2010.

[50] P. Solarz, M. Karbowiak, M. Głowacki, M. Berkowski, R. Diduszko, and W. Ryba-Romanowski, "Optical spectra and crystal field calculation for $SrB_4O_7:Sm^{2+}$," *Journal of Alloys and Compounds*, vol. 661, pp. 419–427, mar 2016.

[51] G. Blasse, A. Meijerink, M. Nomes, and J. Zuidema, "Unusual bismuth luminescence in strontium tetraborate ($SrB_4O_7:Bi$)," *Journal of Physics and Chemistry of Solids*, vol. 55, pp. 171–174, feb 1994.

[52] W. T. Carnall, G. L. Goodman, K. Rajnak, and R. S. Rana, "A systematic analysis of the spectra of the lanthanides doped into single crystal LaF_3," *The Journal of Chemical Physics*, vol. 90, pp. 3443–3457, apr 1989.

[53] N. Kodama, F. Marumo, K. Tanaka, T. Utsunomiya, and Y. Hoshino, "Structure refinement of SrClF," *Report of The Research Laboratory of Engineering Materials, Tokyo Institute of Technology*, no. 13, pp. 7–11, 1988.

[54] W. Plato, "Erstarrungserscheinungen an anorganischen salzen und salzgemischen. II," *Zeitschrift für Physikalische Chemie*, vol. 58U, jan 1907.

[55] Y. C. Li, Y. H. Chang, Y. F. Lin, Y. S. Chang, and Y. J. Lin, "Synthesis and luminescent properties of Ln^{3+} (Eu^{3+}, Sm^{3+}, Dy^{3+})-doped lanthanum aluminum germanate $LaAlGe_2O_7$ phosphors," *Journal of Alloys and Compounds*, vol. 439, pp. 367–375, jul 2007.

[56] G. Abdullaev, G. Dzhafarov, and K. S. Mamedov, "Crystal structure of lanthanum orthoborate," *Azerbaidzhanskii Khimicheskii Zhurnal*, pp. 117–120, 1976.

[57] Y. Ni, J. M. Hughes, and A. N. Mariano, "Crystal chemistry of the monazite and xenotime structures," *American Mineralogist*, vol. 80, pp. 21–26, feb 1995.

[58] A. Meijerink, J. Nuyten, and G. Blasse, "Luminescence and energy migration in $(Sr,Eu)B_4O_7$, a system with a $4f^7$-$4f^65d$ crossover in the excited state," *Journal of Luminescence*, vol. 44, pp. 19–31, sep 1989.

[59] G. Blasse, G. Dirksen, and A. Meijerink, "The luminescence of ytterbium(II) in strontium tetraborate," *Chemical Physics Letters*, vol. 167, pp. 41–44, mar 1990.

[60] A. Zych, M. de Lange, C. de Mello Donegá, and A. Meijerink, "Analysis of the radiative lifetime of Pr^{3+} d-f emission," *Journal of Applied Physics*, vol. 112, p. 013536, jul 2012.

[61] J. P. Hurrell, S. P. S. Porto, I. F. Chang, S. S. Mitra, and R. P. Bauman, "Optical phonons of Yttrium Aluminum Garnet," *Physical Review*, vol. 173, pp. 851–856, sep 1968.

[62] M. Pollnau, D. R. Gamelin, S. R. Lüthi, H. U. Güdel, and M. P. Hehlen, "Power dependence of upconversion luminescence in lanthanide and transition-metal-ion systems," *Physical Review B*, vol. 61, pp. 3337–3346, feb 2000.

[63] L. Guerbous, M. Seraiche, and O. Krachni, "Photoluminescence and electron-vibrational interaction in $4f^{n-1}5d$ states of Ce^{3+} or Pr^{3+} ions doped $LnBO_3$ (Ln=Lu, Y, La) orthoborates materials," *Journal of Luminescence*, vol. 134, pp. 165–173, feb 2013.

[64] G. H. Dieke and H. M. Crosswhite, "The spectra of the doubly and triply ionized rare earths," *Applied Optics*, vol. 2, p. 675, jul 1963.

[65] A. Remillieux, B. Jacquier, C. Linarès, C. Lesergent, S. Artigaud, D. Bayard, L. Hamon, and J. L. Beylat, "Upconversion mechanisms of a praseodymium-doped fluoride fibre amplifier," *Journal of Physics D: Applied Physics*, vol. 29, pp. 963–974, apr 1996.

[66] B. D. Bartolo and B. Bowlby, "Spectroscopic properties of trivalent praseodymium in barium yttrium fluoride," *Journal of Luminescence*, vol. 102-103, pp. 481–486, may 2003.

[67] S. Mahlik, M. Malinowski, and M. Grinberg, "High pressure luminescence and time resolved spectra of $La_2Be_2O_5$:Pr^{3+}," *Optical Materials*, vol. 34, pp. 164–168, nov 2011.

[68] K. Oskam, A. Houtepen, and A. Meijerink, "Site selective 4f5d spectroscopy of CaF_2:Pr^{3+}," *Journal of Luminescence*, vol. 97, pp. 107–114, may 2002.

[69] M. Weber, "Nonradiative decay from 5d states of rare earths in crystals," *Solid State Communications*, vol. 12, pp. 741–744, apr 1973.

[70] L. van Pieterson, M. F. Reid, R. T. Wegh, S. Soverna, and A. Meijerink, "$4f^n \to 4f^{n-1}5d$ transitions of the light lanthanides: Experiment and theory," *Physical Review B*, vol. 65, jan 2002.

[71] K. V. Ivanovskikh, J. M. Ogiegło, A. Zych, C. R. Ronda, and A. Meijerink, "Luminescence temperature quenching for Ce^{3+} and Pr^{3+} d-f emission in YAG and LuAG," *ECS Journal of Solid State Science and Technology*, vol. 2, pp. R3148–R3152, dec 2012.

[72] G. B. Nair and S. Dhoble, "Assessment of electron-vibrational interaction (EVI) parameters of YAG:Ce^{3+}, TAG:Ce^{3+} and LuAG:Ce^{3+} garnet phosphors by spectrum fitting method," *Spectrochimica Acta Part A: Molecular and Biomolecular Spectroscopy*, vol. 173, pp. 822–826, feb 2017.

[73] M. Nikl, H. Ogino, A. Krasnikov, A. Beitlerova, A. Yoshikawa, and T. Fukuda, "Photo- and radioluminescence of Pr-doped $Lu_3Al_5O_{12}$ single crystal," *physica status solidi (a)*, vol. 202, pp. R4–R6, jan 2005.
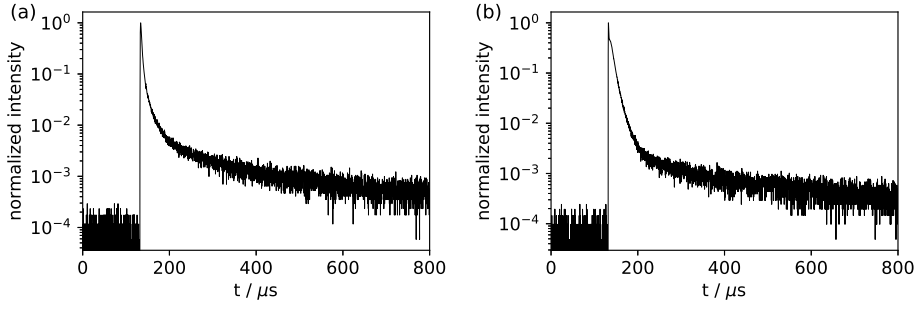
Appendix A - Uncorrected luminescence decay curves
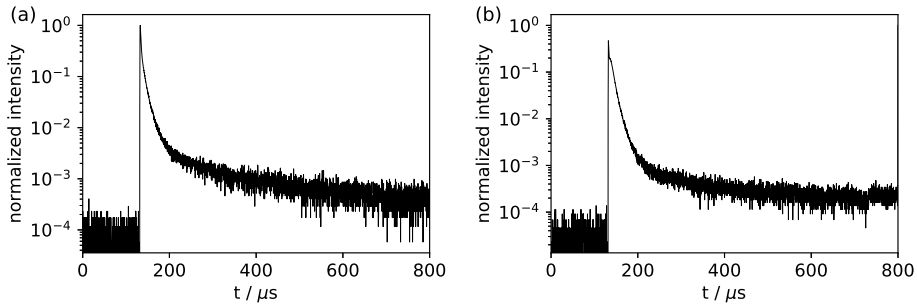

Figure A.1: Uncorrected luminescence decay curves of the Pr^{3+} $^3P_0 \rightarrow {}^3H_4$ emission ($\lambda_{em} = 485$ nm) in the $LaBO_3$ host upon (a) $^3H_4 \rightarrow {}^3P_2$ ($\lambda_{ex} = 451$ nm) and (b) $^3H_4 \rightarrow {}^3P_0$ ($\lambda_{ex} = 480$ nm) excitation.
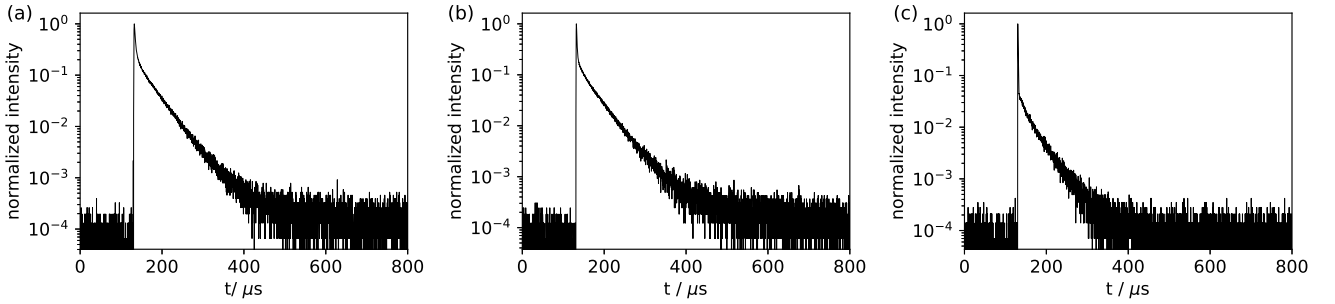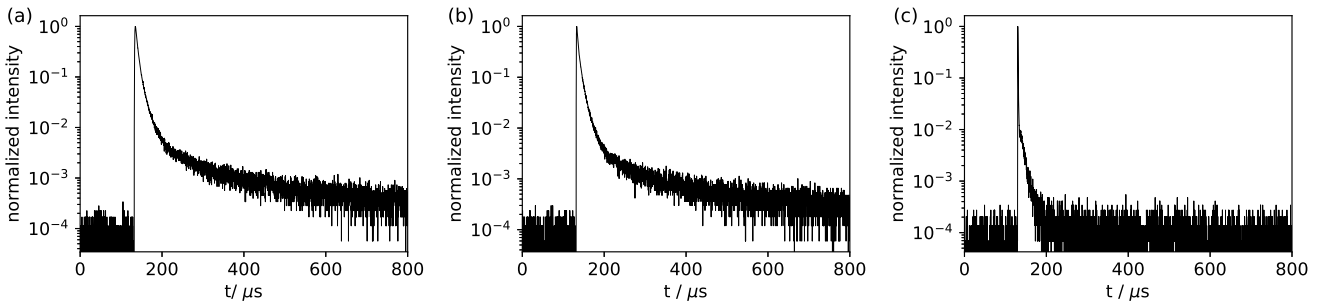

Figure A.2: Uncorrected luminescence decay curves of the Pr^{3+} $^1D_2 \rightarrow {}^3H_4$ emission ($\lambda_{em} = 615$ nm) in the $LaBO_3$ host upon (a) $^3H_4 \rightarrow {}^3P_2$ ($\lambda_{ex} = 451$ nm), (b) $^3H_4 \rightarrow {}^3P_0$ ($\lambda_{ex} = 480$ nm) and (c) $^3H_4 \rightarrow {}^1D_2$ ($\lambda_{ex} = 580$ nm) excitation.

Figure A.3: Uncorrected luminescence decay curves of the Pr^{3+} $^3P_0 \rightarrow {}^3H_4$ emission ($\lambda_{em} = 485$ nm) in the YPO_4 host upon (a) $^3H_4 \rightarrow {}^3P_2$ ($\lambda_{ex} = 451$ nm) and (b) $^3H_4 \rightarrow {}^3P_0$ ($\lambda_{ex} = 480$ nm) excitation.

Figure A.4: Uncorrected luminescence decay curves of the Pr^{3+} $^1D_2 \rightarrow {}^3H_4$ emission ($\lambda_{em} = 615$ nm) in the YPO_4 host upon (a) $^3H_4 \rightarrow {}^3P_2$ ($\lambda_{ex} = 451$ nm), (b) $^3H_4 \rightarrow {}^3P_0$ ($\lambda_{ex} = 480$ nm) and (c) $^3H_4 \rightarrow {}^1D_2$ ($\lambda_{ex} = 580$ nm) excitation.
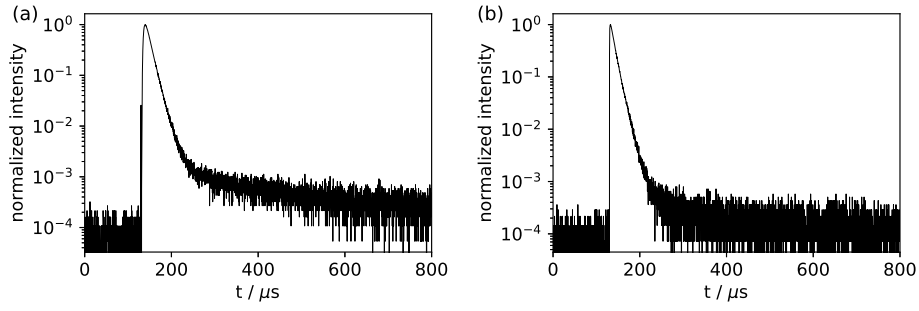
Figure A.5: Uncorrected luminescence decay curves of the Pr^{3+} $^3P_0 \rightarrow {}^3H_4$ emission ($\lambda_{em} = 485$ nm) in the LuAG host upon (a) $^3H_4 \rightarrow {}^3P_2$ ($\lambda_{ex} = 451$ nm) and (b) $^3H_4 \rightarrow {}^3P_0$ ($\lambda_{ex} = 480$ nm) excitation.
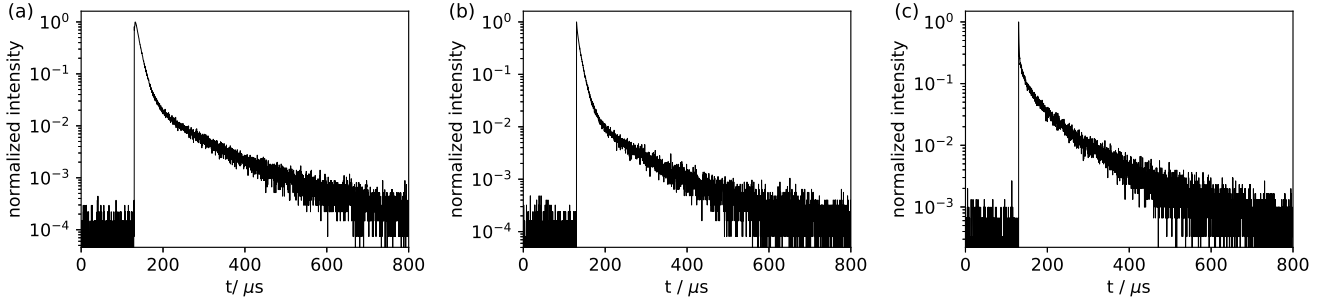

Figure A.6: Uncorrected luminescence decay curves of the Pr^{3+} $^1D_2 \rightarrow {}^3H_4$ emission ($\lambda_{em} = 615$ nm) in the LuAG host upon (a) $^3H_4 \rightarrow {}^3P_2$ ($\lambda_{ex} = 451$ nm), (b) $^3H_4 \rightarrow {}^3P_0$ ($\lambda_{ex} = 480$ nm) and (c) $^3H_4 \rightarrow {}^1D_2$ ($\lambda_{ex} = 580$ nm) excitation.